

**T.C.**

**UNIVERSITY OF TURKISH AERONAUTICAL ASSOCIATION  
SCIENCE AND TECHNOLOGY INSTITUTE**

**EFFECTS OF VARIOUS PARAMETERS ON THE STRENGTH AND  
FAILURE MODE OF BOLTED, BONDED AND HYBRID SINGLE LAP  
JOINTS: AN EXPERIMENTAL AND NUMERICAL STUDY**

**Ph.D. THESIS**

**Mossa EL ZAROUG**

**1303947002**

**GRADUATE SCHOOL OF AERONAUTICS AND ASTRONAUTICS  
Mechanical and Aeronautical Engineering (English) (Doctorate)**

**MAY 2018**

**T.C.**  
**UNIVERSITY OF TURKISH AERONAUTICAL ASSOCIATION**  
**SCIENCE AND TECHNOLOGY INSTITUTE**

**EFFECTS OF VARIOUS PARAMETERS ON THE STRENGTH AND  
FAILURE MODE OF BOLTED, BONDED AND HYBRID SINGLE LAP  
JOINTS: AN EXPERIMENTAL AND NUMERICAL STUDY**

**Ph.D. THESIS**

**Mossa EL ZAROUG**

**1303947002**

**GRADUATE SCHOOL OF AERONAUTICS AND ASTRONAUTICS**

**Mechanical and Aeronautical Engineering (English) (Doctorate)**

**Thesis Supervisor: Assoc. Prof. Dr. Murat DEMIRAL**

Mossa R. El zaroug, having student number 1303947002 and enrolled in the Ph.D. Program at the Institute of Science and Technology at the University of Turkish Aeronautical Association, after meeting all of the required conditions contained in the related regulations, has successfully accomplished, in front of the jury, the presentation of the thesis prepared with the title of: "EFFECTS OF VARIOUS PARAMETERS ON THE STRENGTH AND FAILURE MODE OF BOLTED, BONDED AND HYBRID SINGLE LAP JOINTS: AN EXPERIMENTAL AND NUMERICAL STUDY"


**Thesis Supervisor: Assoc. Prof. Dr. Murat DEMIRAL**  
**University of Turkish Aeronautical Association**



**Jury Members: Assoc. Prof. Dr. Murat DEMIRAL**  
**University of Turkish Aeronautical Association**



**: Assoc. Prof. Dr. Barış SABUNCUOĞLU**  
**Hacettepe University**



**: Dr. Öğr. Üyesi. Monier ELFARRA**  
**Yıldırım Beyazıt University**



**: Dr. Öğr. Üyesi. Muharrem KUNDURACI**  
**University of Turkish Aeronautical Association**



**: Dr. Öğr. Üyesi. Hamed TANABI**  
**University of Turkish Aeronautical Association**



**Thesis Defense Date: 25 May 2018.**

**UNIVERSITY OF TURKISH AERONAUTICAL ASSOCIATION**

**INSTITUTE OF SCIENCES AND TECHNOLOGY**

**STATEMENT OF NON-PLAGIARISM**

I hereby declare that all information in this study I present as my Ph.D. thesis, entitled: *Effects of various parameters on the strength and failure mode of bolted, bonded and hybrid single lap joints: an experimental and numerical study*, has been presented in accordance with the academic rules and ethical conduct. I also declare and certify with my honor that I have fully cited and referenced all the sources utilized in this study.

25 May 2018.

Mossa Ramadan EL ZAROUG



# **ABSTRACT**

## **EFFECTS OF VARIOUS PARAMETERS ON THE STRENGTH AND FAILURE MODE OF BOLTED, BONDED AND HYBRID SINGLE LAP JOINTS: AN EXPERIMENTAL AND NUMERICAL STUDY**

EL ZAROUG, Mossa

Ph.D., Department of Mechanical and Aeronautical Engineering

Thesis Supervisor: Assoc. Prof. Dr. Murat, DEMIRAL

June-2018, 125 pages

In line with the developments in advanced engineering applications, such as the aerospace and automotive industries, the techniques of joining similar and dissimilar materials have become a crucial issue, and the necessity for a superior joint has significantly grown. Compared to conventionally used bolted, riveted and pinned joints, adhesively bonded joints have been increasingly used due to their improved fatigue life and damage tolerance, lower structural weight and easy manufacturing, especially the case when relatively thin adherends are used. Alternatively, hybrid joints, a combination of two or more joining techniques, are presently investigated to create a joint with higher strength than those gained from one technique. In this thesis, we compare and contrast the mechanical performance of bolted, bonded and hybrid single lap joints subject to tensile loading for various parameters such as adherend thickness, overlap length and adherend material with different mechanical properties, such as yield, tensile strength and ductility. To this end, a combined experimental and numerical study was performed. In finite element simulations, cohesive zone, ductile and shear damage models were used to model the damage initiation and evolution of

the adhesive film layer (AF163-2K), aluminum adherend (AL6061 and AL7075) and the steel bolt materials. Force displacement curves, the amount of energy absorbed and failure history for each configuration tested were analyzed extensively to determine the strength of various joints.

**Keywords:** Adhesive joint, bolted joint, hybrid joint, overlap length, materials properties, numerical analysis, failure mode.



# ÖZET

## CİVATA, YAPIŞTIRICI VE HİBRİD TEK TESİRLİ BAĞLANTILARIN MUKAVEMETİ VE KIRILMA MODLARINA FARKLI PARAMETRELERİN ETKİLERİ: DENEYSEL VE NÜMERİK ÇALIŞMA

EL ZAROUG, Mossa

Doktora, Makina Mühendisliği ve Havacılık Mühendisliği Bölümü

Tez Danışmanı: Assoc. Prof. Dr. Murat, DEMİRAL

Haziran -2018, 125 sayfa

Havacılık ve otomotiv endüstrisi gibi ileri mühendislik uygulamalarındaki gelişmelere paralel olarak, benzer ve farklı malzemelerin birleştirilmesi teknikleri çok önemli bir konu haline gelmiştir, diğer bir ifade ile üstün özelliklere sahip bağlantılara olan ihtiyaç giderek büyümektedir. Alternatif olarak iki veya daha fazla birleştirme tekniğinin kombinasyonu olan hibrid bağlantılar onu oluşturan bağlantı tekniklerinin her birinden daha üstün özelliklere sahip olabilmesi açısından araştırılmaktadır. Bu tezde civata, yapıştırıcı ve hibrid konfigürasyonuna sahip tek tesirli bağlantıların çekme yüküne maruz bırakılmaları halindeki mekanik performansları yapıştırılan numunelerin kalınlıkları, bindirme uzunlukları ve yapıştırılan malzemelerin farklı mekanik özelliklere sahip olması gibi farklı parametreler için karşılaştırılmıştır. Bu amaçla deneysel ve nümerik çalışmalar birlikte gerçekleştirilmiştir. Sonlu elemanlar simülasyonlarında, kohezif bölge elemanı, sünek ve kayma hasar modelleri sırasıyla yapıştırıcı tabaka, yapıştırılan numune ve civata malzemelerinin modellenmesinde kullanılmıştır. Farklı konfigürasyonlar için kuvvet-yerdeğiştirme, absorbe edilen enerji miktarı ve kırılma hikayesi farklı tek tesirli bağlantıların mukavemetlerini değerlendirebilmek için detaylı bir şekilde analiz edilmiştir.

**Anahtar sözcükler:** Yapıştırıcı bağlantılı, civata bağlantılı, hibrid bağlantılı bindirme uzunluğu, malzeme özelliği, nümerik analizler, kırılma modu

# TABLE OF CONTENTS

ABSTRACT.....	I
ÖZET.....	I
TABLE OF CONTENTS.....	II
LIST OF FIGURES.....	V
LIST OF TABLES.....	XI
ACKNOWLEDGEMENTS.....	XII
PUBLICATIONS AND CONFERENCE.....	XIII
NOMENCLATURE.....	XIV
CHAPTER 1.....	1
INTRODUCTION.....	1
1.1 Motivation.....	1
1.2 Aims and Objectives.....	2
1.3 Methodology.....	3
CHAPTER 2.....	4
LITERATURE REVIEW.....	4
2.1 Definitions.....	4
2.1.1 Single Lap Joint (SLJ).....	6
2.1.2 Adhesive Joint (ADJ).....	7



2.1.2.1	Adhesion Mechanisms .....	8
2.1.2.2	Fracture Modes .....	9
2.1.2.3	Failure of Adhesive Joints .....	10
2.1.3	Bolted Joint (BJ).....	14
2.1.4	Hybrid Joint .....	17
2.1.5	Aluminum Alloys .....	17
2.2	Literature Review .....	19
2.2.1	Adhesive Joint .....	19
2.2.2	Bolted Joint.....	27
2.2.3	Hybrid Joint .....	28
2.2.4	Improvement of the Bonded SLJ.....	31
CHAPTER 3	.....	43
EXPERIMENTAL WORK AND MATERIALS	.....	43
3.1	Configurations of the Joints .....	43
3.2	Samples Preparation.....	44
3.3	Materials.....	49
CHAPTER 4	.....	54
NUMERICAL MODELLING	.....	54
4.1	Finite Element Method (FEM).....	54
4.1.1	Time Integration Methods (Explicit).....	57
4.2	Cohesive Zone Modelling (CZM).....	60
4.3	Fracture of Ductile Metals .....	64
4.3.1	Ductile Damage Criterion .....	65
4.3.2	Shear damage criterion.....	65
4.3.3	Damage evolution.....	66

4.4	ABAQUS Software .....	68
4.5	Simulations.....	71
CHAPTER 5 .....		78
RESULTS AND DISCUSSIONS .....		78
5.1	Influence of the Adherend Thickness .....	78
5.1.1	Bolted Joints .....	78
5.1.2	Bonded Joints .....	84
5.1.3	Hybrid Joints .....	86
5.2	Influence of the Overlap Length .....	93
5.2.1	Bolted Joints .....	93
5.2.2	Bonded Joints .....	98
5.2.3	Hybrid joints.....	101
CHAPTER 6 .....		107
CONCLUSIONS AND FUTURE WORK .....		107
6.1	Conclusions .....	107
6.2	Future Work .....	109
REFERENCES.....		112

# LIST OF FIGURES

Figure 2.1: Effect of adherend thickness on the failure modes of adhesively bonded joints [3].	5
Figure 2.2: Classification and application of adhesively bonded joints applied and utilized during airframe manufacture [1].	6
Figure 2.3: Notation for the single lap joint.	7
Figure 2.4 : Interlaminar stress in an adhesive[4].	7
Figure 2.5: Adhesive joint interphase [6].	8
Figure 2.6: The illustration of (a) Adsorption Theory, (b) Diffusion Theory, (c) Mechanical Theory and (d) Electrostatic Theory [8].	9
Figure 2.7: Mode-I, Mode-II, and Mode-III crack propagation modes. [11].	10
Figure 2.8: Failure types of adhesive joints [6].	11
Figure 2.9: Bonded SLJ with different rounding radius. (a) Joint geometry (b) Sharp corner (c) Small radius (d) Medium radius (e) Large radius [13, 14].	12
Figure 2.10: Shape of the spew fillet (a) at the end of the adhesive layer; (b) covering the adherend end [15].	12
Figure 2.11: Chamfering of the unloaded ends of the adherends [16].	13
Figure 2.12: Geometry and dimensions of a single-lap joint with flat adherends, $K_e = 1$ (a) and with reverse-bent geometry, $K_e = -1$ (b) [18].	14
Figure 2.13: Bolted single lap joint configuration [20].	15
Figure 2.14: Failure modes: (a) net-tension, (b) bearing, (c) shear tear-out, and (f) bolt shear [22, 23].	16

Figure 2.15: Effects of secondary bending (SB) and bypass load on (a) bolt hole deformations, (b) stress concentration and (c) contact area of the joint lap [24]. .....	16
Figure 2.16: Test specimen geometry for hybrid joint [25]. .....	17
Figure 2.17: Maximum stress at failure vs. adhesive thickness [38]. .....	20
Figure 2.18: Experimental results of strength of joints vs. OL [43]. .....	20
Figure 2.19: Strength and failure loads of bonded joints with different bonding pressures for 25 mm overlap length [44]. .....	21
Figure 2.20: Strength and failure loads of bonded joints with different OLs [44]. ....	22
Figure 2.21: Effect of the elastic modulus on the strength of the joint [47]. .....	23
Figure 2.22: Effect of the elastic modulus on the rotation angle of the joint [47]. ....	23
Figure 2.23: Numerical (CZM) and experimental results of the failure loads vs. the overlap lengths for different adhesives [48]. .....	24
Figure 2.24: Experimental and numerical failure loads vs. different overlap lengths of adhesive joints with adhesive XNR6823 (a) and XNR6852 (b) [49]. .....	25
Figure 2.25: Peeling stress distributions at the adhesive mid-thickness for different OLs[49]. .....	26
Figure 2.26: Numerical and experimental comparison of the force - displacement tests for 1+2 layout rivet joints [86]. .....	30
Figure 2.27: Shape and size of the spew fillet of the single lap joint [15]. .....	32
Figure 2.28: Effect of spew fillet and chamfering on peeling stress [16]. .....	34
Figure 2.29: Failure load vs. taper angle for different OL using Neoxil CE92 N8 adhesive [17]. .....	35

Figure 2.30: Effect of tapered angle on peeling stress [17].	35
Figure 2.31: Peel stresses in adhesive MY750 with a 20 kN applied load, close to the unloaded adherend [13, 14].	36
Figure 2.32: Stress distributions of the mid-thickness of the adhesive layer for different values of K [18].	37
Figure 2.33: The peeling stress along different level of the adhesive thickness of the spew fillet [27].	38
Figure 2.34: Location and shape of reinforcement [96].	39
Figure 2.35: Effect of spew fillet and attached reinforcement on peel stress [96].	39
Figure 2.36: SLJ scheme with slots and bi-adhesive [97].	40
Figure 2.37: SLJ schemes of with and without reinforcements [97].	40
Figure 2.38: Effect of adherend and reinforcement strength on joint strength [97].	41
Figure 2.39: Configuration of the new design of the HJ [98].	42
Figure 2.40: Peeling stress along the overlap length in the middle plane of the adhesive layer for new and baseline designs of the HJ [98].	42
Figure 3.1: Geometry, boundary conditions and dimensions of adhesive (a) and bolted (b) joint configurations (side and top view, respectively).	44
Figure 3.2: Preparation of adherents.	45
Figure 3.3: AF163-2K adhesive film.	46
Figure 3.4: Alignment set (jig).	46
Figure 3.5: Jig inside the oven where the samples were cured.	47
Figure 3.6: Drilling machine with laser alignment.	47

Figure 3.7: A group of specimens after preparing. ....	48
Figure 3.8: Setting up the single lap joints with the rotary laser level. ....	48
Figure 3.9: Tensile stress-strain curves for the AL6061 and AL7075 adherends. ....	50
Figure 3.10: Tensile stress-strain curve for the adhesive film (AF163-2K). ....	50
Figure 3.11: Shear stress-strain curve for the adhesive film (AF163-2K). ....	51
Figure 3.12: Bulk adhesive (a), thick adherend specimens (b) and tensile test specimen (c). ....	52
Figure 3.13: Stress-strain relationship used in the simulations for the adherend materials. ....	53
Figure 4.1: Stages of the physical simulation procedure [103]. ....	56
Figure 4.2: Linear damage evolution [110]. ....	62
Figure 4.3: Illustration of mixed-mode response in cohesive elements [110]. ....	63
Figure 4.4: Formulation of the crack under tensile and shear loading [114]. ....	64
Figure 4.5: Stress-strain curve with progressive damage degradation [110]. ....	67
Figure 4.6: Integration points scheme in elements C3D8R and C3D8 [109-112]. ....	70
Figure 4.7: 3D finite element model of a single lap joint with hybrid configuration (bolted and bonded). ....	72
Figure 4.8: Study of mesh convergency regarding the force-displacement curve obtained for a HJ with 4 mm AL7075 adherends. ....	73
Figure 4.9: All internal energy (ALLIE) and all kinetic energy (ALLKE) in the model for the HJ of 2 mm AL6061 adherends. ....	74
Figure 4.10: Equivalent plastic strain values at damage initiation as a function of stress triaxiality in the ductile damage model [101]. ....	76

Figure 5.1: Experimentally and numerically obtained load-displacement curves of BJ for 15 mm OL.....	79
Figure 5.2: Experimentally and numerically obtained failure modes of the BJ for AL6061 for 15 mm OL.....	82
Figure 5.3: Experimentally and numerically obtained failure modes of the BJ for AL7075 for 15 mm OL.....	83
Figure 5.4: Experimentally and numerically obtained load–displacement curves of ADJ for 15 mm OL.....	85
Figure 5.5: Experimentally (a) and numerically (b) observed adhesive failure and damage progress in the adhesive layer during deformation (c) for the 2 mm AL6061 adherends joined via adhesive bonding for 15 mm OL.....	86
Figure 5.6: Experimentally and numerically obtained load–displacement curves of the HJ for 15 mm OL.....	87
Figure 5.7: Experimentally and numerically obtained failure modes of the HJ for AL6061 for 15 mm OL.....	88
Figure 5.8: Experimentally and numerically obtained failure modes of the HJ for AL7075 for 15 mm OL.....	89
Figure 5.9: Stress distribution in the adhesive layer and the bolt material just before the complete damage of the adhesive layer was attained (a) and the comparison of stresses in the bolt just before (left) and just after (right) complete damage in the adhesive layer for hybrid joint of 2 mm AL6061 adherends .....	92
Figure 5.10: $x$ -displacement of the bolt (just before its complete damage was attained) for 6 mm AL6061 adherends via bolted (a) and hybrid (b) joint configurations for 15 mm OL.....	93
Figure 5.11: Experimentally and numerically obtained load displacement curves of bolted joints.....	94

Figure 5.12: Failure modes observed in bolted joints: (a) Net-tension failure and (b) Bolt failure (Left: Experimental, Right: FE simulation)..... 97

Figure 5.13: x-displacement of the bolt (just before the damage initiated on the bolt surface) (a) and the bearing area for the upper and lower adherends (b) in the bolted joints of 2 mm AL6061 adherends for both 25 mm and 45 mm overlap lengths..... 98

Figure 5.14: Experimentally and numerically obtained load displacement curves of bonded joints..... 99

Figure 5.15: Cohesive failure observed in bonded joints (a: Experimental, b: FE simulation) ..... 100

Figure 5.16 : Stress distributions (just before the cohesive failure occurred) in the 2 mm thickness of AL7075 adherends with bonded joints for the overlap length of 45 mm (top) and 25 mm (bottom)..... 101

Figure 5.17: Experimentally and numerically obtained load displacement curves of HJ of AL6061. .... 103

Figure 5.18: Experimentally and numerically obtained load displacement curves of HJ of AL7075. .... 104

Figure 5.19: Failure modes observed in hybrid joints: (a) Adherend failure, (b) Net-tension failure and (c) Bolt failure (Left: Experimental, Right: FE simulation). .... 105

Figure 5.20: Shear and ductile damage distributions on the surfaces of bolts for 6 mm AL6061 adherends in the hybrid (left) and bolted (right) joint configurations at  $P = 8$  kN (after the cohesive failure for HJ). .... 106

Figure 6.1: New joint configurations for BJ and HJ. .... 111

Figure 6.2: Adhesive layer configurations. .... 111



## LIST OF TABLES

Table 2.1: Percentage of material composition for AL6061 and AL7075 [26]......	18
Table 3.1: Material parameters of adhesive layer in numerical analysis. ....	49
Table 3.2: Elastic properties of materials.....	51
Table 3.3: Plastic properties of Materials extract from the true stress-strain curve...	53
Table 4.1: Damage parameters of aluminum adherends and steel bolt materials used in the FE analysis [121-123]......	76
Table 4.2: Equivalent plastic strain values at damage initiation for different stress triaxiality used in ductile damage model. ....	77
Table 5.1: Experimentally obtained energy absorption values and failure types for different joints and various thickness of AL6061 and AL7075 adherends for 15 mm OL.....	80
Table 5.2: Experimentally obtained energy absorption values and failure types for different joint configurations with 25 mm and 45 mm overlap lengths and various thicknesses of AL6061 and AL7075 adherends.....	96

## ACKNOWLEDGEMENTS

I am, and will always be, deeply indebted to my supervisor Assoc. Prof. Dr. Murat Demiral for his intellectual instructions, encouragement, suggestive ideas, constructive criticism and motivation. His patience and understanding I appreciate. It has helped me to sail through the hard times. I am very much grateful to him for this.

I would like to express my deepest gratitude and appreciation to Assoc. Prof. Dr. Ferhat Kadiođlu from Yildirim Beyazit University, who inspired, encouraged and supported me during this study. He helped me at various stages during my PhD studies and willingly shared his knowledge and ideas with me. His active participation in every aspect of my research work as well as his mentoring have shaped my overall research outlook. He has shown his kindness while donating the needed materials and providing the experimental facilities in his own lab.

My sincere appreciation and gratitude are extended to my parents, my wife (Eman) and my daughters (Sagda, Yagen and Waqar) for their continued support, and patience during my study.

I would also like to express my gratitude and appreciation to my extended family and my friends for their assistance and encouragement. I will always remember them and be grateful to them.

Ultimately, even though, I might have tried to make the acknowledgment list as complete as possible, and I will regret any involuntary omissions of those who feel that their names are missing. Everyone who contributed, in one way or the other, I will be forever grateful, thankful and humble.

## **PUBLICATIONS AND CONFERENCE**

### **Publications**

1. Submitted to the **International Journal of Adhesion & Adhesives** under the title of “*Experimental and numerical investigation into strength of bolted, bonded and hybrid single lap joints: Effects of adherend material type and its thickness*”.
2. To be submitted under the title of “*Effects of overlap length on the strength of bolted, bonded and hybrid single lap joints for different adherend materials and thicknesses*”

### **Conference**

1. **M. El zaroug, F. Kadioglu, M. Demiral**, *Some parameters on the hybrid joints under tensile loading*, 4<sup>th</sup> International Conference of Structural Adhesive Bonding (AB2017), 6/7 July 2017, Porto

## NOMENCLATURE

$\xi$	Critical damping
$\omega_D$	State variable in ductile criterion
$\omega_S$	State variable in shear criterion
$\tau_{max}$	Maximum shear stress
$\sigma_{y0}$	Yield stress at the onset of damage
$\theta_S$	Shear stress ratio
$\nu$	Poisson's ratio
$\tau$	Shear stress
$\mathbf{u}$	Displacements
$d\boldsymbol{\varepsilon}$	Element strain increments
$k_S$	Material parameter
$\Omega^e$	Domain of elements
$\sigma$	Stress
$\rho$	Density
$\eta$	Stress triaxiality
$\delta_f$	Effective displacement at complete failure
$\delta_0$	Relative to the effective displacement at damage initiation
$\delta$	Displacement
$t$	Time increment
$q$	Von Mises equivalent stress
$p$	Pressure stress
$\mathbf{P}$	Vector of externally applied force
$A$	Authentic exterior and outward area
$AD$	Adherend failure
$A_D$	Defects outward and exterior area
$C_d$	Current and effective dilatational wave speed of the material
$D$	Damage evolution variable
$\boldsymbol{\varepsilon}$	Strain
$E$	Elastic modulus

$F$	Force
$G$	Shear modulus
$I$	Vector of internal element forces
$K$	Master stiffness matrix
$K_e$	Eccentricity parameter
$L_e$	Characteristic length of the element
$M$	Bulk mass matrix
$M^{-1}$	Lumping matrix
$\dot{u}^e$	Node degree of freedom velocities
$\dot{\bar{\epsilon}}^{pl}$	Equivalent plastic strain rate
$\vec{V}^e$	Velocity field
$\bar{u}^{pl}$	Effective plastic displacement
$\bar{u}_f^{pl}$	Effective plastic displacement at failure
$\bar{\epsilon}^{pl}$	Effective plastic strain
$\bar{\epsilon}_D^{pl}$	Equivalent plastic strains are at the onset of damage
$\bar{\epsilon}_S^{pl}$	Equivalent plastic strain in shear criterion
$\bar{\epsilon}_f^{pl}$	Equivalent plastic strain at failure (when the D=1)
$\bar{\epsilon}^{pl}$	Equivalent plastic strain in ductile criterion
$\bar{\epsilon}_0^{pl}$	Equivalent plastic strain at the onset of damage
$T_0$	Original thickness of the cohesive element
$C_d$	Current and effective dilatational wave speed of the material
$L_e$	Dimension of characteristic element
$M^e$	Element mass matrix
$N_v^e$	Shape function matrix
$T^e$	Kinetic energy of elements
$\dot{d}$	Linear form of damage evolution with plastic displacement
$\ddot{u}$	Acceleration of the nodal
$\dot{u}$	Velocities

$\delta_n, \delta_s, \delta_t$	Represents the displacements at damage initiation in main direction n, s, t
$\varepsilon_f$	Failure strain
$\sigma_n^0, \sigma_s^0, \sigma_t^0$	Represents the ultimate values of the nominal stresses at damage initiation in main direction n, s, t
$\varepsilon_p$	Plastic strain
$\sigma_p$	Plastic stress
$\sigma_u$	Ultimate stress
$\sigma_y$	Yield stress
$\tau_u$	Ultimate shear stress
$\dot{\varepsilon}$	Strain rate
$\bar{\sigma}$	Effective or undamaged stress
$\omega_{max}$	Maximum eigenvalues
$\omega_{max}^{element}$	Element maximum eigenvalues
$\Delta t$	Finite time increment

# CHAPTER 1

## INTRODUCTION

### 1.1 Motivation

In accordance with the advancements and developments in the aeronautical industry, the techniques and methodologies of joining similar and dissimilar materials have always been considered as a very important, vital and significant issue. From the beginning of aviation, the bolted joint (BJ) has been widely used in aircraft, and even with the widespread use of composite materials, they still play a key role in aeronautical structures. High stiffness and strength, as well as the connectors that can be taken away for inspection and maintenance, or the accessibility of the hidden parts of the structure, are among the advantages of bolted joints. However; due to the large concentrations of stress that developed around the bolt hole, joints can fail at lower levels of stress. Adhesively bonded joints (ADJ) offer more uniform distribution of stresses in the adherends (no hole existing) compared to mechanical joints. They also offer improved fatigue life, lower structural weight, the prevention or reduction of corrosion between dissimilar materials, thus providing an alternative technique to the BJ. On the other hand, the hybrid joint (HJ) combines the advantages of two or more joining techniques. They have a higher static and fatigue strength, a higher stiffness and improved durability with respect to simple joints. Its two-stage cracking process before the final failure promotes its use compared to the bolted and bonded single lap joints (SLJ), where catastrophic failures in structures can occur in connecting areas without any early warning or notification. The loads are often transferred in

## Chapter 1

mechanical joints by the compression on the internal faces of the fastener holes, with a smaller component of shear stress on the outer faces of the adherents due to friction. On the other hand, the loads can be transferred mainly by shear stress on the surfaces of the adhesive layer in the ADJ. In all the joints, the stress distributions are, however, known to be complicated.

The demand and necessity for a superior joint have grown impressively. However, their productive design and manufacturing possess is a huge challenge to safety, cost-effectiveness, and efficiency. Investigation into the effect of various joint parameters, such as overlap length, adherend materials and geometrical constraints, may contribute to determining a superior joint design. This study is dedicated to observing the influence of various parameters such as the adherend thickness, adherend material and the overlap length in the mechanical performance of the BJ, ADJ and HJ.

### **1.2 Aims and Objectives**

The goal of this research is to further the understanding of the strength of bolted, bonded and hybrid SLJ and the limitations of their stiffness, experimentally and numerically. To achieve the aim of the project, its major objectives are formulated as follow:

- To investigate the deformation response of the adhesive, adherend and bolt materials using the quasi-statically performed tensile loading for different test parameters such as the adherend material with different mechanical properties, adherend thickness and the overlap length;
- To develop continuum numerical models incorporating initiation of plasticity and damage with their evolutions representing the mechanical performance of the bolted, bonded and hybrid single lap joints, and in connection with this to obtain an accurate description of local fields of strains, stresses and damage variables inside and on the surfaces of the samples that is not possible to achieve in experiments.



### 1.3 Methodology

This research presents an experimental and numerical modeling approach to the quasi-static performance of SLJs subjected to axial tensile loading. A series of experiments were applied to the combination of three different thicknesses (2 mm, 4 mm and 6 mm) of two different adherents, Al7075 and Al6061, with three different overlap lengths (15 mm, 25 mm, 45 mm), united through the various joints. In order to obtain an in-depth understanding of the strength and the failure modes of these joint configurations, numerical analyses were performed using the *ABAQUS / Explicit* Finite-Element program. Since the aluminum adherend had different mechanical behavior with different yield strengths, tensile strengths and ductility values, their different responses under loading created the opportunity to explore the deformation mechanism with the underlying physics of the three different joints.

This systematic approach and investigation with its diverse parameters was helped by promoting and inspiring the uniqueness of this study.

This thesis is presented as follows:

A literature survey about the single lap joint is presented in Chapter 2. A description of the materials used in the experiments, and relevant experimental studies are given in Chapter 3. Chapter 4 describes first the finite element method including the explicit time integration scheme and different damage models followed by the details of the developed numerical model. In Chapter 5 the validation of the numerical model developed against the experimental data with a discussion of critical results in terms of the effect of the adherend thickness and the effect of the overlap length are presented. The thesis ends with some concluding remarks in Chapter 6.

## **CHAPTER 2**

### **LITERATURE REVIEW**

This chapter reviews the bolted, bonded and hybrid single lap joints with regard to their mechanical performances for various constraints, such as geometry of the SLJ, loading conditions, etc. In the first part of this chapter, the definitions of the SLJ with different configurations are given. Their individual critical review is given in the second part.

#### **2.1 Definitions**

In an attempt to understand how the aerospace industries operate, it is necessary to reduce and limit the number and complexity of joints that could in turn help to reduce weight and increase cost-effectiveness. The very vital benefit of composite construction is its capability to shape creatively and productively unitized components, which minimizes the number of the required joints. However, the design and manufacturing of the remaining joints have remained a major challenge in terms of security, cost-benefits, and structural efficiency [1, 2].

The diversified types of bonded joints and their load carrying capacities are shown in Figures 2.1 and 2.2 below.

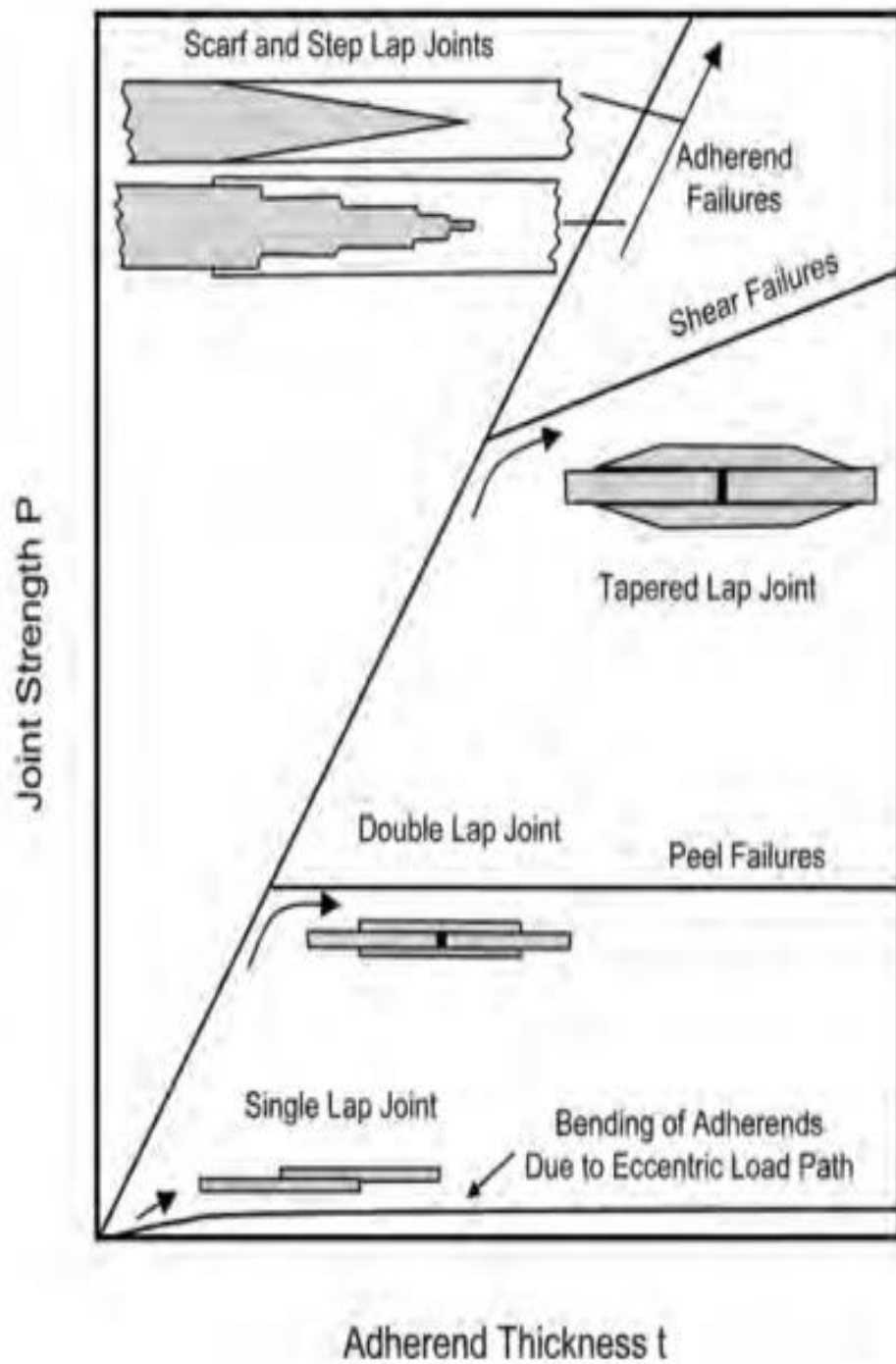


**Figure 2.1:** Effect of adherend thickness on the failure modes of adhesively bonded joints [3].

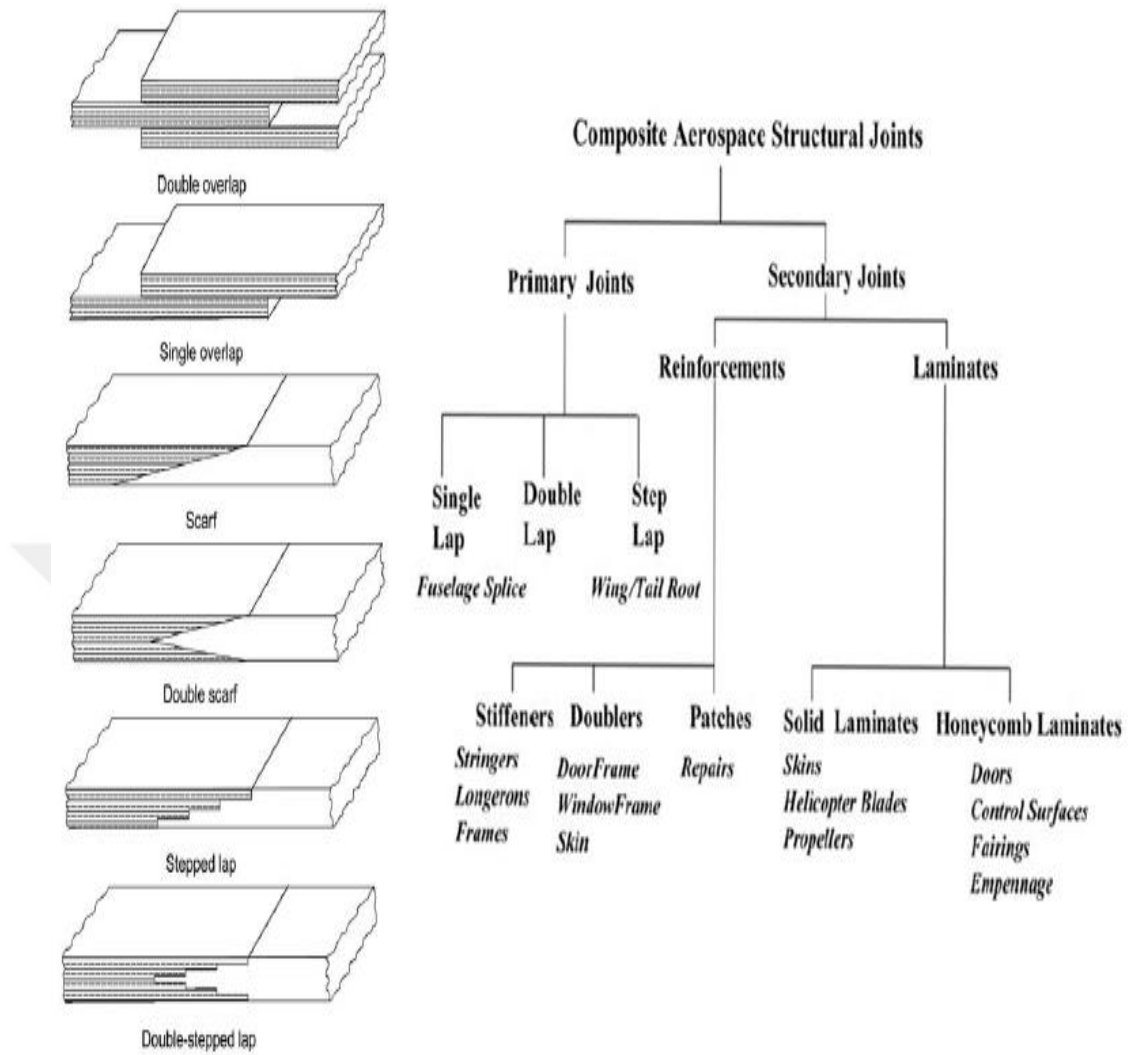


**Figure 2.2:** Classification and application of adhesively bonded joints applied and utilized during airframe manufacture [1].

### 2.1.1 Single Lap Joint (SLJ)

A single lap joint is basically an anti-symmetric assembly of two adherends of similar or dissimilar materials joined by an overlap typically with an adhesive, a bolt, or both. Figure 2.3 illustrates schematically the single lap joint while Figure 2.4 shows the stress distributions along the overlap of the joint.

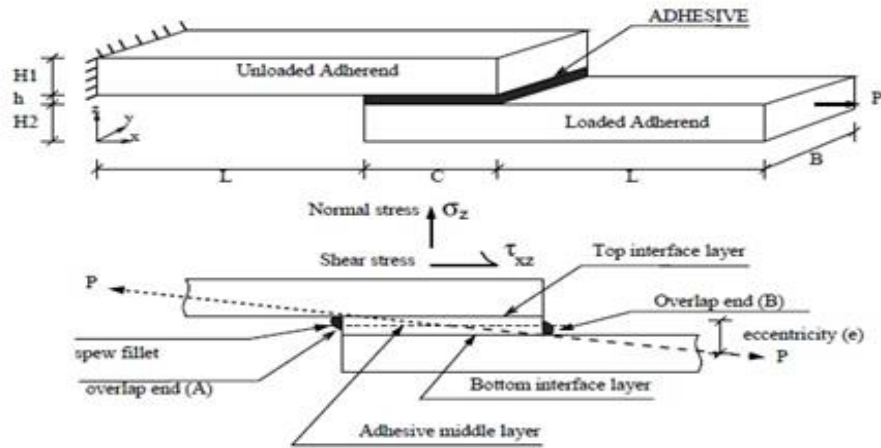


Figure 2.3: Notation for the single lap joint.

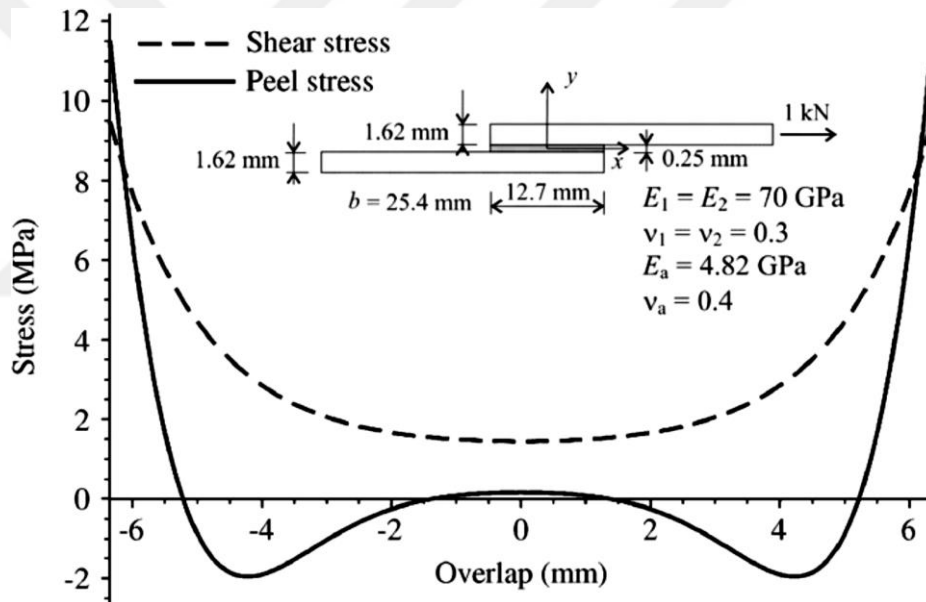


Figure 2.4 : Interlaminar stress in an adhesive[4].

### 2.1.2 Adhesive Joint (ADJ)

Adhesives are materials that help other materials bind together [5]. The first binders used by humans were from plants and animals. The 1940s introduced synthetic polymers. Today, they are as good as any industry because they effectively combine different types of materials and help to ensure connectivity [6].

After the adherends are bonded, a region called an interface is formed. It has more different properties than the adhesive and the adherend, which can affect the

## Chapter 2

mechanical properties of the joint. The interface is the contact boundary between the adhesive and the adherend, as shown in Figure 2.5. Due to the environment and the surrounding situations and reality, the strength of the bonding interface changes over time with the strength and durability of the entire joint [6, 7]. (further details are presented in Section 2.2.1)

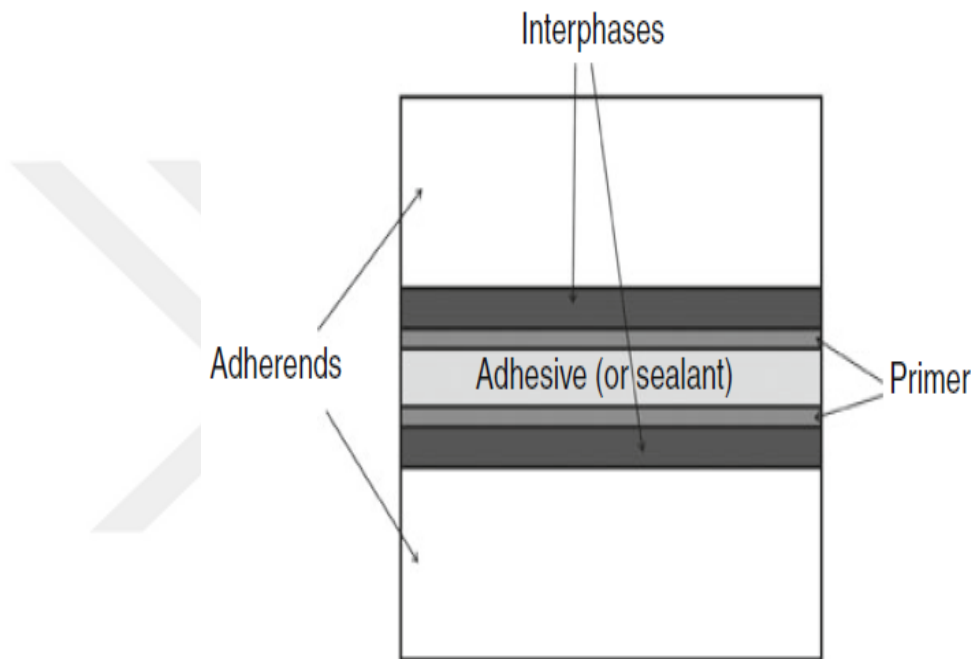


**Figure 2.5:** Adhesive joint interphase [6].

### 2.1.2.1 Adhesion Mechanisms

Intermolecular forces create an opportunity for the material to meet in close contact with the attractant. This attraction is called adhesion. Cohesion involves an intermolecular force within the material. In both cases, the intermolecular force is mostly the van-der-Waals force [6].

Several theories have explained the adhesion mechanism. These include Adsorption Theory, Diffusion Theory, mechanical Theory and Electrostatic Theory, as shown in Figure 2.6 [8]. The close contact between the intermolecular interfaces produces the so-called adsorption force. These are always present in the adhesive rather than the forces described in the case studies on which the forces described by

other theories depend. In the case of adhesives, the factors that affect the spreading and wetting of the liquid adhesive on the surface of a substrate are very important and vital. This, however, applies to all the theories [6] .

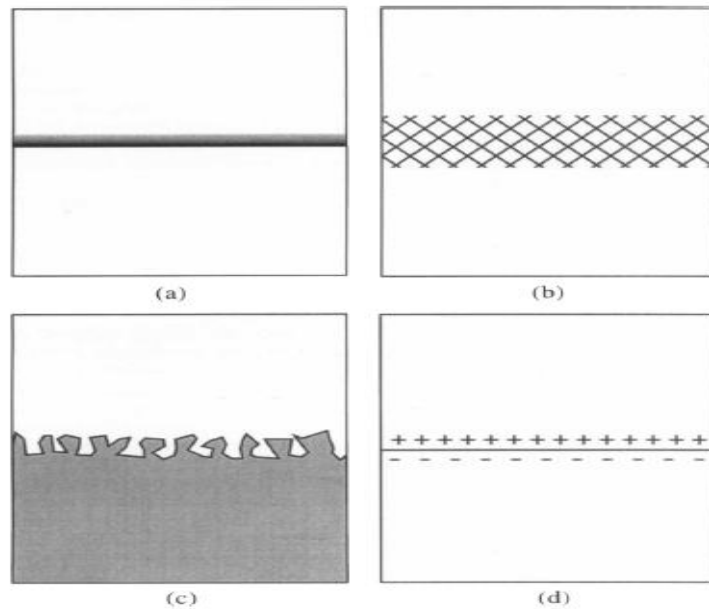


**Figure 2.6:** The illustration of (a) Adsorption Theory, (b) Diffusion Theory, (c) Mechanical Theory and (d) Electrostatic Theory [8].

### 2.1.2.2 Fracture Modes

There are three main and fundamental modes of fracture, as shown in Figure 2.7. They were first presented by Irwin's research on cracks [9]. Mode-I is known to be the tension of the normal mode or cleavage mode. This may occur through cleavage or peeling forces. Mode-II is the shear or sliding mode of cutting along a surface. Mode-III is also a shear mode or a twist mode. The shear is not on the plane along the axis [8]. A combination of these three modes is possible. Mode-I is the most common mode of fracture in engineering applications and the mode with the lowest isotropic material fracture energy. Cracks can propagate normally to the maximum principal stress level [10]. There are differences between brittle and ductile systems. In Mode-I at loading in brittle systems, micro-cracks appear in front of the crack tip when joining and expanding the spread of the cracks. For ductile systems, the plasticization of the crack tip region precedes crack propagation [11]. When considering an adhesive joint, the load is usually a mixed mode between Modes, I, II and III, hence cracks are often

limited by the adhesive layer or interface, regardless of the orientation of the adhesive layer to the applied load [10]. In Mode-I, rigid adhesives are generally weaker, but stronger in the other two, whereas rubber adhesives are stronger in Mode-I but have a higher creep rate in the other two [8].

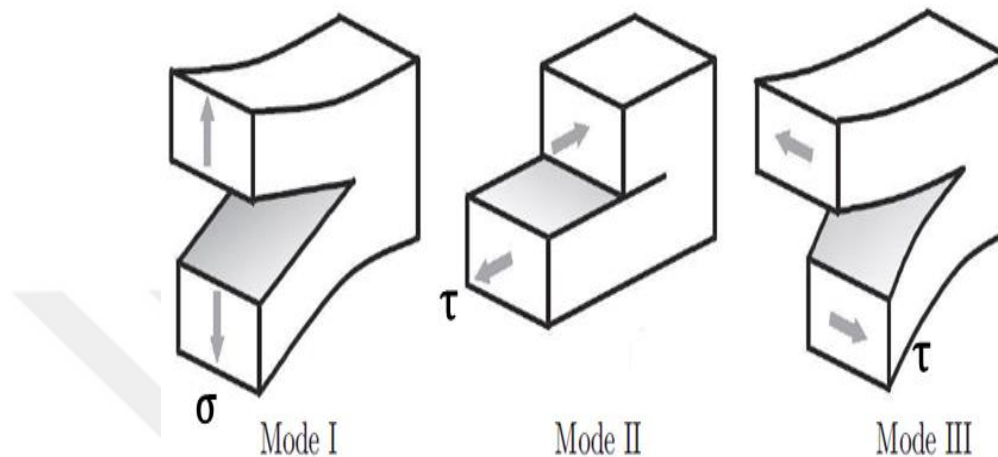


**Figure 2.7:** Mode-I, Mode-II, and Mode-III crack propagation modes. [11].

### 2.1.2.3 Failure of Adhesive Joints

In the case of examining the failure of the joint, it is important to consider the path of crack propagation. This leads to three types of bond failures. If the bonding failure occurs in the interphases or close to them, then it is asserted that there is an adhesive failure. If the fracture occurs on the adhesive layer, then the failure is cohesive. Combinations of these two fractures are possible. Weakness of the joint can be revealed by investigating the position of the crack [10]. The location of the cracks is affected by surface structure. In the smooth surface, failure occurs near the interface or at the interface. The failure is often cohesive for a rough surface. The reason for cohesion failure is the yielding of the fiber tips of the polymer. Plastic deformation rises by the yielding which results in a higher fracture energy than a smooth surface [6, 12]. Figure 2.8 shows the different types of failures.



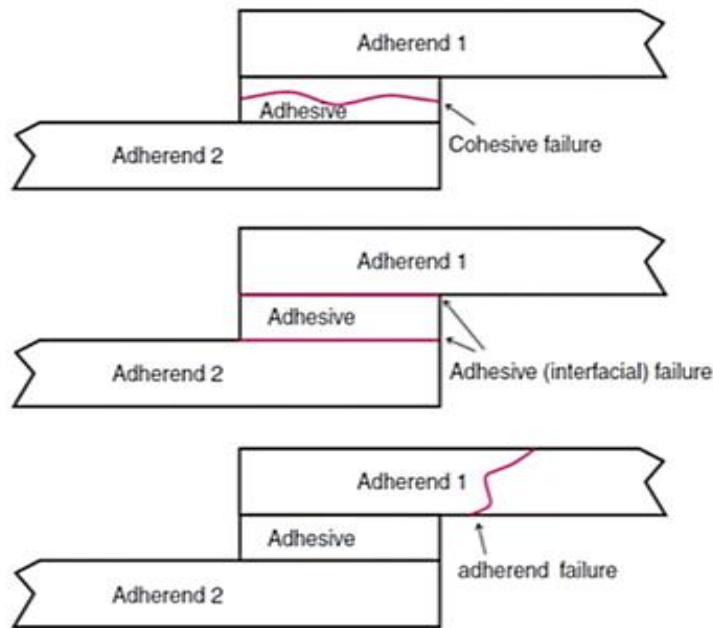


**Figure 2.8:** Failure types of adhesive joints [6].

The strength of an adhesively bonded joint depends on many parameters, such as:

- 1- Surface of the adherend: The surface of adherend should always be clean and slightly roughened so that the adhesive and the adherend can have good adhesion.
- 2- The overlap length.
- 3- The material properties (for adhesive and adherend)
- 4- The thickness of the adhesive and adherends.

Many parameters do enhance the adhesive joint strength as follows:

- Rounding the corner of the adherend along the overlap edge

Stress concentration at both ends of the overlap is the most common obstacle in the adhesive SLJ. To overcome this problem, rounding the corners of the adherends along the overlap length helps to reduce the peel stress at the edges of the adhesive layer. However, a stress analysis of the adhesive layer can only be performed numerically (Figures 2.9) [13, 14]. (further details are presented in Section 2.2.4).

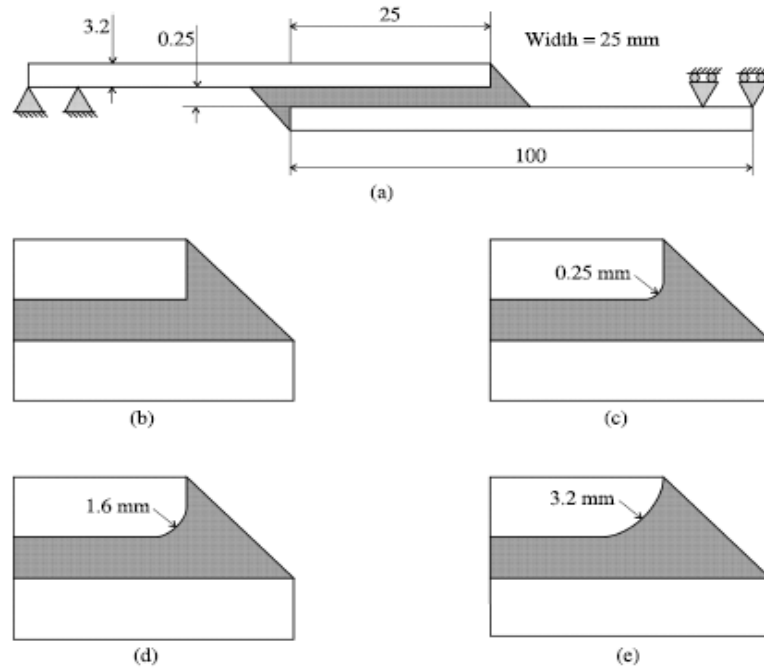


**Figure 2.9:** Bonded SLJ with different rounding radius. (a) Joint geometry (b) Sharp corner (c) Small radius (d) Medium radius (e) Large radius [13, 14].

- Spew fillet

Spew fillet is termed as the portion of adhesive that is forced out from the lap area and shapes a blob at the overlap ends as the two adherends are assembled (Figure 2.10). A spew fillet always presents in the adhesive joint, but it is often overlooked in the stress analysis of adhesively bonded joints. Obviously, the presence of spews can reduce any peak stresses, thereby increasing the strength of the joint and preventing the early occurrence of cracks. However, the reduction in peak stresses is related not only to the existence of a spew fillet, but also to the shape and size of the spew fillet [15]. (further details are presented in Section 2.2.4).

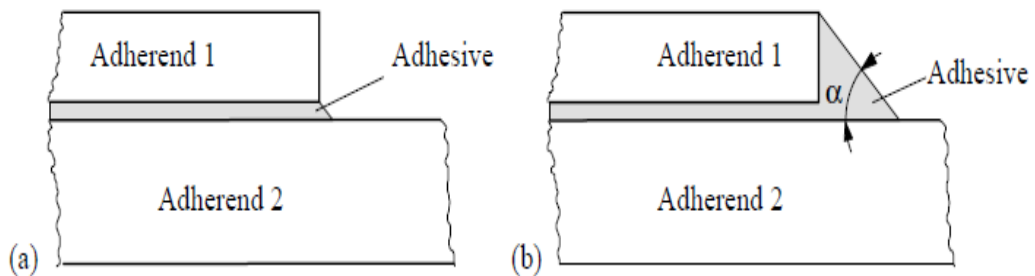


**Figure 2.10:** Shape of the spew fillet (a) at the end of the adhesive layer; (b) covering the adherend end [15].

- Tapering (chamfering) the adherends

Tapering (or chamfering) refers to the reduction of the edge thickness of the adherend at the unloaded ends, which makes the edges sharp (Figure 2.11). It is noteworthy that the presence of tapering reduces the peak stress, thereby increasing the bond strength by reducing the peel stresses that cause the cracks to initiate at the edge of the overlap [16, 17] (further details are presented in Section 2.2.4).

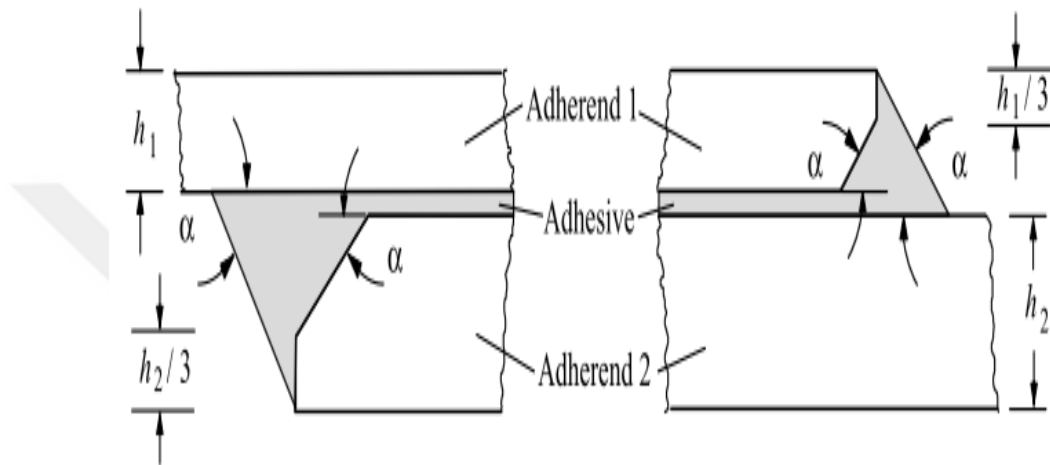


**Figure 2.11:** Chamfering of the unloaded ends of the adherends [16].

- Joggling the adherends

Bending of the SLJ is due to eccentricity, which in turn develops stresses in the thickness direction of the adhesive layer. These stresses are defined and referred to as peel stresses. The combination of peel and shear stresses on the adhesive layer will develop at the overlap ends which can affect the bonding strength. For this reason, the adherend joggle eliminates this eccentricity. Consequently, the bending moment causing the peel stresses will decrease relatively. The shape and the geometry of the joggle joint is shown in Figure 2.12. The peel stress distribution along the overlap edge for the eccentricity parameter  $K_e$  varies from 1 to -1 [18]. (further details are presented in Section 2.2.4).

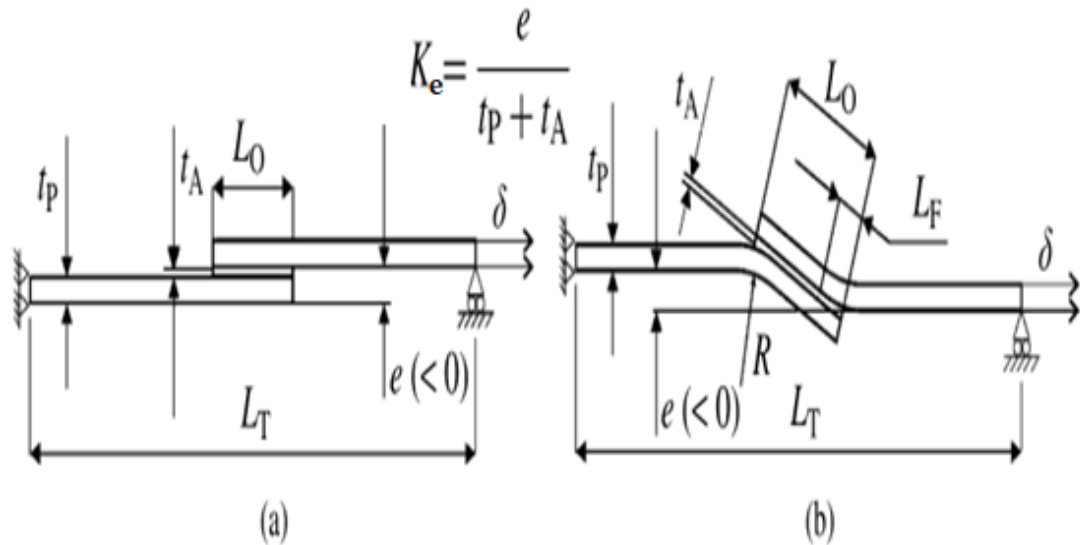


**Figure 2.12:** Geometry and dimensions of a single-lap joint with flat adherends,  $K_e = 1$  (a) and with reverse-bent geometry,  $K_e = -1$  (b) [18].

### 2.1.3 Bolted Joint (BJ)

Since the beginning of aviation, bolted joints have been widely used in aircraft, and even with the widespread use of composite materials, they still play a key role in aeronautical structures. In addition, with regard to high stiffness and strength, this mechanism has the ability to remove connectors for inspection and maintenance or access to hidden parts of the structure. The main advantages of bolted joints over other technologies include the ease of disassembly, the ease of maintenance and the ability to replace damaged parts. Researchers have performed a great deal of research on bolting to determine the key parameters that affect the efficiency of connections. Pragmatically, it is necessary to understand the mechanism that causes damage and failures. Bolted connections are a key structural area that must be properly designed in order to achieve the desired performance of an entire structure [19, 20].

Due to the large stress concentration, joints can be a source of faintness when the appropriate design practices are not followed. Therefore, failures usually occur at connections and interfaces, and not in the remainder of the system. In order to provide a safe and cost-effective connection design, geometries and compositional materials, which affect the strength and failure modes, are often configured at joints. The simplest type of mechanical connection is the SLJ (Figure 2.13) in which two adherends are assembled with a bolt or rivet. The key geometric variables used in the design include

the diameter of the bolt head ( $h$ ), the bolt diameter ( $d$ ), the distances from the center of the bolt hole to the edges of the adherend ( $e$ ), the width of the adherend ( $w$ ) and the thickness of the adherend ( $t$ ). Although this connection scheme may be the least heavy part involved in the loading plane, the eccentric load path can lead to an undesired bending, often referred to as secondary bending, which in turn usually results in lowering the joint strength values [19, 20]. In this research, the  $e_2/d$  ratio is constant and equal to 2.083 (12.5/6) corresponding to the fix width (25 mm) of the adherends. On the other hand, the ratio of  $e_1/d$  varies according to the overlap lengths as 1.25 mm, 2.083 mm and 3.75 mm for 15 mm, 25 mm and 45 mm, respectively. When the  $e_1/d$  ratio is below 2, the main failure is shear tear-out as long as the adherend is not sufficiently thick, so the bolt can sustain the load. If the ratio exceeds 2, the main failure is net-section tension as long as the bolt sustains the load [21] (further details are presented in Section 2.2.2).

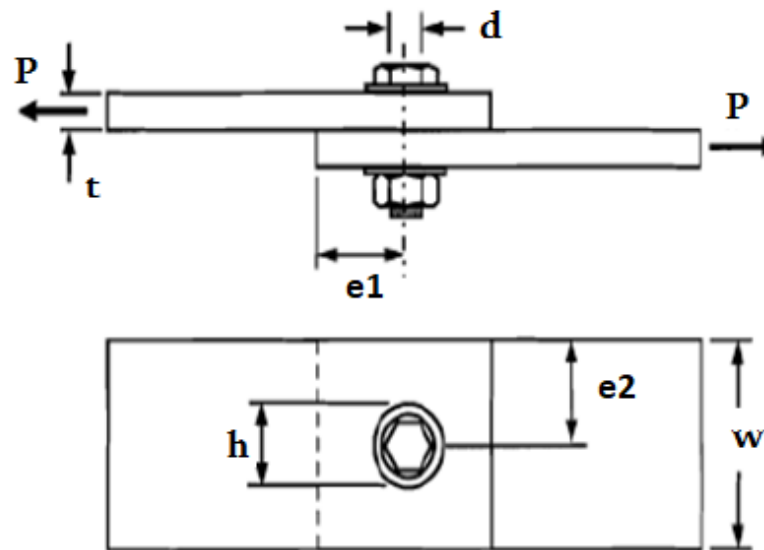


**Figure 2.13:** Bolted single lap joint configuration [20].

Among the different connection technologies, bolting seems to be the most practical option for emergency portable bridges due to its ease of disassembly. However, the bolts cause stress concentrations around the bolt holes, which can lead to the initiation of cracking. Net-tension failure of the adherend (a), bearing failure (b), shear tear-out failure (c), and bolt shear failure (d) are the four possible failure modes when the component is axially stressed, as shown in Figure 2.14 [22, 23]. These modes

correspond to the HJ modes after the adhesive layer fractures. Figure 2.15 shows the effect of secondary bending and bypass loading on the bolt hole deformations, stress concentration and contact area of the joint lap [24].

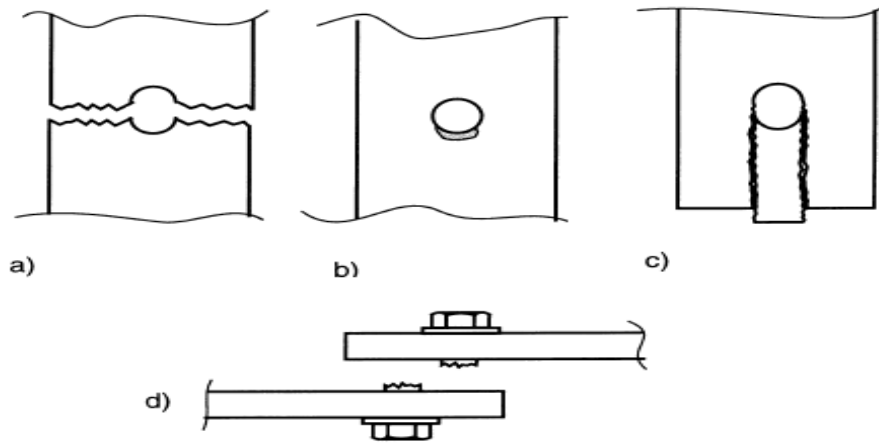


**Figure 2.14:** Failure modes: (a) net-tension, (b) bearing, (c) shear tear-out, and (f) bolt shear [22, 23].

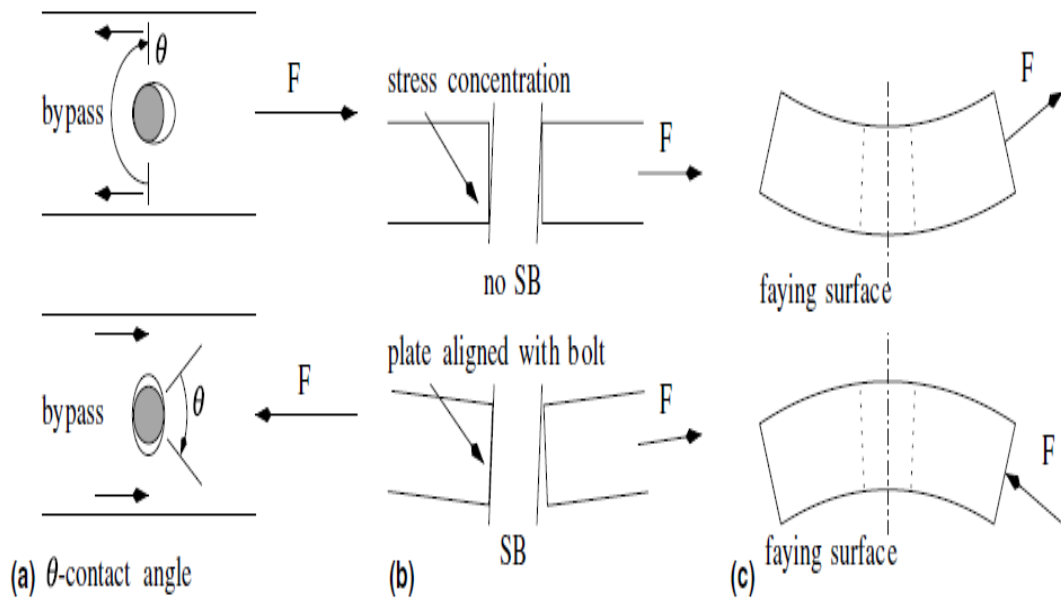


**Figure 2.15:** Effects of secondary bending (SB) and bypass load on (a) bolt hole deformations, (b) stress concentration and (c) contact area of the joint lap [24].

### 2.1.4 Hybrid Joint

A hybrid joint is referred to as a combination of two or more joining techniques that has the capacity to create a joint superior to the strength obtained from only one technique. The most common mixed joints include adhesives and fasteners (rivets or bolts) (Figure 2.16) (further details are presented in Section 2.2.3) [25].

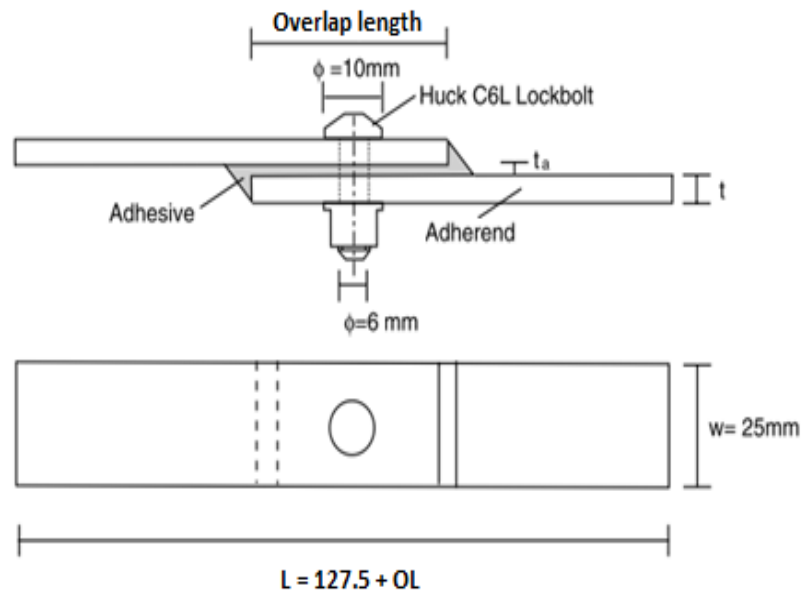


**Figure 2.16:** Test specimen geometry for hybrid joint [25].

### 2.1.5 Aluminum Alloys

In this study, the 6061 and 7075 series of aluminum alloys were used as adherends. Alloys of aluminum are cost-effective in various structures, among them the automotive industry, the aerospace industry, mechanical, electrical and structural construction, cookware, electronic enclosure covers, cryogenic pressure vessels, and many others. Aluminum is non-ferromagnetic and is very important in the power and electronics industries. It is non-inflammatory and is very important in applications involving the exposure of flammable or explosive substances to ores. Aluminum is also nontoxic and is commonly used in food and beverage containers. It appears attractive and can be soft and shiny and it can be almost any color or texture [26].

The 6-series alloys, in which magnesium (Mg) and silicon (Si) are the major alloying elements are commonly used in construction, extrusion and automotive components. The alloys in the 6-series usually contain silicon and magnesium,

generally in the form of magnesium silicate ( $Mg_2Si$ ). Although unlike most 2-series and 7-series alloys, 6-series alloys offer good formability, weldability, machinability and corrosion resistance, and they are medium strength. The alloys in this heat treatable group can be tempered as T4 by tempering (solution heat treatment but not heat treated by precipitation) and are strengthened after the formation of complete T6 properties [26].

The 7-series alloys are a group of alloys where zinc is the main alloying element (although other elements such as copper (Cu), magnesium (Mg), chromium (Cr) and zirconium (Zn) may be specified) for strength applications. 7-series is the strongest aluminum alloy, with yield strength equaling or exceeding 500MPa. A zinc content of 1% ~ 8% is the 7-series alloy of the main alloying elements. When adding a smaller percentage of magnesium, the alloy can be heat treated in order to achieve a very high strength. Often a few other elements such as copper and chromium may be added. A dilution of scandium also improves performance. The 7-series alloys are used in fuselage structures, mobile devices, and other high-stress components. The higher strength of a 7-series alloy reduces the resistance to stress corrosion through cracking, and they (7-series alloys) are often used in colder conditions to provide better combinations of strength, corrosion resistance and fracture toughness [26]. Table 2.1 presents the percentage of material composition for AL6061 and AL7075.

**Table 2.1:** Percentage of material composition for AL6061 and AL7075 [26].

	<i>Al</i>	<i>Si</i>	<i>Cu</i>	<i>Mg</i>	<i>Cr</i>	<i>Zn</i>
AL6061	97.9	0.6	0.28	1	0.2	-
AL7075	90	-	1.6	2.5	0.23	5.6



## **2.2 Literature Review**

### **2.2.1 Adhesive Joint**

In principle, the spew fillet is considered to be and regarded as a benign advantage in ADJ and hypothetically, it increases the strength of the SLJ. In fact, it is difficult to prevent the spew fillet due to the squeezing of the adhesive. Numerous publications have investigated the effect of spew fillets on strength and the manner in which peel stress is reduced.

Clearly, the presence of a spew fillet reduces the peak stress at the edges of the overlap, thereby increasing the strength of the joint and preventing the early occurrence of cracks [15, 16, 27-31]. In addition, other researchers have studied the effects of rounded or tapered adherends on reducing the peel stress [13, 14, 32, 33]. When two adherends are adhered, a portion of the used adhesive is extruded from the overlap area and spew fillets are formed on the overlap ends of the unloaded parts of the adherends.

Liao et al. [34] found that as the thickness of the adhesive layer increases, the fracture energy at the joint area increases in ductile adhesives; however, it was the opposite case for the brittle adhesives. In addition, numerical results revealed that the ductility of the adhesive rises with an increase in adhesive layer thickness [35].

Mohan et al. [36, 37] studied the effect of the bonding method between the co-cured and secondary bonding joint method under Mode-I and mixed mode loadings. They found that the strength of the co-cured bond joint was lower than that of the secondary bond joint under both loading conditions.

Castagnetti et al. [38] studied the effect of different thicknesses of adhesive layer for single lap and tubular butt joints, revealing a decrease in the strength as the adhesive thickness increases (Figure 2.17). The reduction in bond strength was attributed to the thicker bond lines that contain more defects such as voids, micro-cracks and higher interfacial stresses [39-42].

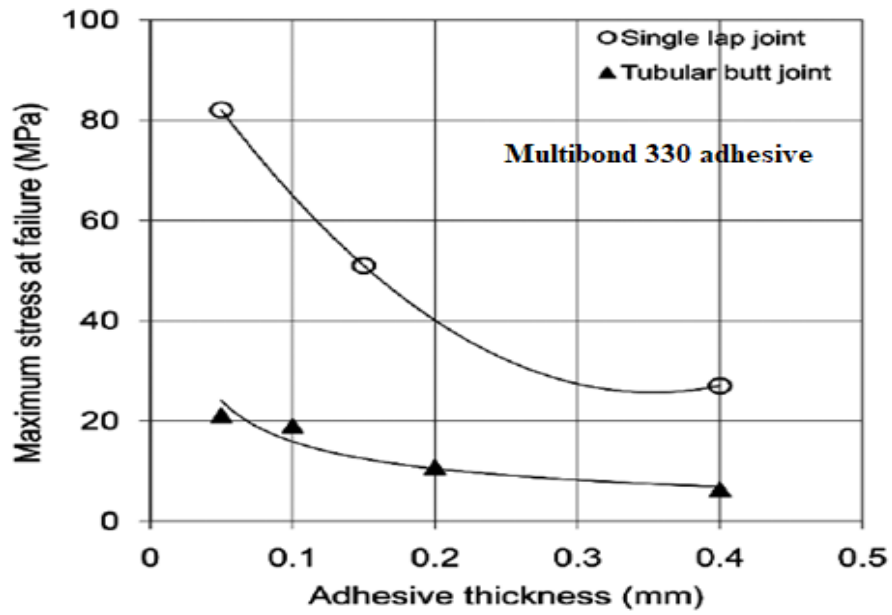


**Figure 2.17:** Maximum stress at failure vs. adhesive thickness [38].

Lucic et al. [43] studied bonded single lap joints for aluminum to optimize the OL ratio (OL / 30 mm overlap width from 0.5 to 2). The experimental results were compared with the numerical data released by ANSYS software. The research revealed that the optimal overlap ratio is equal to 4/3 (Figure 2.18).

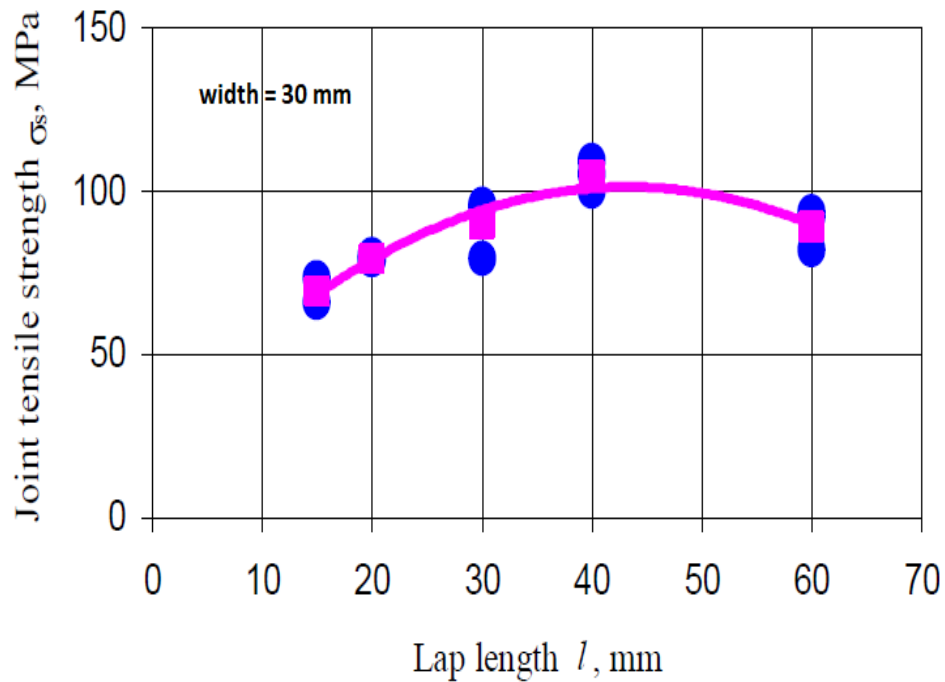


**Figure 2.18:** Experimental results of strength of joints vs. OL [43].

Seong et al. [44] studied the impact of bonding pressure, the OL, the thickness of adhesive layers and the type of adherend material on failure load and mode of composite-to-aluminum adhesively bonded SLJ. The investigation concluded that:

- 1- Applied pressure to the bonding area should be higher than or equal to 3 atmospheres (Figure 2.19).
- 2- The increase of overlap length increases the strength, just so long as the overlap length to width ratio is not greater than one (Figure 2.20).
- 3- The thicker the adherend, the higher the strength of the adhesive joint. However, when the thickness of adherends is doubled, the increase in strength is negligible.
- 4- Failure modes were complex, but the main failure was the delamination of the composite.

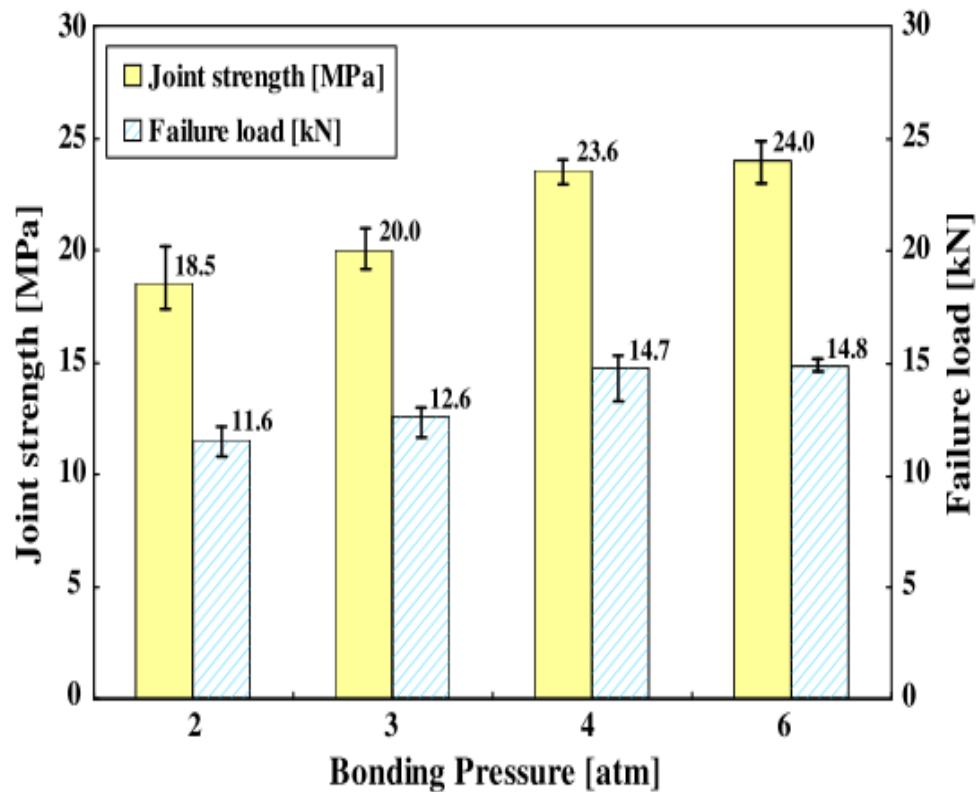


**Figure 2.19:** Strength and failure loads of bonded joints with different bonding pressures for 25 mm overlap length [44].

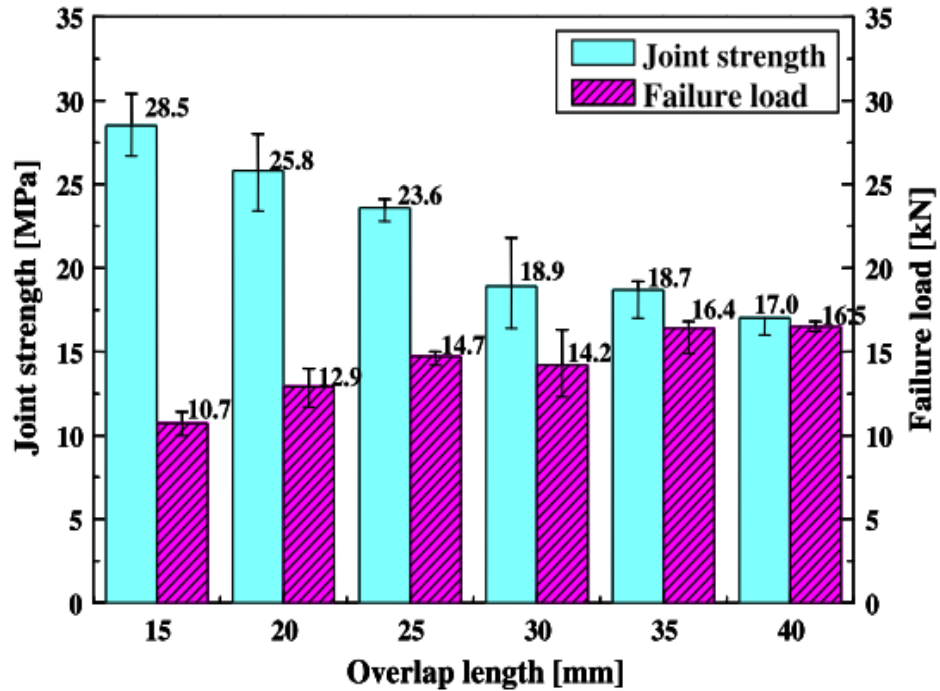


**Figure 2.20:** Strength and failure loads of bonded joints with different OLs [44].

Samaei et al. [45, 46] performed experimental and numerical investigations on the influence of geometric parameters and mechanical properties of adhesives in single lap aluminum structures under tensile loads using ANSYS software for the numerical analyses. The outcomes indicate that by increasing the adhesive thickness, the stress concentration decreases in the areas that are prone to yield if a flexible adhesive is used instead of a rigid one, and effective stresses along the overlap length are also reduced.

Reis et al. [47] compared the tensile and shear strengths of bonded SLJs with three different adherends, namely carbon/epoxy laminated composites, high elastic limit steel and 6082-T6 aluminum alloy. The study concluded that:

- 1- The increase in the adherends stiffness increases the strength of the joint, although the effect of yield stress is further pertinent. The less stiff adherends were found to accomplish strength of the joint of the dissimilar adherends (Figure 2.21).
- 2- The increase in stiffness of the adherend reduces the rotation of the joint and establishes a more stable stress distribution in the adhesive layer (Figure 2.22).

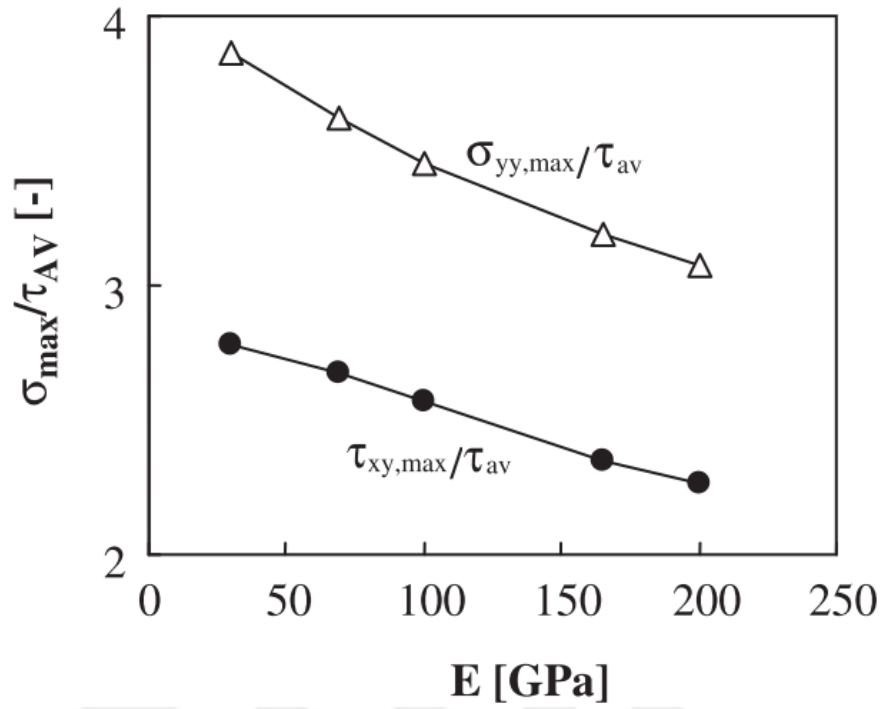


Figure 2.21: Effect of the elastic modulus on the strength of the joint [47].

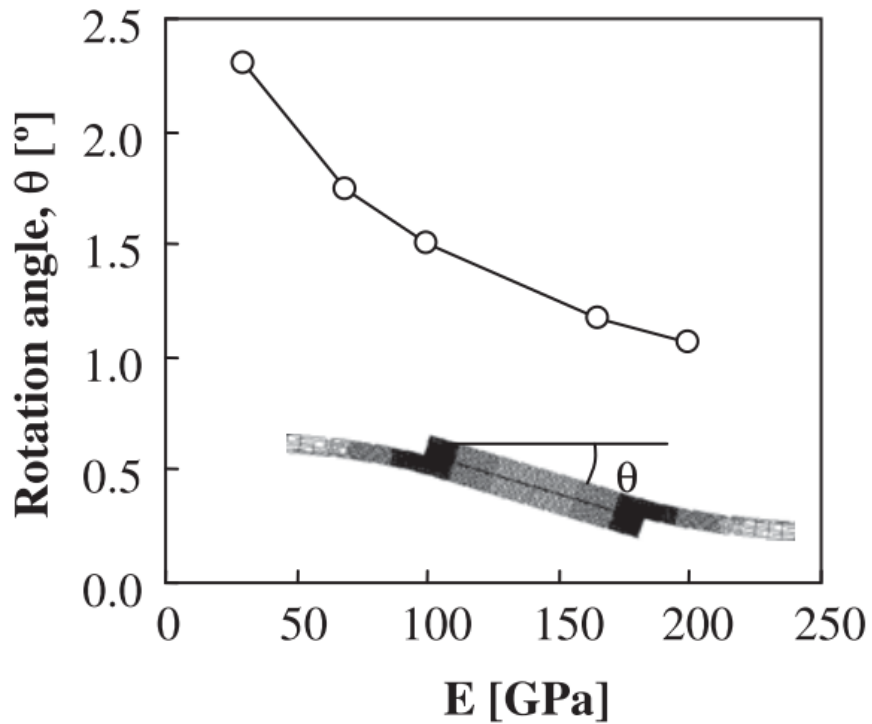
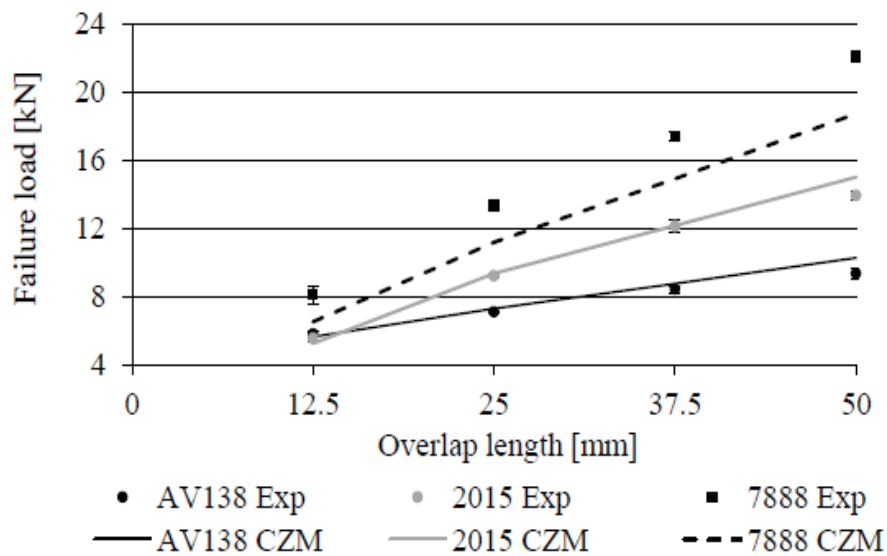


Figure 2.22: Effect of the elastic modulus on the rotation angle of the joint [47].

Campilho and Fernandes [48] investigated the performance of brittle (Araldite® AV138), moderately ductile (Araldite® 2015) and largely ductile (Sikaforce® 7888) adhesives in single-lap joints between aluminum adherends with varying values of overlap length. Their experimental study was accompanied by a detailed analysis of finite elements based on cohesion zone modeling (CZM) (via *ABAQUS*® CAE). The SLJ bonded with high strength and high ductility polyurethane (Sikaforce® 7888) which showed the highest strength and the maximum load improvement as the OL increased (Figure 2.23).



**Figure 2.23:** Numerical (CZM) and experimental results of the failure loads vs. the overlap lengths for different adhesives [48].

Ribeiro et al. [49] examined the effect of different adhesives (brittle and ductile) and the overlap length values on strength of the SLJ between aluminum and carbon-epoxy composites. The study was conducted experimentally and numerically and the following results ensued:

1. The brittle adhesive has better strength than the ductile adhesive when the overlap length equaled 10 mm (Figure 2.24a and 2.24b).
2. The flexible adhesive strength increases proportionally with the increasing OL, while the brittle adhesive strength does not change significantly (Figure 2.24a and 2.24b).
3. Although the peeling and shearing stress distributions at the middle plane of

the adhesive increases, precisely at the joint edge, with the increase of the OL, it is more uniform away from the overlapping edges (Figure 2.25).

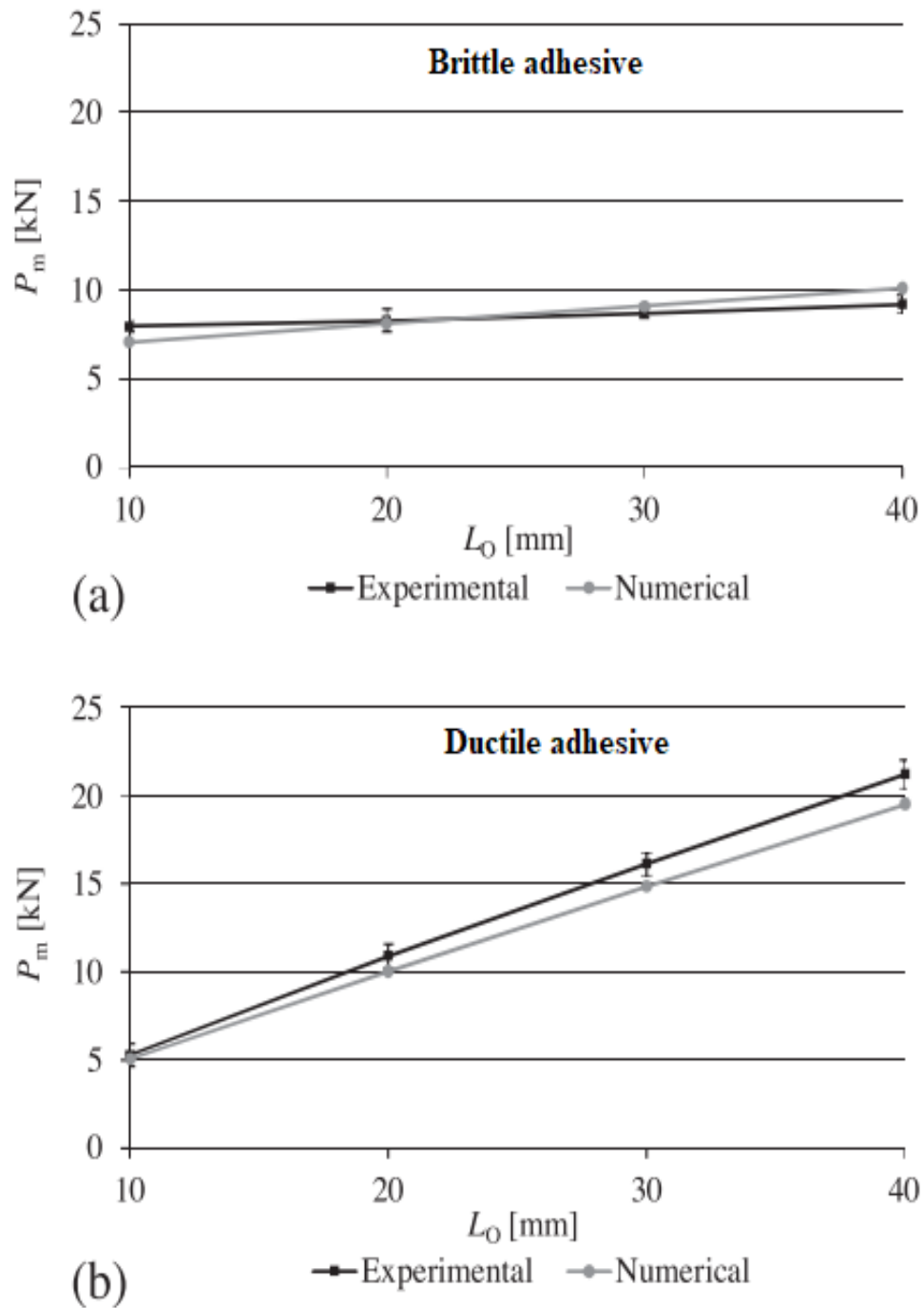


**Figure 2.24:** Experimental and numerical failure loads vs. different overlap lengths of adhesive joints with adhesive XNR6823 (a) and XNR6852 (b) [49].

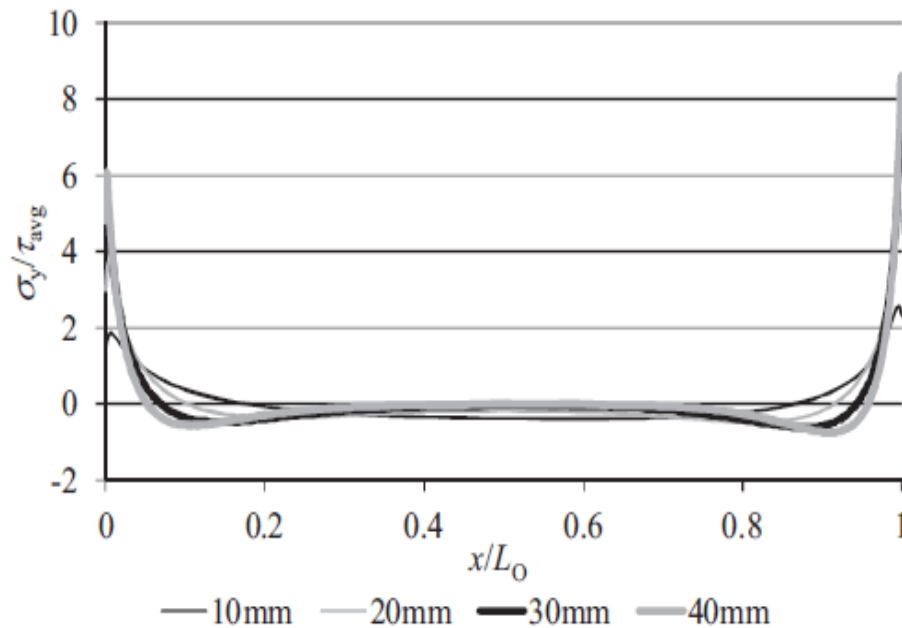


**Figure 2.25:** Peeling stress distributions at the adhesive mid-thickness for different OLs[49].

Similarly, Wei et al [50] observed that the failure load upsurge linearly with the increase of the OL, while the normalized failure load, equal to the failure load divided by the OL, reduced dramatically with the increase of the OL, demonstrating that increase in the OL might toughen the joint by a limited level.

Papanicolaou et al. [51] investigated the unbalanced Boron/Epoxy-Aluminum 2024 T3 single lap joints bonded with high strength adhesive subjected to tensile loading, after being exposed to a corrosive environment. It was found that the overlap length and the aging conditions directly affected the joint tensile strength. When the overlap length increased, the maximum shear and normal stresses were found to increase, but the lap shear strength was not proportional to the overlap length. Turan and Pekbey [52] investigated the failure behavior of single-lap joints with different types of adhesives for increasing overlap length. It was observed that when the overlap length was increased from 10 mm to 40 mm, the failure loads were increased by 48–82%. Karachalios et al. [53] observed that for high strength steel adherends as the overlap became longer, the adhesive global yielding was replaced by a failure due to high local shear strains in the ADJ.

Adams et al. [54] studied different bonded SLJs using Finite-Element Analysis (FEA). They also presented elastoplastic and non-linear FEAs involved in adhesive



bonding [55, 56]. Their work highlighted the development of FEA interested in adhesive bonding. The use of explicit finite element codes to solve the equations of motion for each degree of freedom allowed very large models to be simulated within a reasonable time of execution, for example, a detailed process structure containing even over one million degrees of freedom. The limits of freedom were due to the computer memory limitations and the need to maintain the solution times.

While compared with the finite-element method used in the numerical analysis, Sugiman and Ahmad [57] revealed that the CZM method was superior to the continuum damage method in predicting the degree of damage and in the computational time. A similar valuation was made by Rudawska [58], who made experimental and numerical comparisons of the peeling stress distribution in the adhesive layer for both epoxy-glass composites and epoxy-graphite composites by using the same adhesive substance. The study indicated that, using the CZM law (traction-separation) embedded in *ABAQUS* gave reasonable results compared to the experimental outcomes. More researchers [48, 59-63] claimed the same in their studies.

### **2.2.2 Bolted Joint**

Mechanical bolted joints typically show four failure modes: bolt shear, tear-out shear, bearing and net tension. Mixtures of these failure modes are also possible. The strength of mechanical joints is affected by several parameters. The parameters that have the most effect on the failure mode of a bolted joint, are the distance from the bolt to the edge of the OL and the width of the connection. The structure is also affected by the clearance between the bolt and its hole. Friction between the bolt head and the adherend also affects the strength of the joint. Therefore, the investigation of all these parameters is crucial in order to design bolted or hybrid joints.

Numerous attempts have been made to investigate numerically and experimentally the effects of the geometry and properties of the joints on the performance and strength of the SLJ. Ekh et al. [24, 64] conducted a numerical study of the effect of bolt-to-bolt distance on secondary bending and strength, as well as the analysis of load transfer in multi-row bolted joints. A similar study was conducted in [65, 66]. McCarthy et al. [67] conducted an experimental study using a single lap joint

## Chapter 2

with a single-finger telescopic bolt. The results showed that the load-receiving delay was proportional to the amount of clearance between the bolt and the hole. Later, their goal was to replicate the observed behavior with a three-dimensional finite-element model, using the same connection configuration without preloads in the bolt. The model imitated the effect of clearance seen in the experiment with accurate outcomes [68]. As a result, they extended the model in order to study the effect of the clearances in multiple rows of bolts [69]. Since all these studies had already been shown to be good and with auspicious results in joint behavior investigations, it is clear that these similar finite element studies can be applied to other joint parameters.

In the past, there were only a few efforts focusing on the analysis of stress concentrations around bolt holes using the finite-element method. Ireman [70] examined contact pressure distribution around the bolt hole of bolted single lap joint of composite and aluminum adherends, while using a single bolt, protruding or countersunk bolt. Meanwhile, the material properties in the composite were uniform. It was impossible to back-calculate the stress state of each ply. McCarthy et al. [71, 72] studied tangential and radial stress distribution around bolt holes in bolted SLJ composites with protruding or countersunk bolts. The outcomes of the uniform and inhomogeneous material properties were obtained and the effects of the clearances on the stress distribution were studied.

The most common method of measuring bolt clamping force is to use a torque wrench. While this method is easy to implement, it proves to be very inaccurate because it relies on the estimation of the coefficient of friction between nuts, plates, and bolts. More advanced methods use strain gauges which can be applied to locations between nuts and plates [73].

### **2.2.3 Hybrid Joint**

The knowledge on HJ technology in practice requires extensive research to reach the same level of knowledge of bonded or bolted joint technologies. The study of the HJ began with Hart-Smith [74]. This study revealed that HJs with fibrous composite structures did not offer any significant increase in strength compared to bonded joints, which could be explained by the low fraction of load transferred by the fasteners. Studies by Kelly [25], Sadowski et al. [75, 76], Fu and Mallick [77], Imanaka et al.

[78], Lopez-Cruz et al. [79], Marannano and Zuccarello [80] demonstrated that the strength of HJs was higher than those of BJs or the ADJs alone.

Kelly [25] investigated the strength and fatigue life of the joints using carbon-fibre reinforced plastic adherends. The HJ were proved to have higher joint strength and extended fatigue life with a flexible polyurethane adhesive compared to the ADJ. However, the HJ in combination with a stiff epoxy adhesive offered only limited improvements in structural performance. Similar conclusions were obtained for different adherends and HJ configurations by Imanaka et al. [78], Lopez-Cruz et al. [79] and Keweon et al. [81]. Fu and Mallick [77] found that the performance of HJs was sensitive to the washer configuration. For larger washer areas, greater strength and fatigue life were obtained. The propagation rate of fatigue cracks was reduced in HJs when compared to ADJs. Lee et al. [82] tested various HJ specimens with different width-to-bolt diameter ( $w/d$ ) ratios and edge-to-bolt diameter ( $e/d$ ) ratios. It was observed that the failure loads of the HJ with a  $w/d$  ratio of 2.8 were higher than those of the adhesive joints with  $e/d$  ratios greater than 2 and less than those of the adhesive joints with  $e/d$  ratios lower than 2. In another study, Imanaka et al. [78] observed that the fatigue strength of the joints increased with a decrease in the ratio of its width-to-hole diameter. Tan [83] investigated the efficiency of the hybrid single lap joint of unidirectional prepregs with two/four bolts and the FM400 adhesive and concluded that the number of bolts influenced the load required to debond the adhesive material.

Moroni et al. [84] performed an experimental study to compare simple joints and HJs also accounting for environmental variables. It was observed that weld-bonded HJs lead to an increase in strength, stiffness and energy absorption in comparison with simple spot welding, and a strong reduction of dependence on temperature and ageing with respect to bonded joints was reported. Steward [85] tested single lap hybrid joints used for repairs and concluded that the HJ was 50% stronger than the BJ and 16% stronger than the ADJ.

Sadowski and zarzeka-Raczkowska [86] investigated the effect of three-rivet layout geometry (3 rivets as longitudinal, transverse and 1 + 2 ( $\bullet\bullet$ ) layouts) on the strength of the hybrid adhesive bonded/riveted aluminum joints and concluded from their experimental and numerical study that the hybrid joints with a rivet layout 1+2 ( $\bullet\bullet$ ) had the best strength among the three-rivet geometrical layouts despite the fact

that the three-rivet layout without adhesive had no significant influence on the joint strength (Figure 2.26). Conversely, the HJ proved to have greater stiffness, strength and fatigue life. Similarly, conclusions have been obtained when different adherends and hybrid combinations are used [78, 87].

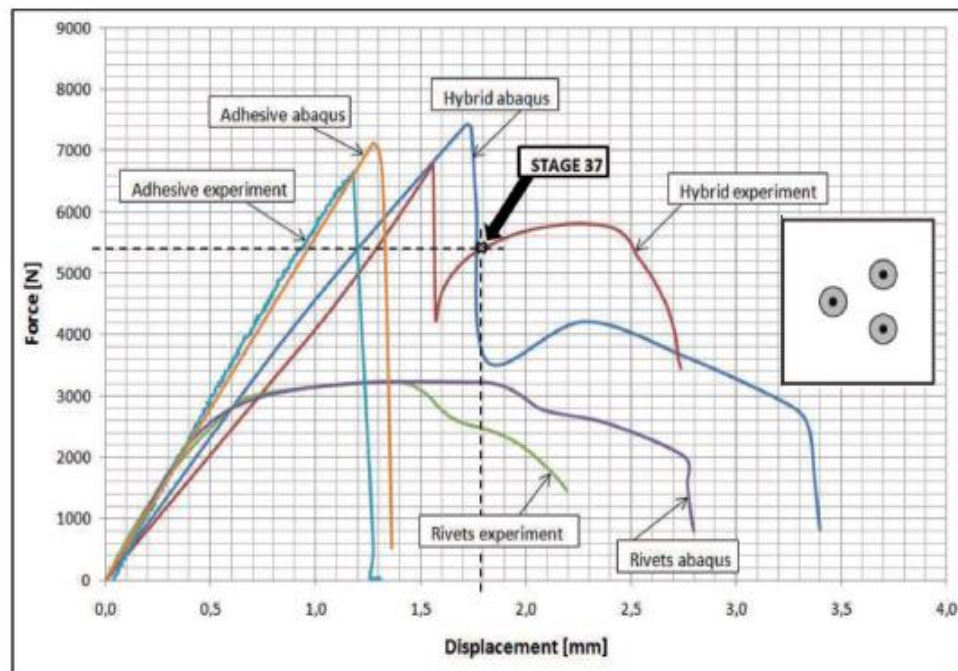


**Figure 2.26:** Numerical and experimental comparison of the force - displacement tests for 1+2 layout rivet joints [86].

Senguttuvan and Lillymercy [88] conducted experimental comparisons of the joint strength of GFRP between three types of single lap joints, namely adhesive, riveted and bolted joints. The adhesive joint was investigated with different thicknesses and overlap lengths, whereas the riveted and bolted joints were examined with 2, 3 and 4 rivets and bolts. The study was concluded with these assertions:

1. By increasing the number of bolts and rivets, the strength of the joint increases.
2. An increase in the number of rivets or bolts leads to uniform distribution of the applied tensile load on the area between the GFRP adherends.
3. Bolted joints have superior strength when compared to bonded and riveted joints.

In other studies, Pironi and Moroni [89] found that the HJ was superior to the

ADJ due to the combination of both bolted and bonded joints, while the bolting mechanism delayed the crack propagation. Karthik, et al [90] came to a similar conclusion. Their investigation of bonded, riveted and hybrid single lap joints for woven glass fiber showed that hybrid joints have superior strength. In addition, the stress-strain curve for the hybrid joint is linear, i.e., the rivets increase the strength of the bonded joint by preventing the propagation of cracks. Therefore, the joint becomes stiffer without sliding between adherends.

In addition, Yogesh and Arunkumar [91] learned that the HJ is effective when the BJ is stronger than the ADJ. However, once the strength of the BJ is lower than the strength of the ADJ, the BJ does not contribute much to the strength of the HJ. The HJ with a ductile adhesive sustained a large load. This is because the load regularly transferred between the adhesive and the bolt, as compared to the one that used a stiffer adhesive, where the load transferred only through the adhesive [92].

Hai and Mutsuyoshi [93] examined two types of double lap joint, namely the BJ and HJ. The results showed that the double lap HJ involving stainless steel bolts, adhesive bonding and V-notched splice plates is an effective technique to connect hybrid fiber-reinforced polymer laminate adherends.

Overall, it has been found that the strength of the HJ is higher than that of the BJ or ADJ alone. For the optimized joining techniques enabling highly integrated structures, the influencing parameters need to be determined. However, in none of the above studies, the effect of the adherend thickness and the adherend material as potential affecting parameters on the static strength of the HJ with respect to the BJ and the ADJ was investigated at the same time both experimentally and numerically.

### **2.2.4 Improvement of the Bonded SLJ**

Lang and Mallick [15] explored the impact of various adhesive spew fillet geometries on the peak stresses and stress distributions in adhesively bonded single lap joints using the FEM method (ANSYS). The outcomes show that:

1. In general, the spew fillet geometry causes a reduction in peak stresses.
2. Amongst all spew fillet geometries (Figure 2.27), the arc spew fillet shows the highest percentage of reduction.

3. Decreasing the angle of the incidence of the triangular geometry reduces the peak stress.

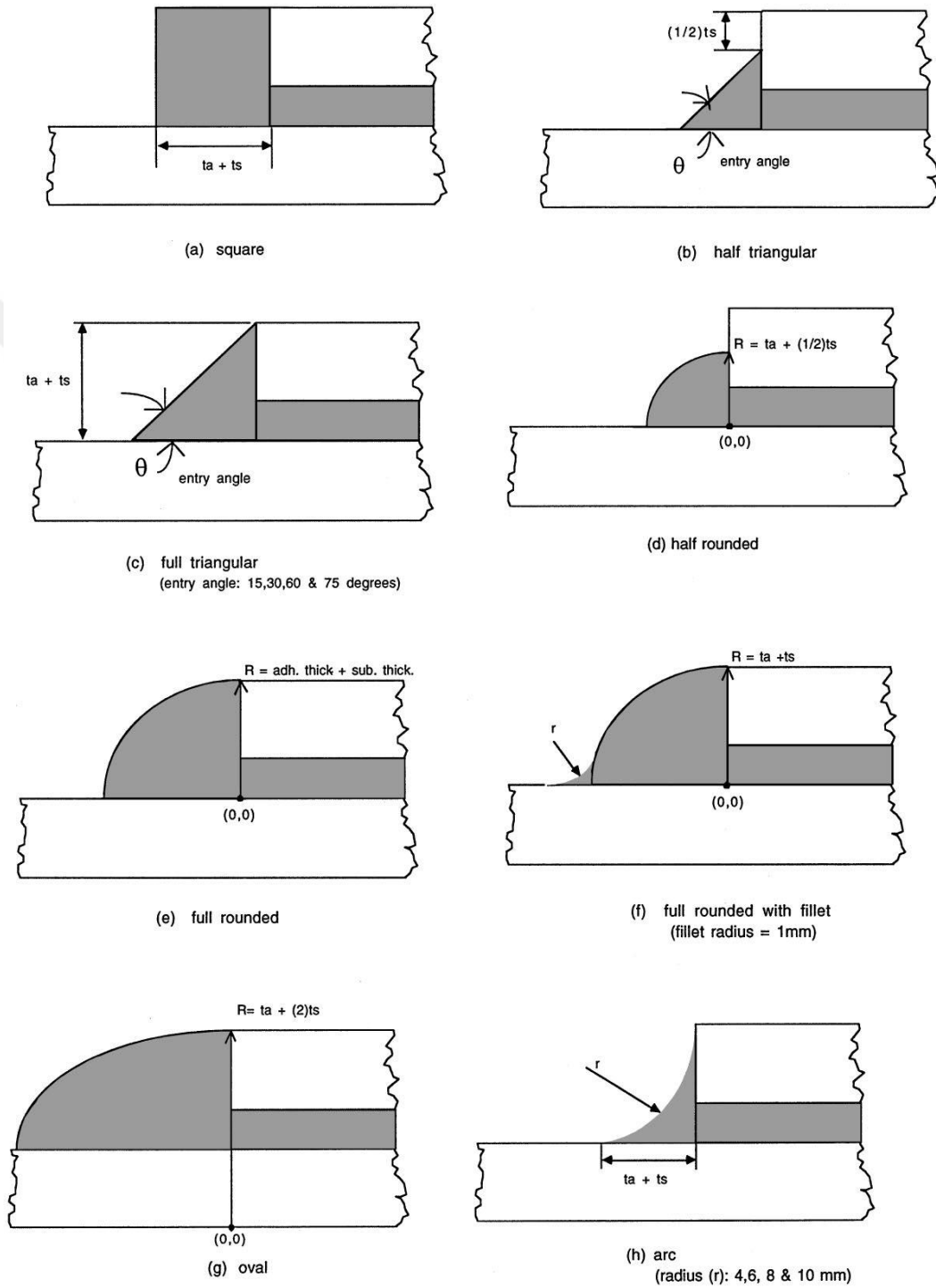
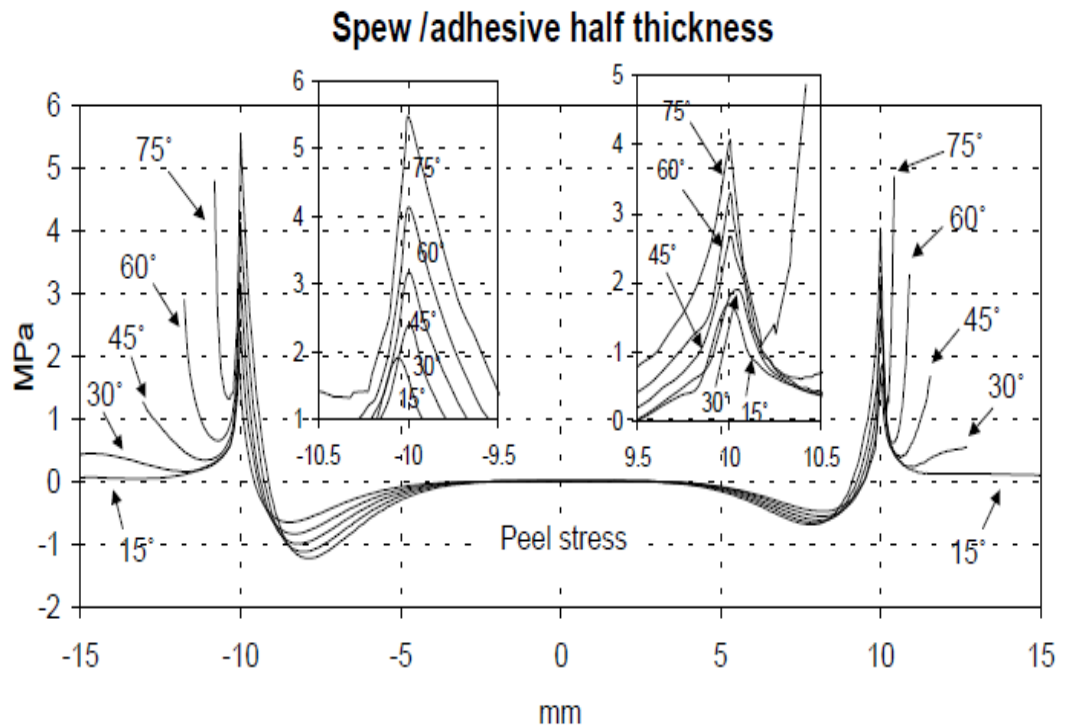


Figure 2.27: Shape and size of the spew fillet of the single lap joint [15].

Similarly, Doru et al. [30] conducted experiments and numerical studies on the effects of various spews and different adherend widths on the adhesive SLJs of aluminum. The study concluded that the spew fillet at the overlap width and variable widths of the adherend reduced stress concentration and increased the bond strength.

Belingardi et al. [16] studied the effect of using the adhesive spew fillet and tapered the ends of the unloaded adherends for bonded single lap joints of steel and FRP. Their conclusions are as follows:

- 1- The spew fillet and chamfer angles of  $15^\circ$  show the least reduction in the stresses peak. However, an angle of  $45^\circ$  for both parameters is sufficient to obtain a corresponding reduction of the stresses peak (Figure 2.28).
- 2- The results associated with the elastic behavior incidentally deduced that the ultimate strength of the joint increases as the peak stress decreases.



### Chamfer and spew / adhesive half thickness

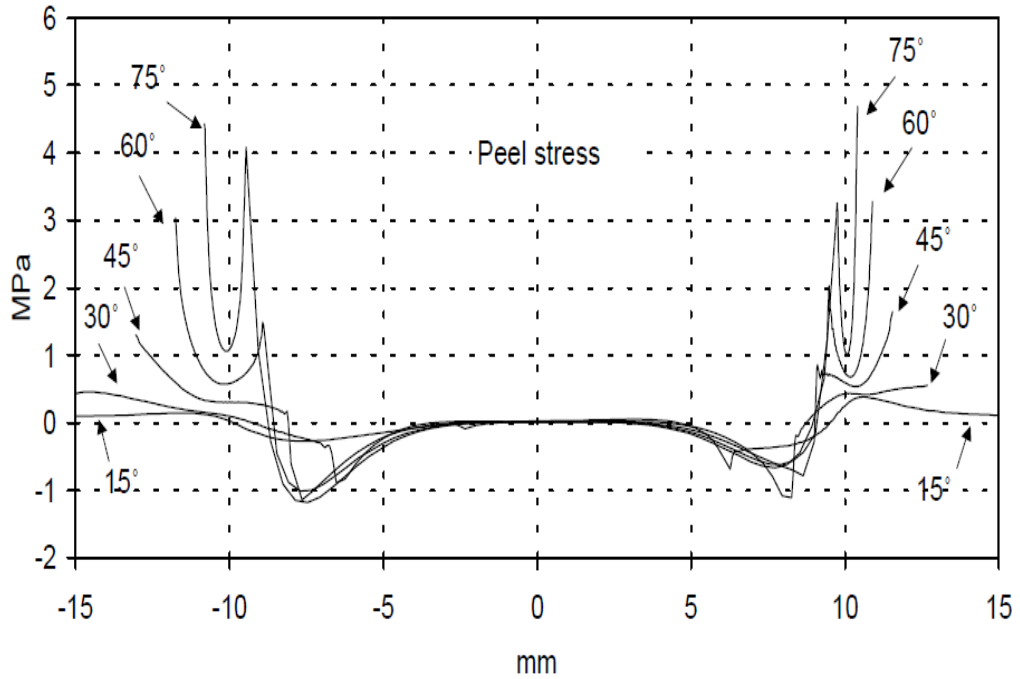


**Figure 2.28:** Effect of spew fillet and chamfering on peeling stress [16].

Solmaz and Aydın [17] studied the effect of differing overlap lengths (25.4 mm and 38.1 mm) and different taper angles ( $0^\circ$ ,  $15^\circ$ ,  $30^\circ$ ,  $45^\circ$ ,  $60^\circ$  and  $75^\circ$ ) on the strength of bonded single lap joints of CFRP. The study was conducted experimentally and numerically, and it was observed that:

- 1- The maximum strength was observed at a  $15^\circ$  tapered angle of adherends (Figure 2.29).
- 2- The least reduction of peeling stress was observed at a  $15^\circ$  tapered angle of adherends (Figure 2.30).



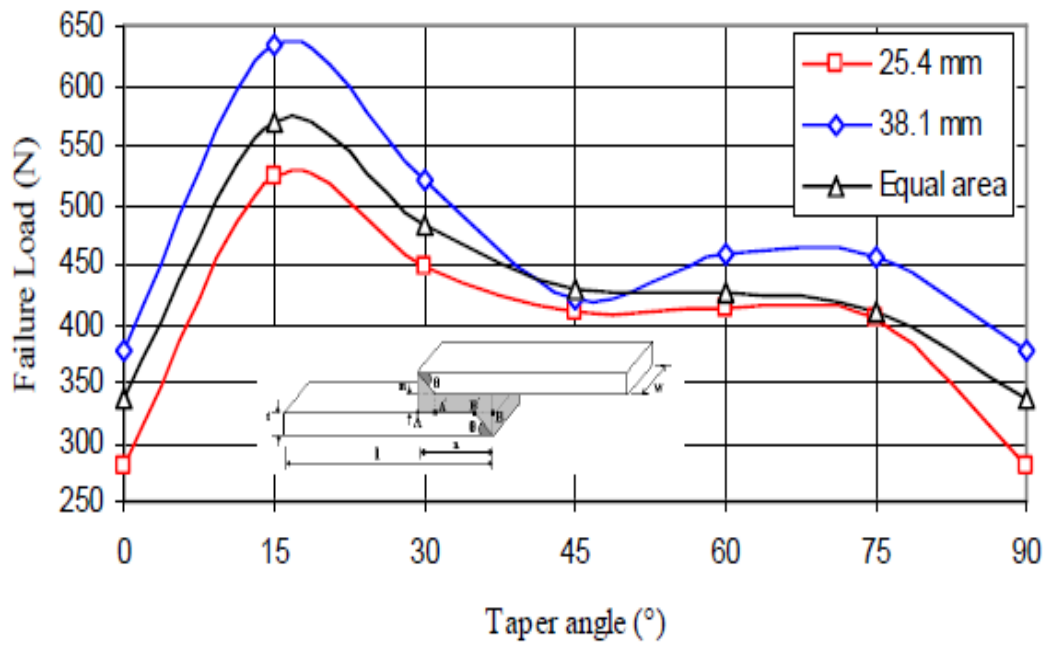


Figure 2.29: Failure load vs. taper angle for different OL using Neoxil CE92 N8 adhesive [17].

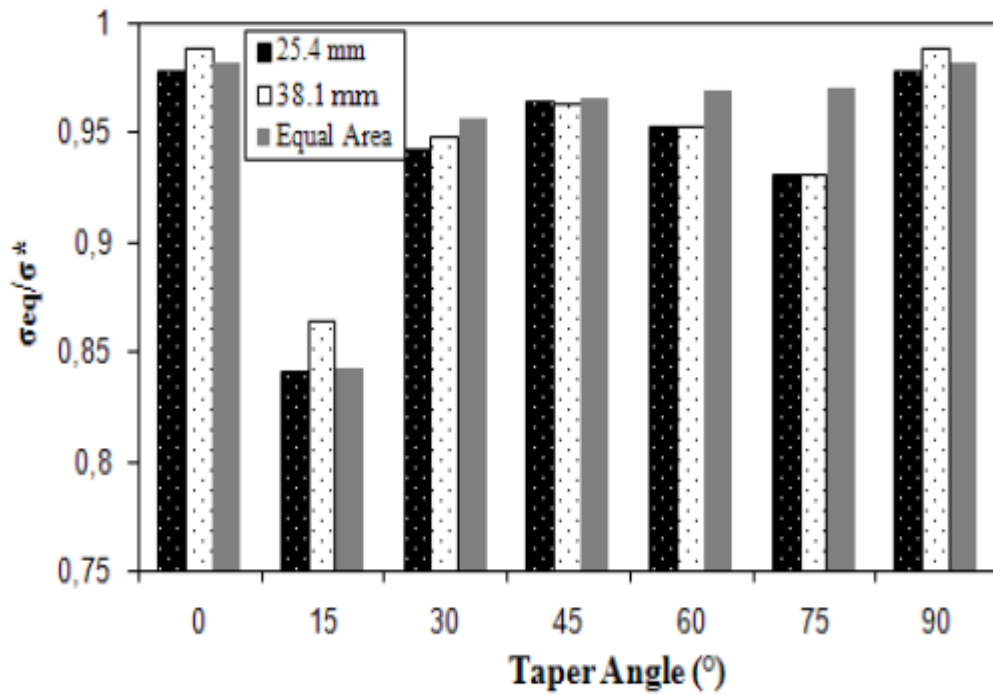
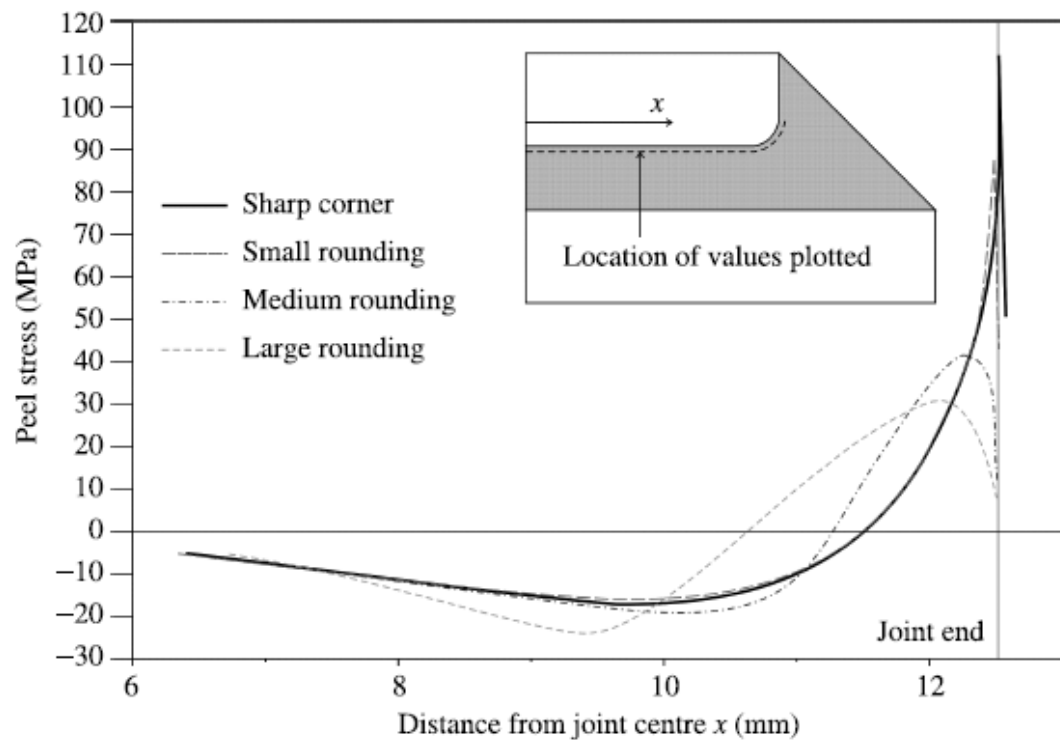


Figure 2.30: Effect of tapered angle on peeling stress [17].

Zhao et al. [13, 14, 94] investigated the stress distribution at the edge of the overlap widths of bonded aluminum SLJs using brittle and ductile adhesives. The test was conducted for different degrees of rounded corners of the adherend. The study gives a detailed stress and strain distribution around the rounded adherends using the finite-element method. It was observed that:

- 1- The adherend corner radius had a greater effect with the brittle adhesive than the ductile adhesive.
- 2- The larger the radius of rounding, the greater the drop in stress, and the further the stress peak moved toward the overlap center. The joint strength of rounded corners was increased by approximately 40% compared to the sharp corners (Figure 2.31).
- 3- The larger the rounding, the smaller the parallel portion between the adherends concentrating the load.
- 4- The edges of the fillets with a large degree of rounding become critical sources of joint failure.



**Figure 2.31:** Peel stresses in adhesive MY750 with a 20 kN applied load, close to the unloaded adherend [13, 14].

Campilho et al. [18] carried out experiments and numerical studies to evaluate the feasibility of bending the adherend at the overlapping area to increase the strength of the aluminum SLJ adhered with brittle and ductile adhesives. Various eccentricity joints were tested, including the absence of eccentricity ( $K_e = 1$  to  $-1$ ). It was concluded that the joints with  $K_e = 0$  (i.e., perfectly aligned adherends) were found to be most effective as the peel stress at the edges was reduced, whereas the joint with  $K_e = -0.5$  has the higher strength (Figure 2.32).

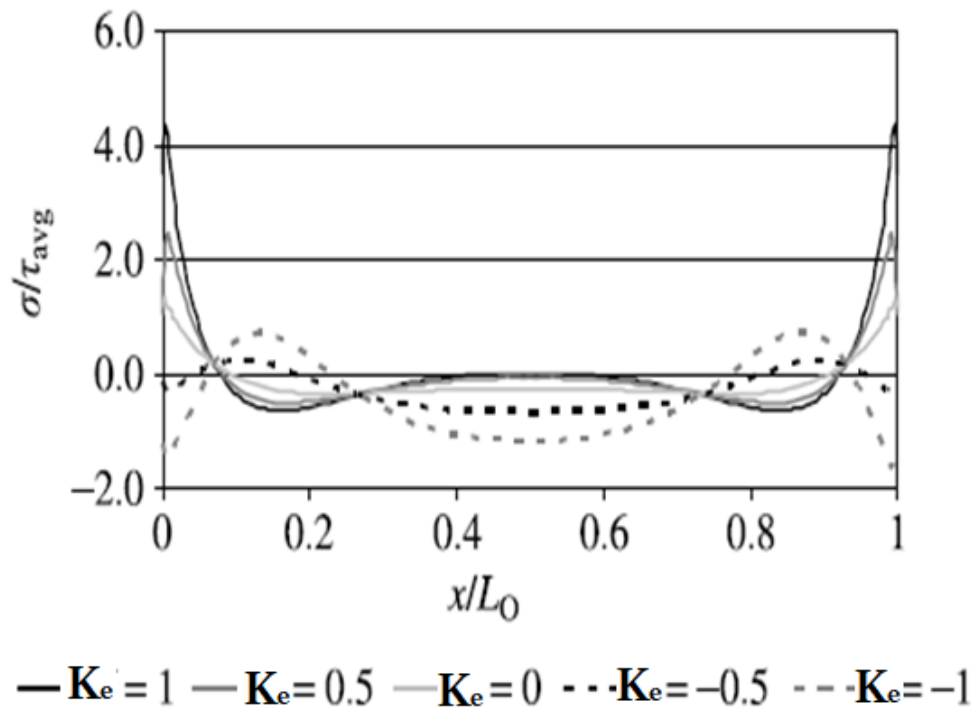


**Figure 2.32:** Stress distributions of the mid-thickness of the adhesive layer for different values of  $K$  [18].

Furthermore, Kishore and Prasad [95] conducted an experimental comparison between bonded flat-joggle-flat (FJF) and single lap joints for composite laminates. The study found that the FJF bonded joint increased its strength by 90% due to the elimination of its eccentricity.

Taib et al. [27, 28] conducted numerical analyses of two adhesive joint configurations, namely single lap and joggle lap joints. The composite adherend was assumed to behave as a linear-elastic material, whereas the layers of the adhesive were assumed to be non-linear. The study observed that:

- 1- Axial stress decreased with an increase in the curvature length, while the effect of curvature length on peeling and shear stresses was negligible.
- 2- The peel and shear stress were significantly reduced, and the load transfer was improved as the thickness of the spew fillet increased (Figure 2.33).

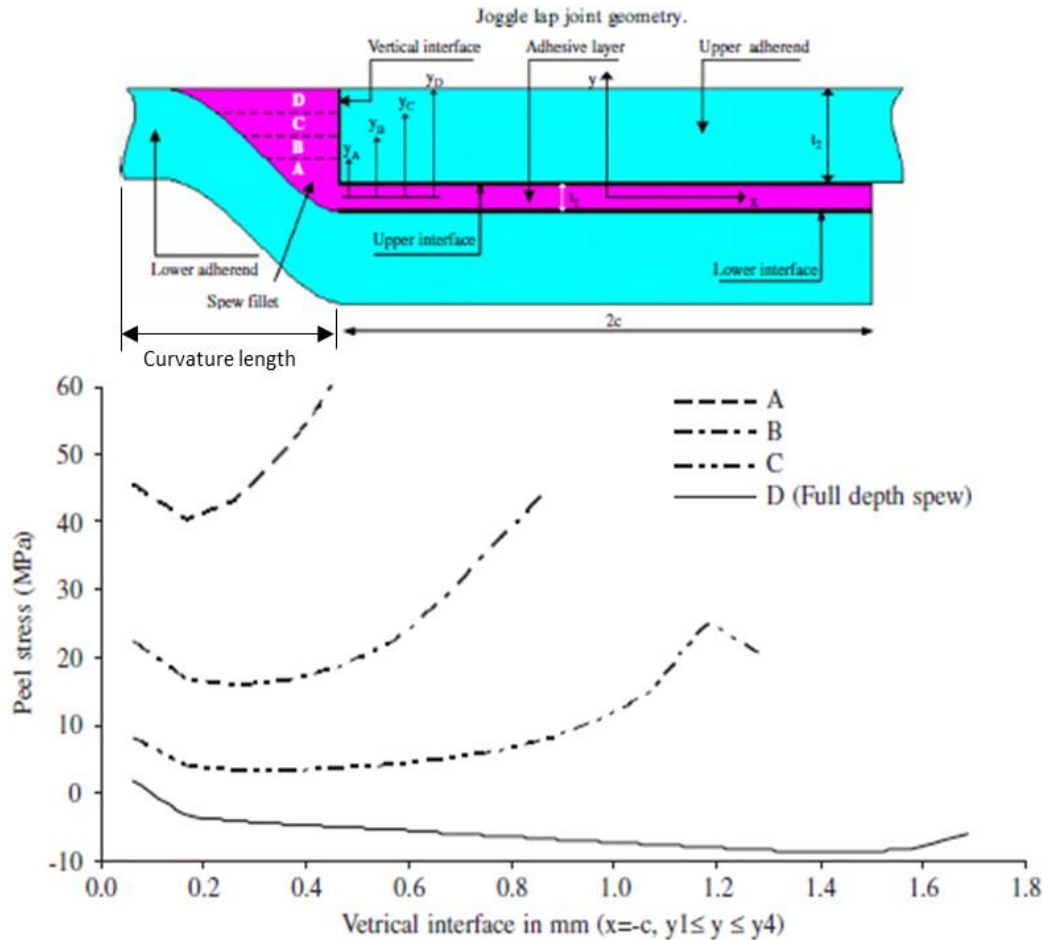


**Figure 2.33:** The peeling stress along different level of the adhesive thickness of the spew fillet [27].

Neto et al. [96] introduced a new design of the SLJ using reinforcement (Figure 2.34) to relieve peel stress in the adhesive layer, which is the primary threat to the adhesive joints. The new model was numerically analyzed in *ABAQUS* to assess the spew fillet effect. It was observed that the peel stress decreased as the spew fillet radius and attached additional composite increased (Figure 2.35). Moreover, an increase in the radius of the spew fillet reduced the rotation angle of the joint.

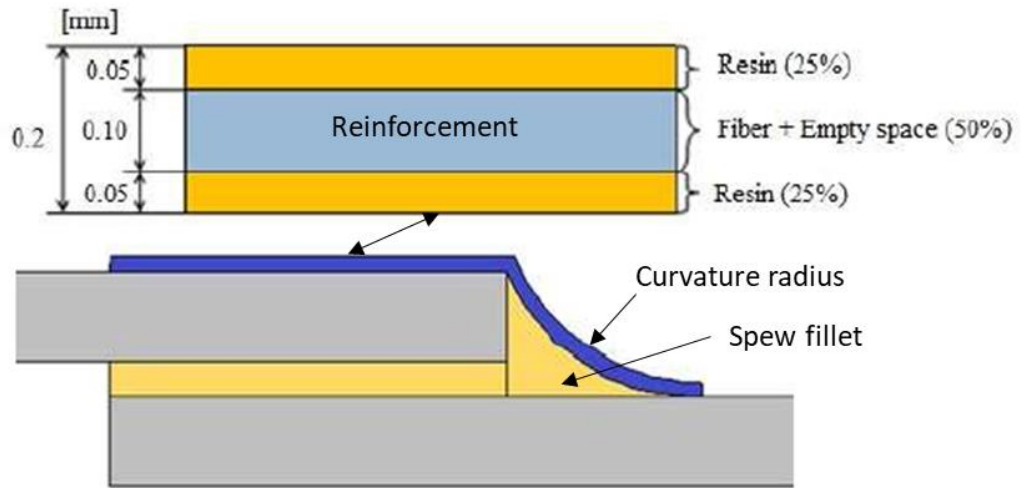


**Figure 2.34:** Location and shape of reinforcement [96].

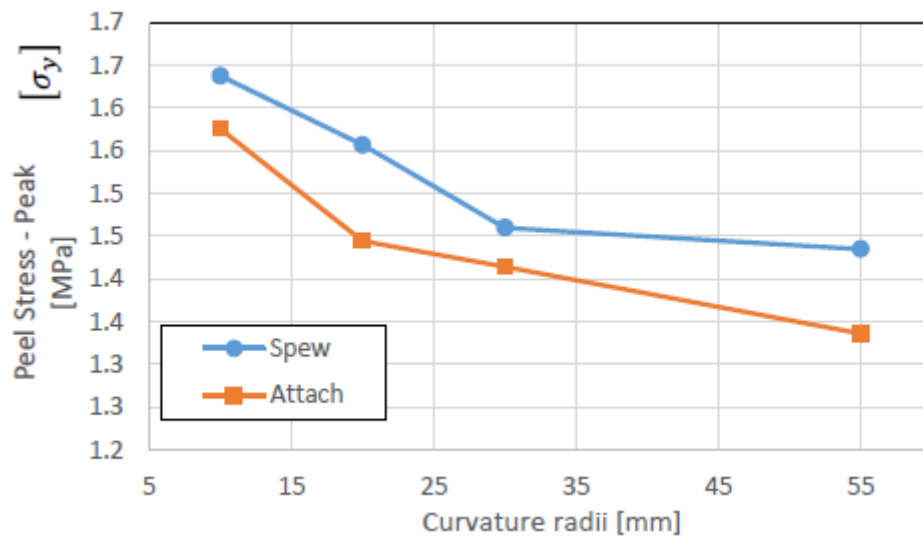


**Figure 2.35:** Effect of spew fillet and attached reinforcement on peel stress [96].

Çalık and Yıldırım [31] investigated the combined effect of the spew fillet, the bi-adhesive and the parallel slot in adherends on the stress distribution along the length of the adhesive SLJ using the Finite Element Method under pure tension. The study was concluded that for all conditions, maximum peel stress values in Case 1(25-75-25 mm, ductile-brittle-ductile adhesive) are approximately 7% lower than Case 2 (35-55-35 mm) (Figure 2.36).

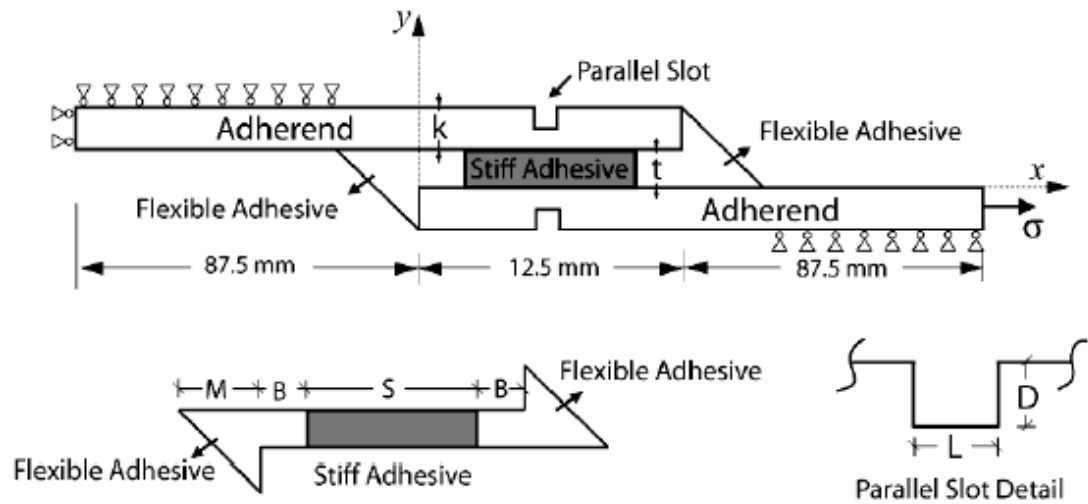


**Figure 2.36:** SLJ scheme with slots and bi-adhesive [97].

Wang et al. [97] experimentally and numerically investigated adhesive SLJs of different substrates and with different reinforcements (Figure 2.37), namely aluminum (A) and copper (C) alloys. The results showed that:

1. The deformation of the joints decreased with an increase in stiffness at the end of the overlap region.
2. Concerning failure of the adhesive joint, deformation of the substrate, and joint strength were affected by the mechanical properties of the adherends and reinforcement (Figure 2.38).

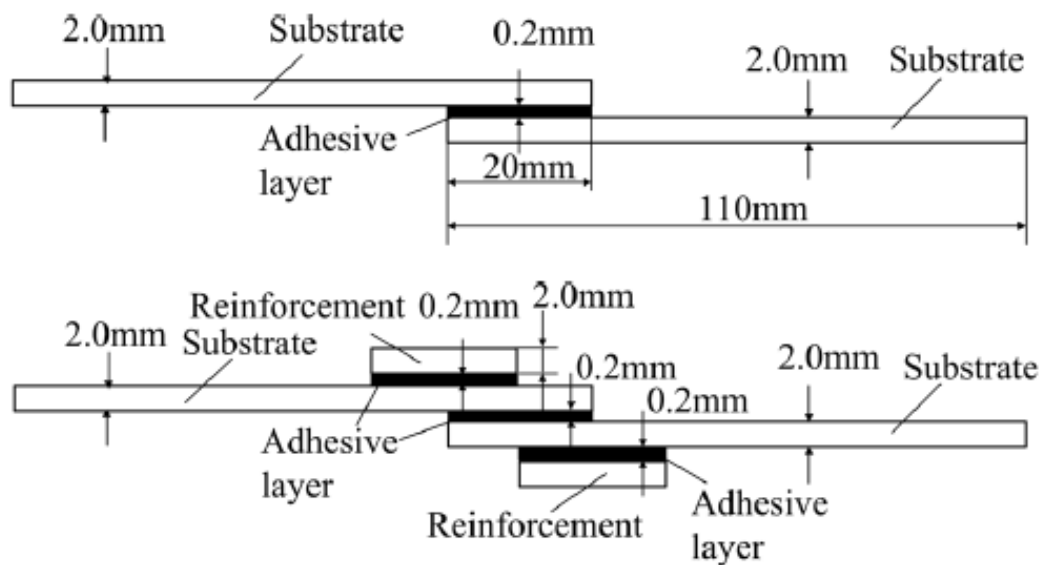


**Figure 2.37:** SLJ schemes of with and without reinforcements [97].

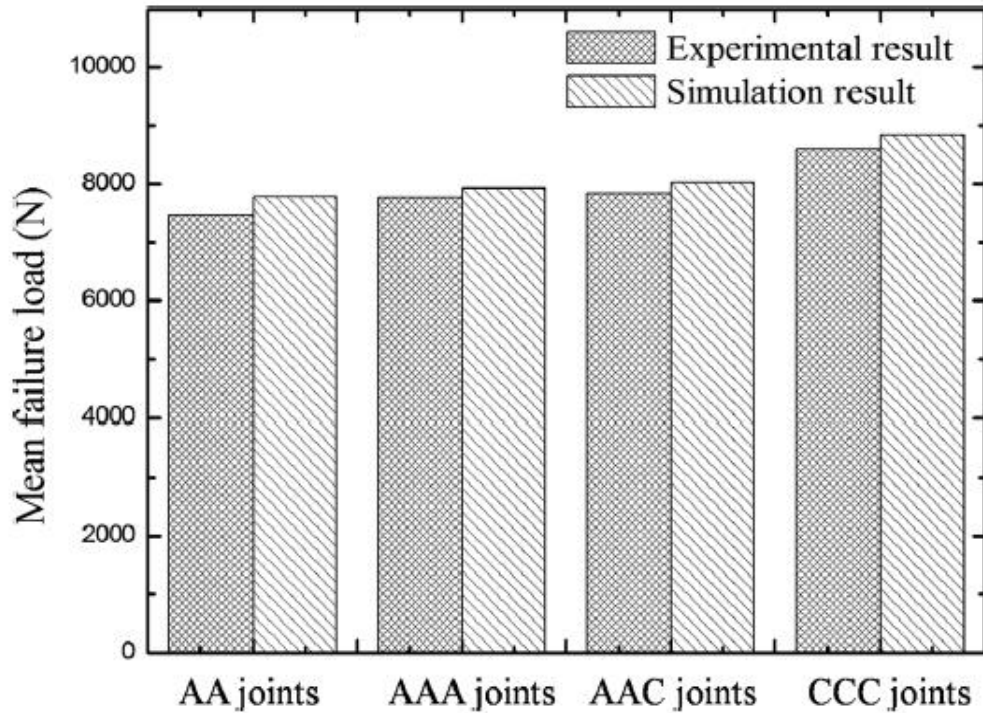


**Figure 2.38:** Effect of adherend and reinforcement strength on joint strength [97].

Ouellet and Vadean [98] compared the classical design of the HJ to a new design derived from analyzing the axiomatic design for quasi-isotropic composite materials. Their research showed that:

- 1- A new type of washers based on Belleville springs was proposed to force the washers to come into contact as close as possible with the overlapping edge (Figure 2.39).
- 2- Incorporating stiffer adhesives between the bolts to stiffen the area between them reduces the load transferred near the free edges of the joint (Figure 2.40).
- 3- Tapering the joint edge of the adherends reduces the local secondary bending moments (Figure 2.39).
- 4- The new design had significant strength by reducing the maximum peel stress in the adhesive layer (Figure 2.40).

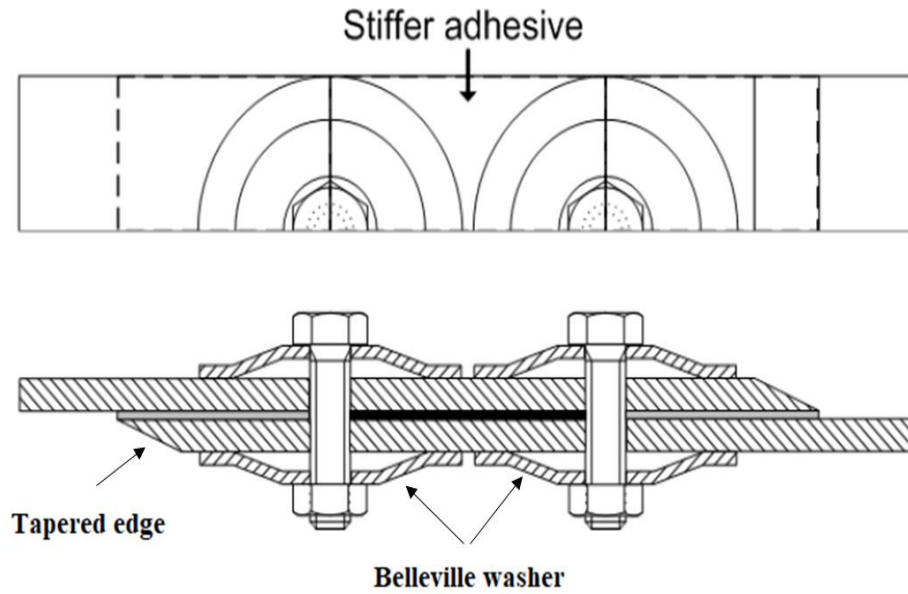


**Figure 2.39:** Configuration of the new design of the HJ [98].

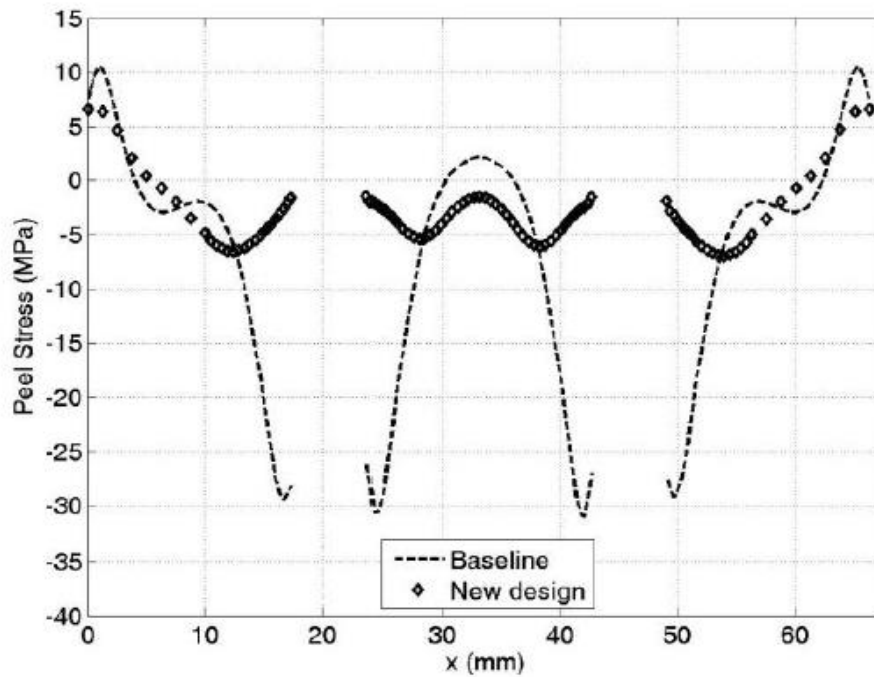


**Figure 2.40:** Peeling stress along the overlap length in the middle plane of the adhesive layer for new and baseline designs of the HJ [98].



## CHAPTER 3

### EXPERIMENTAL WORK AND MATERIALS

In this chapter, the details regarding the performed experiments, including the geometrical details, samples' preparation and the materials used in a row are described.

#### 3.1 Configurations of the Joints

In the experiments on the ADJ, BJ and HJ, three different adherend thicknesses, (2 mm, 4 mm and 6 mm) were considered for each overlap length (15 mm, 25 mm and 45 mm). The thickness of the adhesive layer was well-organized technically, and with precision so that the aluminum sheet (as a template) had the same thickness since the thickness was kept at a constant level of 0.200 mm in the ADJ and HJ. All the tests were performed three times at room temperature and at a relative humidity of 50% using a universal tensile test machine at a speed of 2 mm/min. The force-displacement curves presented in Chapter 5 present one of the three tests close to their mean value. The dimensions and boundary conditions for the parts that were used for the ADJ and the BJ structures are shown in Figure 3.1, where in the HJ combination of these two are used.

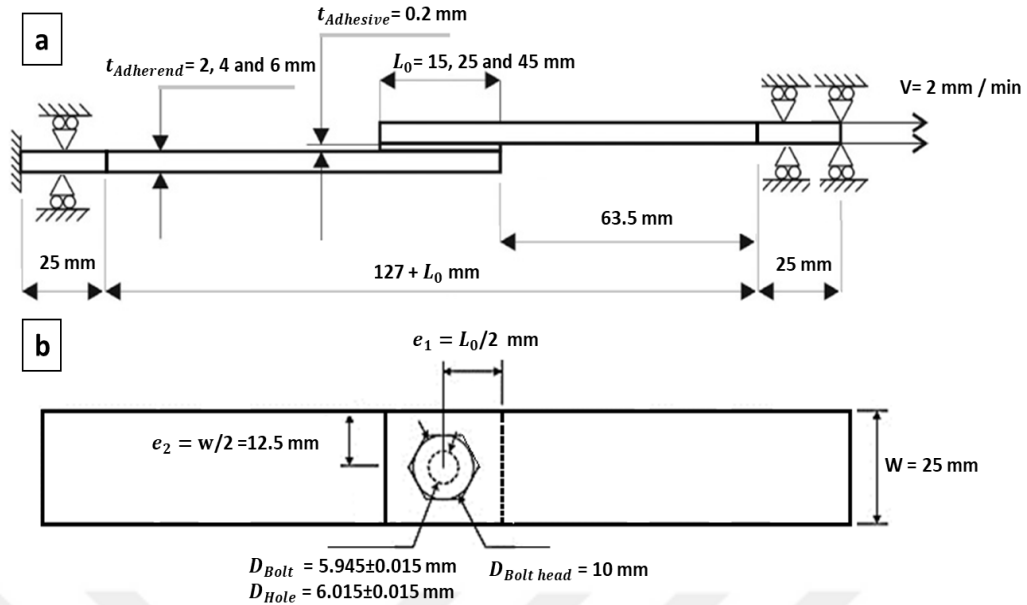


**Figure 3.1:** Geometry, boundary conditions and dimensions of adhesive (a) and bolted (b) joint configurations (side and top view, respectively).

### 3.2 Samples Preparation

In the ADJ and HJ, after all the adherends were carefully checked, the bonded area was abraded with 500 grit sandpaper to ensure interfacial adhesion. Afterwards, they were cleaned with dichloromethane (Methylene chloride  $\text{CH}_2\text{Cl}_2$ ) (Figure 3.2) and they were then allowed to dry. The adhesive film was precisely cut to the same dimensions as the overlap area (Figure 3.3). A specially designed jig (Figure 3.4) was used to guarantee the well-adjusted position of the ADJ, as described ASTM D1002-10. Before placing the samples in the jig, the set was sprayed with a release agent and thin pieces of oven paper were placed under the specimens to prevent the samples from adhering to the frame. We used a thermocouple to measure the temperature of the specimens instead of the oven thermometer, aimed at an accurate curing temperature of  $125^\circ\text{C}$  as the supplier recommends (Figure 3.5) [99]. The samples were cured for 60 minutes at a temperature of  $125^\circ\text{C}$  and a pressure of around 2 bars (applied as weight, see Figure 3.5) as the supplier recommends and in exact accordance with the cure conditions of the adhesive layer of the ADJ and HJ [99].

Finally, a drilling machine with laser alignment was used to obtain an accurate hole with a diameter of 6 mm (Figure 3.6). In the BJ and the HJ, the steel bolts were completely threaded and no washer was used (see Figure 3.7). A free-running fit with

## Chapter 3

ISO symbol 6H9/d9 was used, where  $D_{\min} = 6.000$  mm and  $D_{\max} = 6.03$  mm for the hole and  $d_{\min} = 5.93$  mm and  $d_{\max} = 5.96$  mm for the bolt. In the BJ and HJ experiments, the torque was applied to the joint with a value of 1 N.m as preloading using a torque wrench which has a measuring device therein to determine the value of the torque applied. The tensile tests of each joint configuration were performed, and the respective force-displacement curves were plotted using similar instrumentation as explained in Section 3.3, except for the fact that the displacement values were obtained from the machine rather than the extensometer. A group of prepared samples is illustrated in Figure 3.7. The vertical position of the specimen was adapted using a rotary laser level, as shown in Figure 3.8.



**Figure 3.2:** Preparation of adherents.



**Figure 3.3:** AF163-2K adhesive film.



**Figure 3.4:** Alignment set (jig).

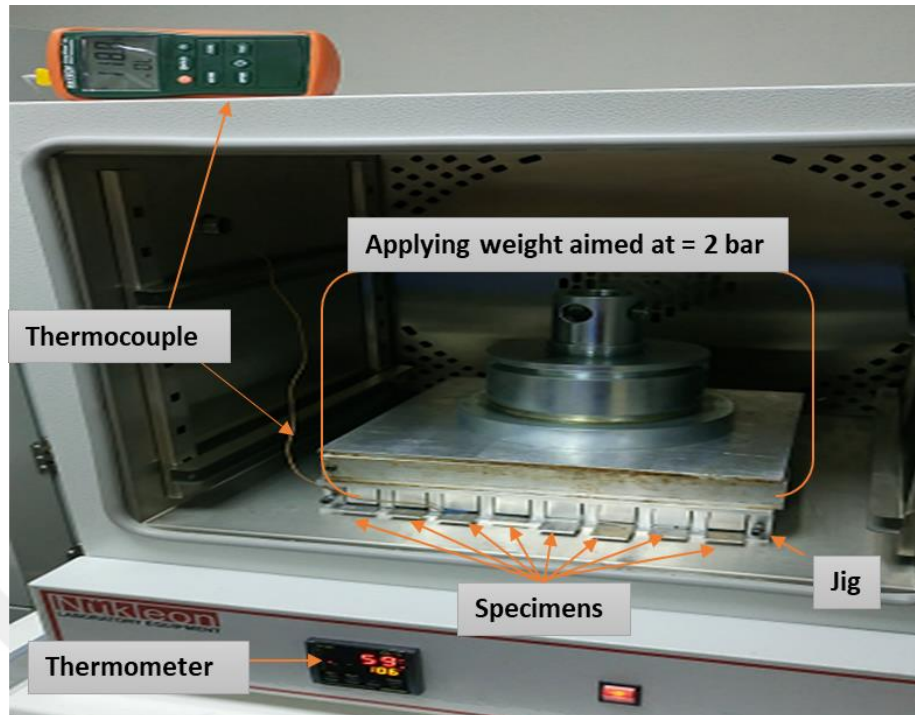
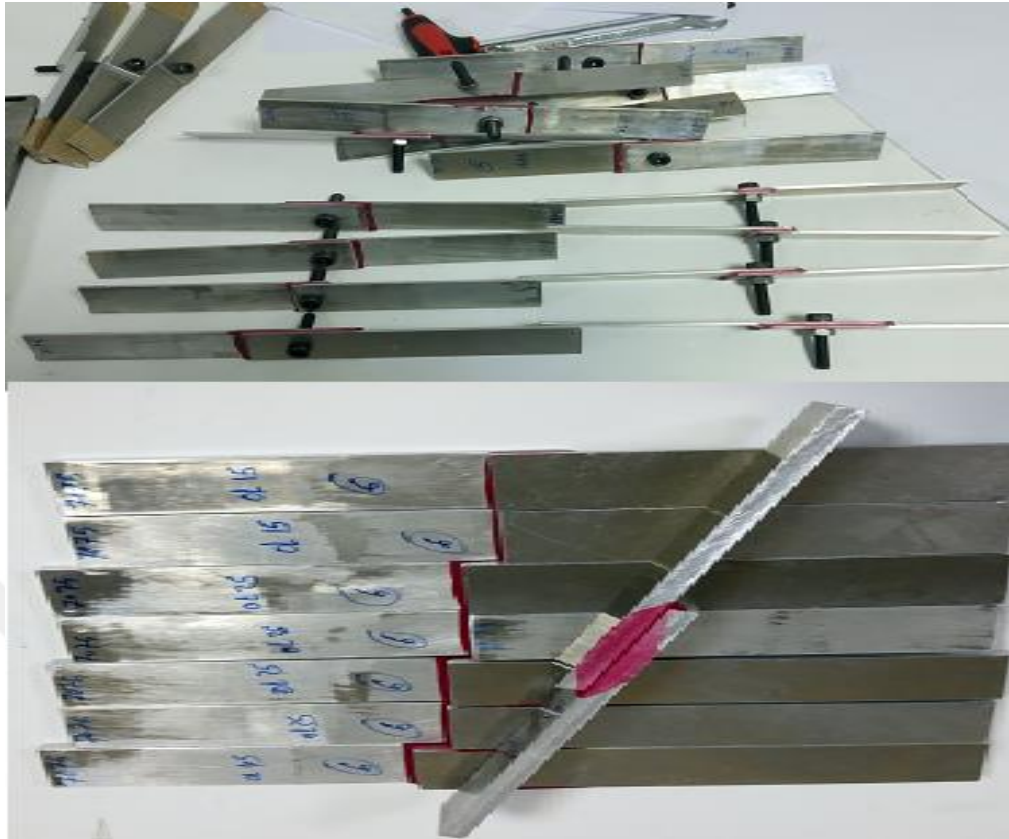


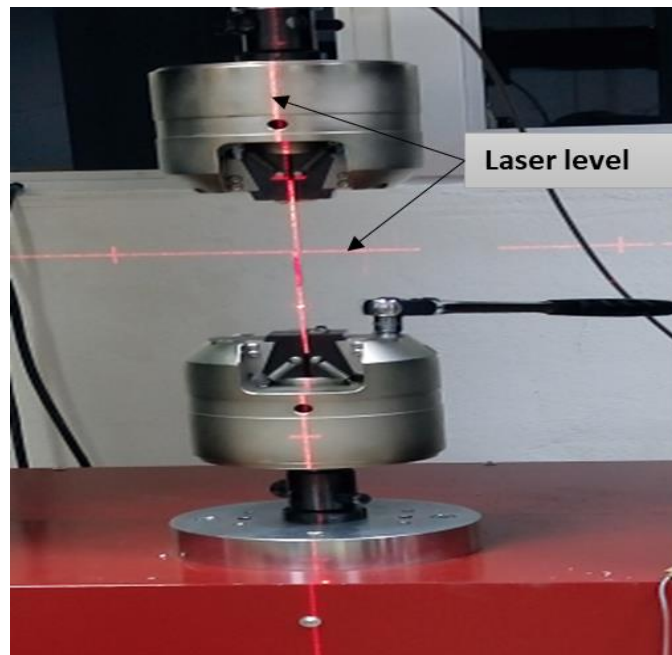
Figure 3.5: Jig inside the oven where the samples were cured.



Figure 3.6: Drilling machine with laser alignment.



**Figure 3.7:** A group of specimens after preparing.



**Figure 3.8:** Setting up the single lap joints with the rotary laser level.

### 3.3 Materials

Tensile tests were performed with the Besmak BMT-S 600 kN universal test machine to characterize the elastic, plastic and failure response of the adherend materials, AL6061 and AL7075, and the adhesive film (AF163-2K), a knit film made of thermosetting modified epoxy produced by 3M Scotch-Weld™ [99], which were used in this study and shown in Figures 3.9 and 3.10, respectively. They illustrate the curves closer to the average of three samples tested for each material. The bulk adhesive formed by putting twenty adhesive film layers on top of each other (Figure 3.12a) was cured in the same manner as the samples in Section 3.2. Then, the bulk adhesive was cut into tensile test specimens and tested. Four specimens of each material were tested. The axial extensometer mounted on the test section of the specimen was used to make accurate measurements of the strain in the specimen. In addition, a shear test was performed to determine the shear modulus (Figure 3.11) using thick adherend specimens (Figure 3.12b), aimed at only the shear force acting on the adhesive layer. The geometry of the tensile test specimen for the aluminum is illustrated in Figure 3.12c according to ASTM B557M-15. Completely threaded steel bolts (M6-Grade 8.8) were used in bolted and hybrid joints.

For the studied AF163-2K, the material parameters presented in Table 3.1 [100] were used. The obtained elastic properties with their standard deviations and plastic properties of all materials used are shown in Tables 3.2 and 3.3, respectively. The plastic response of the adherend materials in the simulations were characterized as shown in Figure 3.13.

**Table 3.1:** Material parameters of adhesive layer in numerical analysis.

$E$ (MPa)	$G$ (MPa)	$\sigma_n^0$ (MPa)	$\sigma_s^0 = \sigma_t^0$ (MPa)	$G_{c,n}$ (kJ/m <sup>2</sup> )	$G_{c,s} = G_{c,t}$ (kJ/m <sup>2</sup> )
2000	750	30	50	0.60	0.67

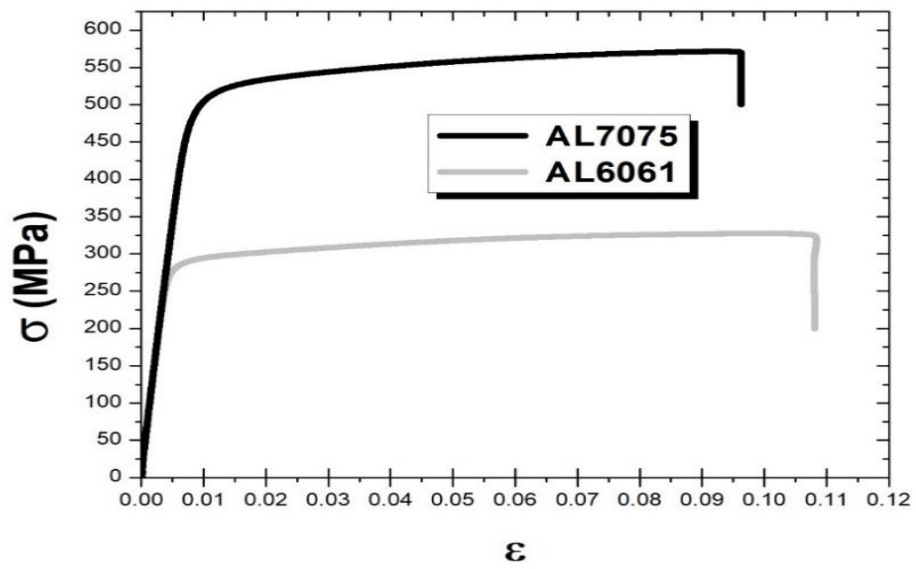


Figure 3.9: Tensile stress-strain curves for the AL6061 and AL7075 adherends.

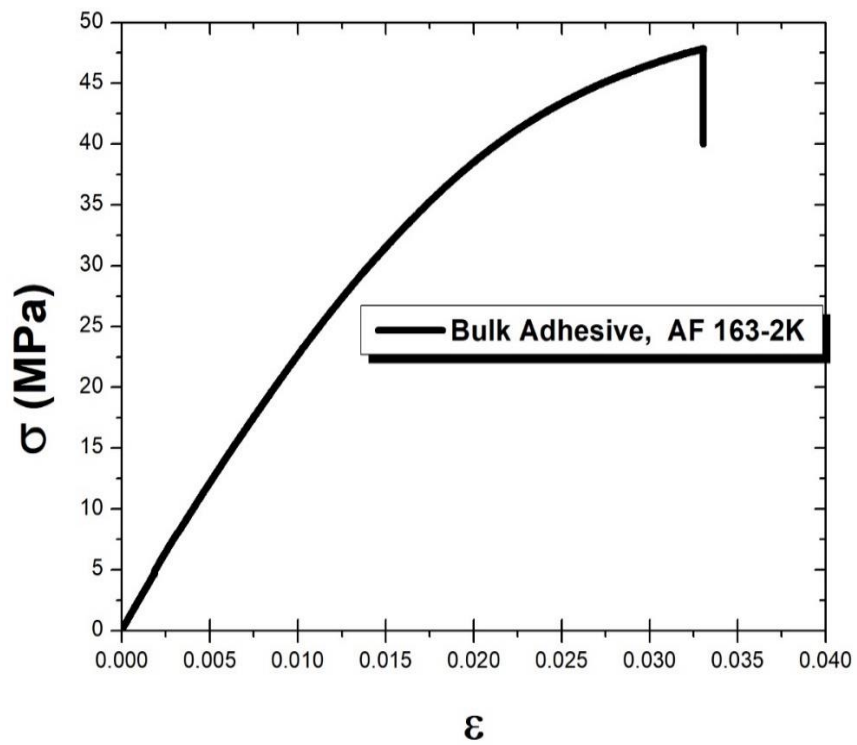
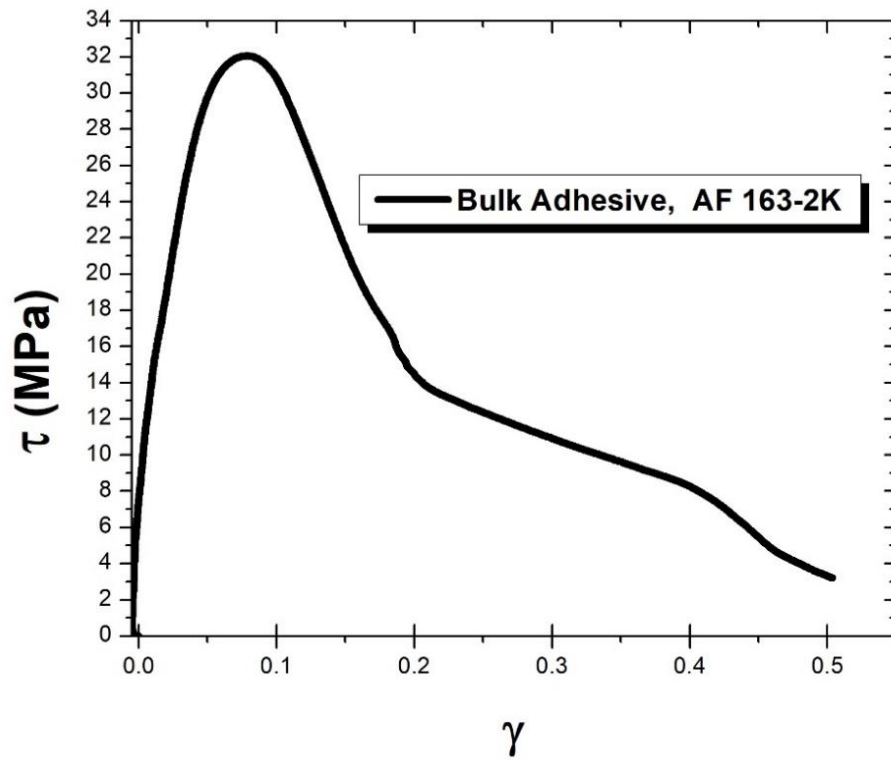


Figure 3.10: Tensile stress-strain curve for the adhesive film (AF163-2K).





**Figure 3.11:** Shear stress-strain curve for the adhesive film (AF163-2K).

**Table 3.2:** Elastic properties of materials.

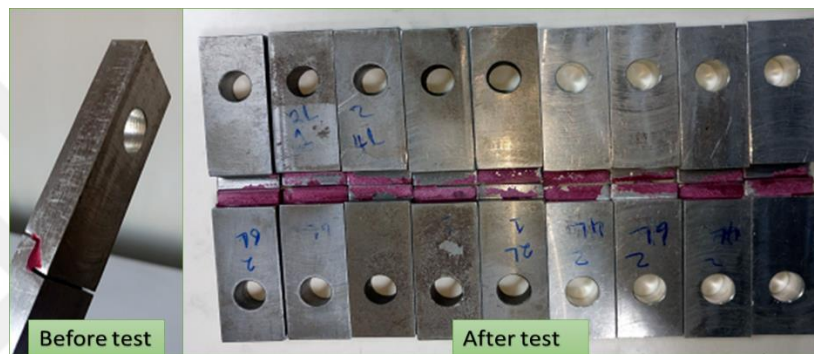
Materials	$E$ (GPa)	$\nu$	$\sigma_y$ (MPa)	$\sigma_u$ (MPa)	$\epsilon_f$ (%)
AL6061	68.9±0.85	0.33*	282±0.67	327±0.56	10.8±0.58
AL7075	71.7±0.78	0.33*	491±0.92	571±0.43	9.8±0.79
Steel bolt	210*	0.3*	600*	800*	8*

\*taken from [101] – the remainder are from the tensile test (average of three samples).

(a)



(b)



(c)

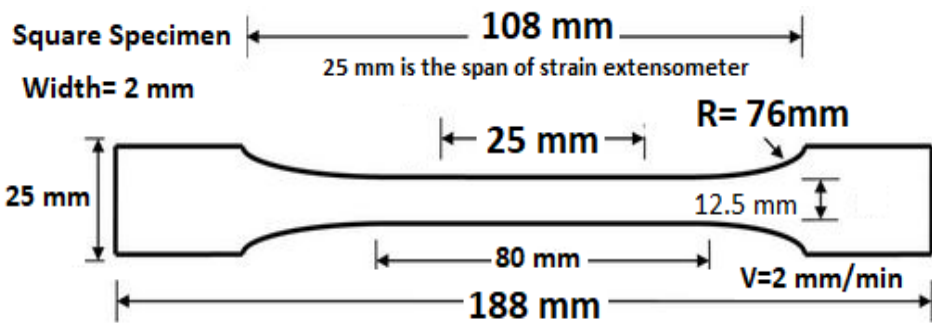
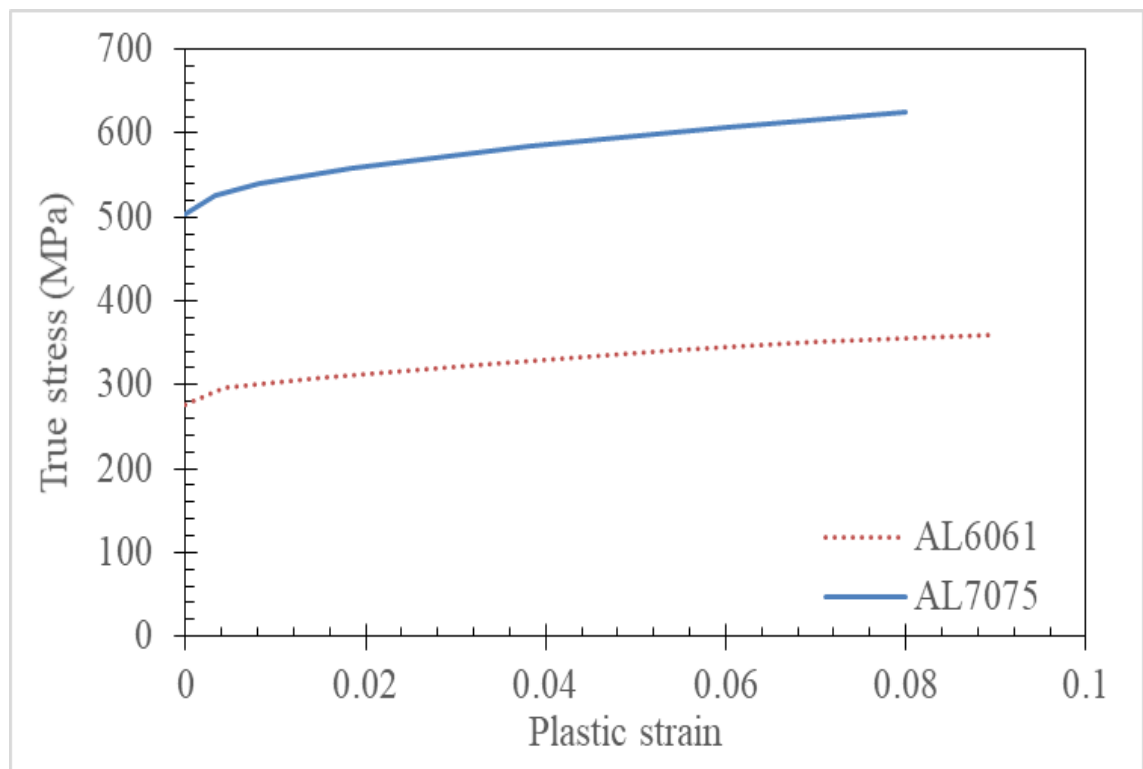


Figure 3.12: Bulk adhesive (a), thick adherend specimens (b) and tensile test specimen (c).

**Table 3.3:** Plastic properties of Materials extract from the true stress-strain curve.

Al6061		Al7075		Steel bolt [102]	
$\sigma_p$ (MPa)	$\epsilon_p$	$\sigma_p$ (MPa)	$\epsilon_p$	$\sigma_p$ (MPa)	$\epsilon_p$
276	0	503	0	640	0
295.9	0.0043	526	0.00332	700	0.0224
309	0.01534	540.3	0.00824	735	0.0337
325.6	0.034	557.8	0.01844	770	0.045
341.1	0.0542	584	0.0382	800	0.06
350.7	0.07	607.4	0.06	825	0.07
359.7	0.0896	624.7	0.08	850	0.08

**Figure 3.13:** Stress-strain relationship used in the simulations for the adherend materials.

## CHAPTER 4

### NUMERICAL MODELLING

This chapter introduces the Finite-Element Method (FEM). At this point, the FEM and its aspects in conjunction with constituent equations are first presented. Secondly, an incremental formulation of the cohesive zone, ductile and shear damage models are presented in a more detailed form for all implementations of the *ABAQUS* software.

#### 4.1 Finite Element Method (FEM)

Mechanics can be defined as the actual application of science to the design, construction or operation of a material system or devices, such as a machine, vehicle, or structure. Mechanics are categorized as follows:

1. Theoretical
2. Applied
3. Computational
4. Experimental

Theoretical mechanics works and operates with the basic laws and principles studied for intrinsic scientific value. Applied Mechanics conveys theoretical knowledge in the field of science and engineering applications specifically in connection with building mathematical models of physical phenomena. Computational

## Chapter 4

Mechanics creates solutions for specific problems through model-based simulation and through numerical methods implemented in digital computers. Experimental dynamics subordinate knowledge is obtained and achieved from theory, application and simulation to the fundamental test of supervision [103].

Continuum mechanics studies the body in a macroscopic dimension by using a continuum model in which a microstructure is homogenized by phenomenological means. Traditional applications are referred to as strong, changeable and adaptable mechanics. Structural Mechanics is known to be the combined point of solid mechanics. Because a structure is made solid for obvious reasons, Computational Solid Mechanics accentuates and affirms the application of scientific approaches, whereas Computational Structural Mechanics affirms the technical applications of structural design and analysis [103].

Continuum mechanics problems can be sub-grouped according to their being static or dynamic. In statistics, inertial forces are overlooked or undervalued. Static problems can be subdivided into time-invariant and quasi-static. Previously, it was not necessary to consider this explicitly. It is realized that it will need response sequence parameters such as historical time. Quasi-static problems include foundation settlement, creep flow, velocity dependent firing or fatigue cycling which requires more realistic time estimates, but inertia is overlooked because of slow motion. Time dependence in mechanics must take into account the actual time derived for the calculation of the inertia (and/or damping) force. Linear static analysis handles static problems where the response is linear in the causal sense. For example, doubling the applied force doubles the displacement and internal stress. Problems outside this domain are categorized as nonlinear [103].

The concluding categorization of Computational Solid and Structural Mechanics (CSSM) is based on a discretization method in which the continuous mathematical model is discretized in space, i.e., transformed into a discrete model of finite degrees of freedom, as listed below:

1. Finite-Element Method (FEM)
2. Boundary Element Method (BEM)

3. Finite Difference Method (FDM)
4. Finite Volume Method (FVM)
5. Spectral Method
6. Mesh Free Method

For linear problems, the finite-element method dominates the current scene, and the boundary element method publishes a powerful second choice in the chosen applications. For nonlinear problems, the dominance of the Finite-Element Method is deemed extraordinary [103].

FEM is a common numerical system for solving complex engineering problems where the application of general analytical methods may be limited or impractical. The general premise of this method is to discretize arbitrary domains into a set of simple shaped elements that approximate differential equations (Figure 4.1). Assuming a convenient approximate solution in each element, it derives the overall equilibrium condition of the structure. Satisfaction of these conditions leads to approximations to unknowns, such as displacement, deformation and stress [103].

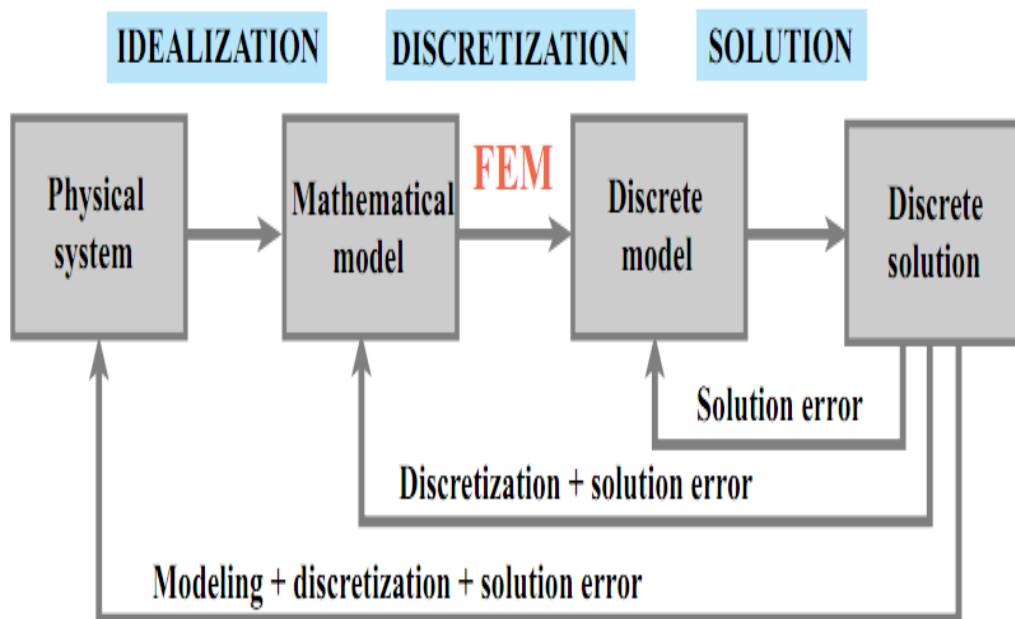


**Figure 4.1:** Stages of the physical simulation procedure [103].

### 4.1.1 Time Integration Methods (Explicit)

In order to find the unknown variables in the numerical analysis, such as displacement, stress and strain, one would need to integrate the rate equations in relation to time. Constructive velocity equations are highly nonlinear, so integration is usually gradually accomplished. Stress and the other state of variables are updated at every increment. Computational algorithms for time integration are grouped into two general classes: explicit and implicit algorithms. In this thesis, nonlinear analysis was performed with a dynamic explicit solver since it does not have convergence issues, unlike the implicit static solver. Next, the explicit time integration scheme is explained.

Explicit code integrates the equations of motion explicitly through time by utilizing and applying the central difference method. At each increment, the initial kinematic conditions are applied to calculate the kinetic conditions for the following increment.

The acceleration of the nodal ( $\ddot{u}$ ) can be calculated at the beginning of the time increment ( $t$ ) based on the dynamic equilibrium via the following equation:

$$\ddot{u}|_{(t)} = (M)^{-1} (P - I)_{(t)}$$

where  $M$  is the bulk mass matrix,  $P$  the vector of the externally applied force and  $I$  the vector of internal element forces. Hence, the configuration of the master mass matrix  $M$  is generally similar to the master stiffness matrix  $K$  in general. The mass matrix for the individual element is formed into the local coordinates, converted to the global, and merged into the master mass matrix using the same techniques utilized for  $K$ . The  $K$  and  $M$  assemblers can be made similarly. This process through a common uniformity is one of the great assets of the Direct Stiffness Method.

A notable difference from stiffness matrices is that one can utilize and apply diagonal mass matrices as a result of direct lumping. A main diagonal mass matrix can simply be stored as a vector. If and only if, all the entries are not negative, the inverse of the diagonal matrix is also diagonal, so it is easily reversed. A lumping matrix involves significant computational benefits for the calculations involving  $M^{-1}$ .

One of the approaches of mass matrix constructions is technically based on a variational formulation. This is, however, done by recognizing and obtaining the kinetic energy as a part of the governing equations. The kinetic energy of an element of mass density  $\rho$  takes up the domain of  $\Omega^e$  and moves around with the velocity field of  $\vec{V}^e$ , which is

$$T^e = \frac{1}{2} \int_{\Omega^e}^0 \rho (\vec{V}^e)^T \vec{V}^e d\Omega^e$$

The velocity field of elements is interpolated by the shape functions, which is

$$\vec{V}^e = N_v^e \dot{u}^e$$

where  $\dot{u}^e$  is recognized as the node degree of freedom (DOF) velocity and  $N_v^e$  is the shape function matrix. They are inserted into the previous equation and move the node velocities completely out of the integral, which gives:

$$T^e = \frac{1}{2} (\dot{u}^e)^T \int_{\Omega^e}^0 \rho (N_v^e)^T N_v^e \dot{u}^e d\Omega^e \stackrel{\text{def}}{=} \frac{1}{2} (\dot{u}^e)^T M^e \dot{u}^e$$

from which the element mass matrix follows as the Hessian of  $T^e$ :

$$M^e = \frac{d^2 T^e}{d\dot{u}^e d\dot{u}^e} = \int_{\Omega^e}^0 \rho (N_v^e)^T N_v^e d\Omega^e$$

Simultaneously, the acceleration equation at any identified or given nodal point is predicted and recognized only through its mass and through the net acting force. From the basic equations of the accelerations, the velocities ( $\dot{u}$ ) and displacements ( $\mathbf{u}$ ) are developed “explicitly” through the time increment of each one of them ( $\Delta t$ ) by utilizing the rule and code of the central difference via these enlisted equations below:



$$\dot{u}|_{(i+0.5)} = \dot{u}|_{(i-0.5)} + \left( \frac{\Delta t|_{(i+1)} + \Delta t|_{(i)}}{2} \right) \cdot \ddot{u}|_{(i)}$$

$$\dot{u}|_{(i+1)} = \dot{u}|_{(i+0.5)} + \left( \frac{\Delta t|_{(i+1)}}{2} \right) \cdot \ddot{u}|_{(i+1)}$$

$$u|_{(i+1)} = u|_{(i)} + \Delta t|_{(i+1)} \cdot \dot{u}|_{(i+0.5)}$$

In the case of element calculations, the element strain increments  $d\varepsilon$  is estimated and calculated from the strain rate  $\dot{\varepsilon}$ . The stresses are then computed from this equation:

$$\sigma_{(t+\Delta t)} = f(\sigma_{(t)} + d\varepsilon)$$

Then the nodal internal forces  $I_{(t+\Delta t)}$  are calculatedly assembled.

In the case of obtaining accurate results, the time increment  $\Delta t$  ought to be quite small so that it allows the accelerations to be nearly constant during an increment. By way of the time increment, however, it decreases the analysis demands to an unacceptable number of increments and computational time with the purpose of decreasing the computational time, either through the “loading rate scaling” or through the “mass scaling” which may be introduced. Both techniques, however, show a relevant and important scale of reduction through the process of time within the acceptance and calculation of the accuracy.

Explicit procedures incorporate time through the use of many small increments. The central difference operator is conditionally unmovable and the stability limit of an operator without damping is given in terms of the highest eigenvalue in the system as follows:

$$\Delta t \leq \frac{2}{\omega_{max}}$$

In *ABAQUS/Explicit*, the small quantity of damping is recognized to have the capacity to control the high frequencies of oscillations. By damping, the stable time increment is estimated and calculated by:

$$\Delta t \leq \frac{2}{\omega_{max}} (\sqrt{1 + \xi^2} - \xi)$$

where  $\xi$  is the critical damping in the highest mode. Conversely, the usual engineering intuition introduces and presents damping to the solution that reduces the stability of the increase of time.

A trial of the stability of the increase in time is calculated for each element in the mesh by utilizing and applying the following equation:

$$\Delta t \leq \frac{2}{\omega_{max}^{element}}$$

where  $\omega_{max}^{element}$  is regarded as the element maximum eigenvalues. A conservative estimate of the stable time increment is, however, then given by the minimum taken with all the elements. The above limit, with its stability, is rewritten as follows:

$$\Delta t = \left( \frac{L_e}{C_d} \right)$$

where  $L_e$  is the dimension of characteristic element and  $C_d$  is recognized as the current and effective dilatational wave speed of the material. The dimension of characteristic element is then obtained from an analytic upper bound expression for the maximum eigenvalue of an element.

#### 4.2 Cohesive Zone Modelling (CZM)

CZM was once introduced and proposed by Barenblatt [104] according to the principles of Griffith's theory associated with brittle fracture, which was then applied in the computational framework of FEM by Hillerborg et al. [105]. Sugiman and Ahmad [57] asserted that the CZM methodology had a higher value compared to the

continuum damage methodological approach for adhesive modeling while envisaging the dimensions and degree of damage and also less in the computational time. A similar valuation was made by Rudawska [58], who distinctively compared the connections between experimental and numerical results. More researchers [48, 59, 60, 62, 63, 106-108], however, asserted and presented the same in their studies and research. Traction separation law controls the response of cohesive elements. The nominal traction stress vector,  $t$ , is comprised of and formed with three components,  $t_n$ ,  $t_s$ , and  $t_t$ , with three-dimensional problems, which represent the normal along the local 3-direction and the three shear tractions. The corresponding separations are, however, denoted by  $\delta_n$ ,  $\delta_s$ , and  $\delta_t$ . Hence, elastic behavior can then be quoted as

$$t = \begin{Bmatrix} t_n \\ t_s \\ t_t \end{Bmatrix} = \begin{bmatrix} K_{nn} & K_{ns} & K_{nt} \\ K_{ns} & K_{ss} & K_{st} \\ K_{nt} & K_{st} & K_{tt} \end{bmatrix} \begin{Bmatrix} \delta_n \\ \delta_s \\ \delta_t \end{Bmatrix} = K \delta$$

In order to limit the cohesive constraint, it acts along the contact normal direction only, which is defined as uncoupled cohesive behavior and is specified as the zero values for the shear stiffness components,  $K_{ss}$  and  $K_{tt}$ . Alternatively, if only the tangential cohesive constraints are to be emphasized, the normal stiffness term,  $K_{nn}$ , can then be set to the point of zero in most cases where the regular “separations” will then be unconstrained. Regular compressive forces are therefore resisted as per the usual contact behavior [109-112].

By using damage modeling, one can simulate the bond between two cohesive surfaces degrading and eventually failing. The failure mechanism consists of two components: damage initiation criterion and damage evolution law. The initial response is linear. However, if the initial criterion of damage is met, damage can occur according to user-defined damage evolutionary laws. Figure 4.2 illustrates a typical tow separation linear response with a failure mechanism. If a damage initiation criterion is specified without the corresponding damage evolution model, *ABAQUS* evaluates the damage initiation criteria for output purposes only. The response of the cohesive surface is not affected (i.e., no damage occurs). Cohesive surfaces are, however, not damaged under pure compression [109-112].

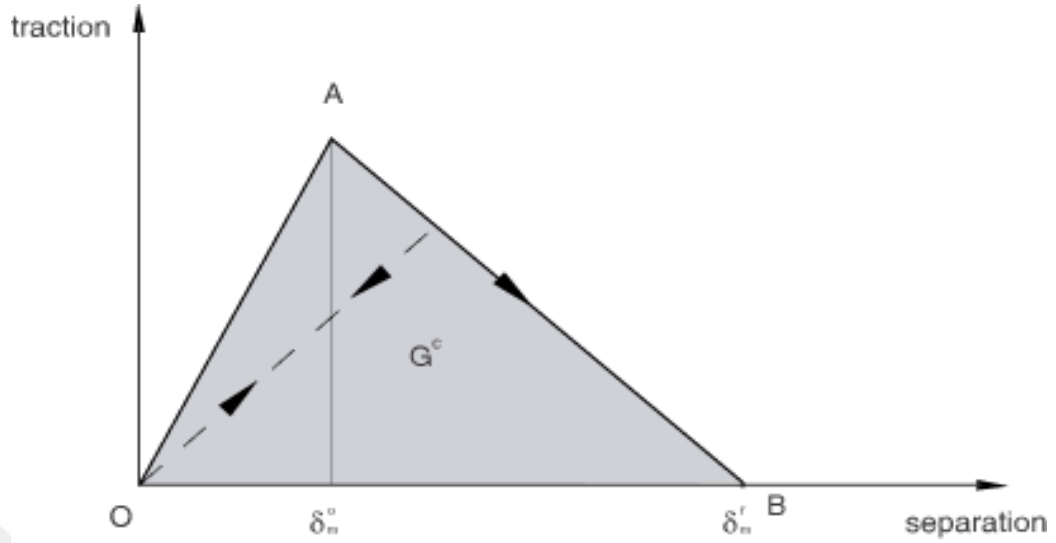


**Figure 4.2:** Linear damage evolution [110].

In this research, the study of damage is asserted and envisioned to initiate when a quadratic interaction function which involves the nominal stress ratios for different modes reaches a value of 1 [109-112]. This standard can be represented and shown as follows:

$$\left(\frac{\langle\sigma_n\rangle}{\sigma_n^0}\right)^2 + \left(\frac{\sigma_s}{\sigma_s^0}\right)^2 + \left(\frac{\sigma_t}{\sigma_t^0}\right)^2 = 1$$

where  $\langle a \rangle$  represents the Macaulay bracket, which is defined as  $(a + |a|)/2$ , and  $\sigma_n$ ,  $\sigma_s$  and  $\sigma_t$  represent the tractions in each pure mode: normal to the interface ( $n$ ), in the first ( $n$ ) and in the second shear direction ( $t$ ), respectively.  $\sigma_i^0$ ,  $i = n, s, t$  are the normal and shear strength values, respectively. After damage initiation, linear softening starts where the traction approaches zero at each mode of the critical displacement value ( $\delta_{c,i}$ ). As the fracture toughness for each mode ( $G_{c,i}$ ) characterizes the respective area under the traction-separation curve,  $\delta_{c,i} = 2G_{c,i}/\sigma_i^0$  can be easily found. The damage evolution is governed by the following quadratic equation:

$$\left(\frac{G_n}{G_{c,n}}\right)^2 + \left(\frac{G_s}{G_{c,s}}\right)^2 + \left(\frac{G_t}{G_{c,t}}\right)^2 = 1$$

where  $G_i$  is the work done by the pure mode traction  $\sigma_i$  on the corresponding separation  $\delta_i$ . For the studied AF163-2K, the material parameters ( $\sigma_n^0 = 30$  MPa,  $\sigma_s^0 = \sigma_t^0 = 50$  MPa and  $G_{c,n} = 0.60$  kJ/m<sup>2</sup>,  $G_{c,s} = G_{c,t} = 0.67$  kJ/m<sup>2</sup>) determined in [113] were used, where the parameters relevant to processes evolving in first and second shear modes were considered identical.

The damage evolution represented by  $D$  is therefore based on the effective displacement at complete failure,  $\delta_f$ , relative to the effective displacement at damage initiation,  $\delta_0$ , are as shown in Figure 4.2, as a tabular function of the mix-mode (Figure 4.3) and it is calculated through the following linear equation [109-112]:

$$D = \frac{\delta_f(\delta - \delta_0)}{\delta(\delta_f - \delta_0)}$$

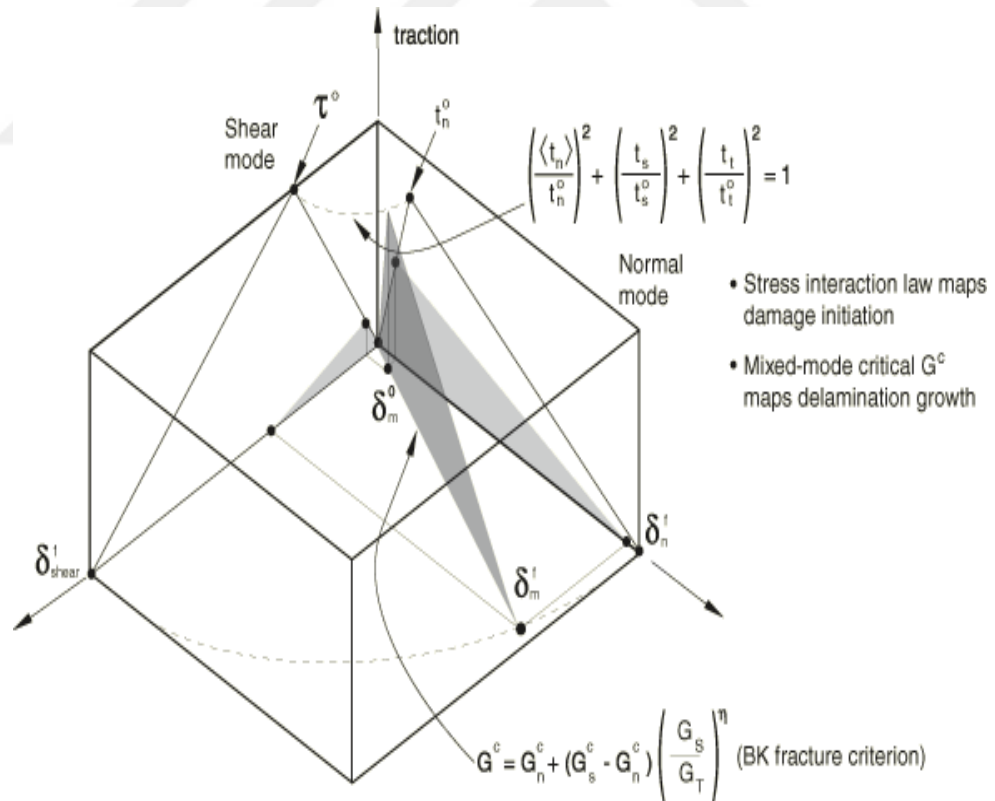


**Figure 4.3:** Illustration of mixed-mode response in cohesive elements [110].

### 4.3 Fracture of Ductile Metals

The fractures of ductile metals are caused by two major failure mechanisms:

1. Ductile fracture due to the nucleation, growth and coalescence of voids.
2. Shear fracture due to shear band localization.

In soft metals, necking occurs early due to extensive plastic deformation. After necking, voids or crack nucleation will form in the solid and it grows. Then coalescence of micro voids occurs and leads to separation. Figure 4.4 illustrates the elongation and shear-causing crack formation of stretched voids by connecting the voids [114].

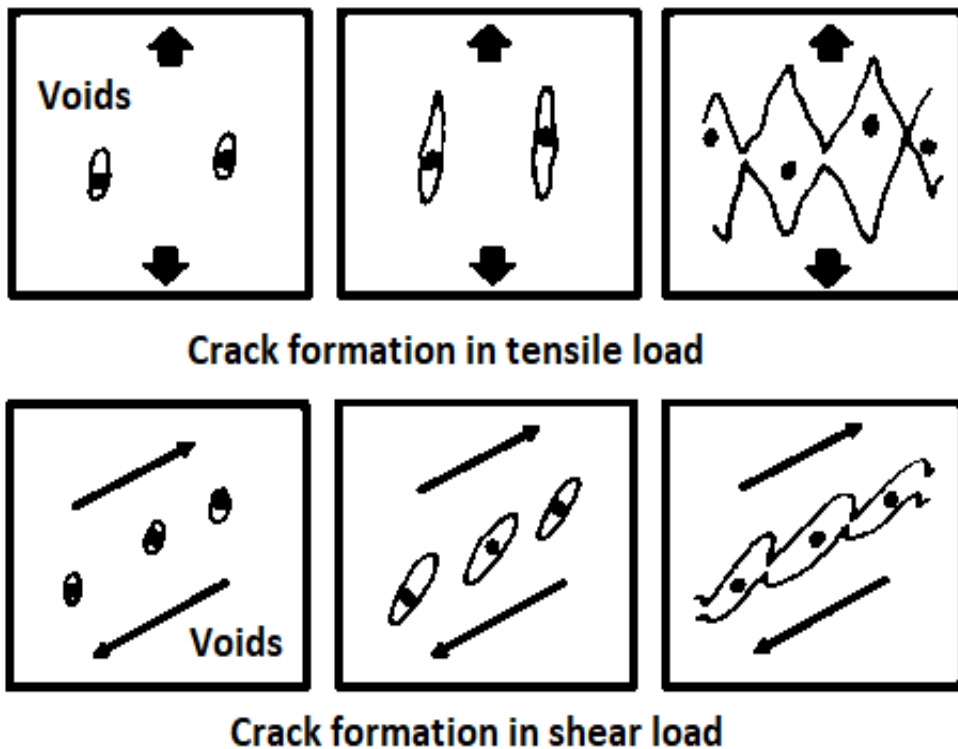


**Figure 4.4:** Formulation of the crack under tensile and shear loading [114].

### 4.3.1 Ductile Damage Criterion

The ductile criterion predicts the onset of damage as a result of nucleation, growth and coalescence of voids. The model asserts that the equivalent plastic strains at the onset of damage as

$$\bar{\varepsilon}_D^{pl}(\eta, \dot{\varepsilon}^{pl})$$

where  $\bar{\varepsilon}_D^{pl}$  is a function of stress triaxiality and strain rate.  $\eta = -p/q$  is the stress triaxiality where  $p$  is the pressure stress,  $q$  the von Mises equivalent stress and  $\dot{\varepsilon}^{pl}$  is the equivalent plastic strain rate [109-112].

The criterion for damage initiation is met when the following condition is satisfied [109-112]:

$$\omega_D = \int \frac{d \bar{\varepsilon}_D^{pl}}{\bar{\varepsilon}_D^{pl}(\eta, \dot{\varepsilon}^{pl})} = 1$$

where  $\omega_D$  is a state variable that increases monotonically with plastic deformation. At each increment, during the analysis, the incremental increase in  $\omega_D$  is computed as [109-112]

$$\Delta \omega_D = \frac{\Delta \bar{\varepsilon}_D^{pl}}{\bar{\varepsilon}_D^{pl}(\eta, \dot{\varepsilon}^{pl})} \geq 0$$

### 4.3.2 Shear damage criterion

The shear criterion envisions the onset of damage due to shear band localization. The model assumes that the equivalent plastic strain at the onset of damage is

$$\bar{\varepsilon}_S^{pl}(\theta_S, \dot{\varepsilon}^{pl})$$

Where  $\bar{\varepsilon}_S^{pl}$  is a function of the shear stress ratio and strain rate [109-112].

$[\theta_s = (q + k_s p)/\tau_{max}]$  is the shear stress ratio, where  $q$  is the von Mises equivalent stress,  $k_s$  the material parameter (a typical value of  $k_s = 0.3$  for aluminum) [115],  $p$  is the pressure stress and  $\tau_{max}$  is the maximum shear stress [109-112].

The criterion for damage initiation would occur when and once the following condition is occurred [109-112],

$$\omega_s = \int \frac{d\bar{\epsilon}^{pl}}{\bar{\epsilon}_s^{pl}(\theta_s, \dot{\bar{\epsilon}}^{pl})} = 1$$

where  $\omega_s$  is identified as a state variable that reaches a level that increases monotonically with plastic deformation proportional to the incremental change in equivalent plastic strain. At each increment during the analysis, the incremental increase in  $\omega_s$  is computed as [109-112],

$$\Delta\omega_s = \frac{\Delta\bar{\epsilon}^{pl}}{\bar{\epsilon}_s^{pl}(\theta_s, \dot{\bar{\epsilon}}^{pl})} \geq 0$$

### 4.3.3 Damage evolution

Directly under the background of the characteristic stress-strain characteristics of the damaged materials with isotropic hardening elastic-plastic material, the damage is created in two forms: yielding stress softening and elastic degeneration. The stress-strain curve reaction to the damage is shown in Figure 4.5, where  $E$  is Young's modulus,  $\sigma_{y0}$  and  $\bar{\epsilon}_0^{pl}$  are the yield stress and equivalent plastic strain at the onset of damage,  $\bar{\epsilon}_f^{pl}$  is the equivalent plastic strain at failure (when the  $D = 1$ ). The substances would lose their load carrying capacity once the  $D = 1$ . The element would be taken out from the mesh if all of the section points at any one integration position would lose their load-carrying capacity. The reactions from the real curve, without damage, are formed by a dashed curve. The damage evolution is demonstrated in two forms of softened yielding stress and degenerate elasticity  $((1-D) \cdot E)$ . The whole damage variable  $D$  seizes the unified effect of the entire active mechanisms and computes based on the individual damage variables for each one of the mechanisms [109-112].



$$\sigma = \frac{F}{A} \quad \& \quad \bar{\sigma} = \frac{F}{A-AD}$$

$$\bar{\sigma} = \frac{F}{A(1-\frac{A_D}{A})}, \text{ where } D = \frac{A_D}{A}$$

$$\sigma = (1 - D)\bar{\sigma}$$

where  $D$  is the long-range comprehensive damage variable,  $\sigma$  is then recognized as the true stress,  $\bar{\sigma}$  the effective or undamaged stress,  $A$  an authentic exterior and outward area and  $A_D$  the defected outward and exterior area.

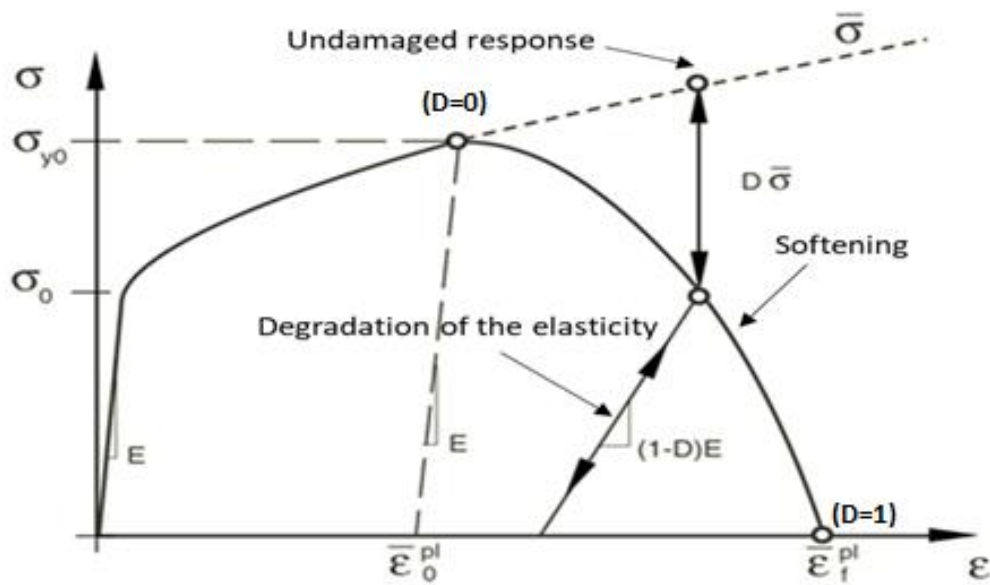


**Figure 4.5:** Stress-strain curve with progressive damage degradation [110].

It can, however, be observed that the damage initiation criterion begins at the point  $D = 0$ , and damage evolution builds from this point just before the element deletion that occurs at point  $D = 1$ , where the elements will then be taken away from the measurements once the stiffness is fully degraded.

Once the damage initiation criterion is achieved, the effective plastic displacement  $\bar{u}^{pl}$  is identified and recognized with the evolution equation,

$$\dot{\bar{u}}^{pl} = L_e \cdot \dot{\bar{\epsilon}}^{pl}$$

where,  $L_e$  is the characteristic length of the element and  $\bar{\epsilon}^{pl}$  is the effective plastic strain.

The evolution of the damage variable with the relative plastic displacement can be specified in tabular, linear or exponential forms. The linear and exponential forms of damage evolution with plastic displacement are

$$\dot{d} = \frac{L_e \cdot \dot{\bar{\epsilon}}^{pl}}{\bar{u}_f^{pl}} = \frac{\dot{\bar{u}}^{pl}}{\bar{u}_f^{pl}} \quad (\text{linear})$$

$$d = \frac{1 - e^{-\alpha(\bar{u}^{pl}/\bar{u}_f^{pl})}}{1 - e^{-\alpha}} \quad (\text{exponential})$$

where,  $\alpha$  is the exponential law parameter and  $\bar{u}_f^{pl}$  is the effective plastic displacement at failure. Here, the material stiffness is fully degraded ( $d=1$ ) when  $\bar{u}^{pl} = \bar{u}_f^{pl}$  [109-112]. In the energy type damage evolution, instead of giving the effective plastic displacement at failure as an input, it is computed as  $\bar{u}_f^{pl} = 2G_f/\sigma_{y0}$ , where  $G_f$  is the fracture energy per unit area and  $\sigma_{y0}$  is the value of the yield strength at the time when the failure criterion is reached.

#### 4.4 ABAQUS Software

*ABAQUS*<sup>®</sup> finite-element code was selected to perform all the simulations performed within the entire period of this study. *ABAQUS* is a universal code that has been technically successful in the implementation phase to solve numerous problems, challenges and difficulties in the structural analysis and other disciplines of mechanical engineering. In addition, *ABAQUS* creates space and opportunities for specific interactions between different engineering fields, such as thermoelectric and thermal structure coupling field problems. This section provides an overview of the code

operations. A great focus is placed on the relevant and identified qualities of the code in relation to the precisions that describe the structural experience and development that comprise the simulations that have been performed in this work [109-112].

*ABAQUS/Explicit* demands and needs much less disk space and memory than *ABAQUS/Standard* in the same simulation. The problem of comparing the computation costs of both programs is attractive because of the substantial disk space and memory savings of *ABAQUS/Explicit*. *ABAQUS/Explicit* is an obvious selection for the wave propagation analysis. However, there are static or semi-static problems that can be simulated with any program. With *ABAQUS/Standard*, there are generally mechanical engineering problems that can be solved, but these are difficult to perform due to contact or material complexity, resulting in many iterations. These analyses are highly demanding in *ABAQUS/Standard*. This is because we need a series of linear equations at every iteration. *ABAQUS/Standard* must be repeated to ascertain the answer to the nonlinear problem, but *ABAQUS/Explicit* determines the solution without repetition by explicitly advancing the kinetic state from the previous increment. If the same analysis with *ABAQUS/Standard* needs quite a large number of iterations, the analysis in *ABAQUS/Explicit* can be more efficient but require a large number of time increments [109-112].

In the quasi-static analysis, the work utilized by the external forces is almost identical to the internal energy of the system. In the case of viscoelastic materials, discrete dashes, or material damping that are not applied nor utilized, the viscous dissipation energy is technically and relatively small. Since the velocity of the material in the model is very small, inertial forces can be ignored in the quasi-static analysis. These situations indicate and reveal that the kinetic energy in the analysis must be very small. The kinetic energy of the deformation material ought not to exceed a small fraction of internal energy (typically 5% to 10%) in most processes [109-112].

The reduction of the integration utilizes a lower order of integration to form element stiffness. Reduced integration elements, specifically and particularly for 3D problems, can significantly reduce the run-time. A careful look at an example of the analysis with a C3D8 element which consists of 8 integration points in contrast to the one with C3D8R element, which consists of only one, reveals element assembly estimated to be 8 times more demanding and requiring much for the former

(Figure 4.6). The user has the opportunity to select from the full- integration and the decreased-integration only for quadrilateral and hexahedral elements. The first-order decreased integration elements, such as C3D8R, can demonstrate an hourglass. This implies that the elements have the ability to be distorted in such a manner that the computed strains at the single integration point are viewed as zero. This results in an uncontrolled mesh distortion. These elements, however, do have the potential capacity of hourglass control, but this is productive only with the presence of fine meshes[109-112].

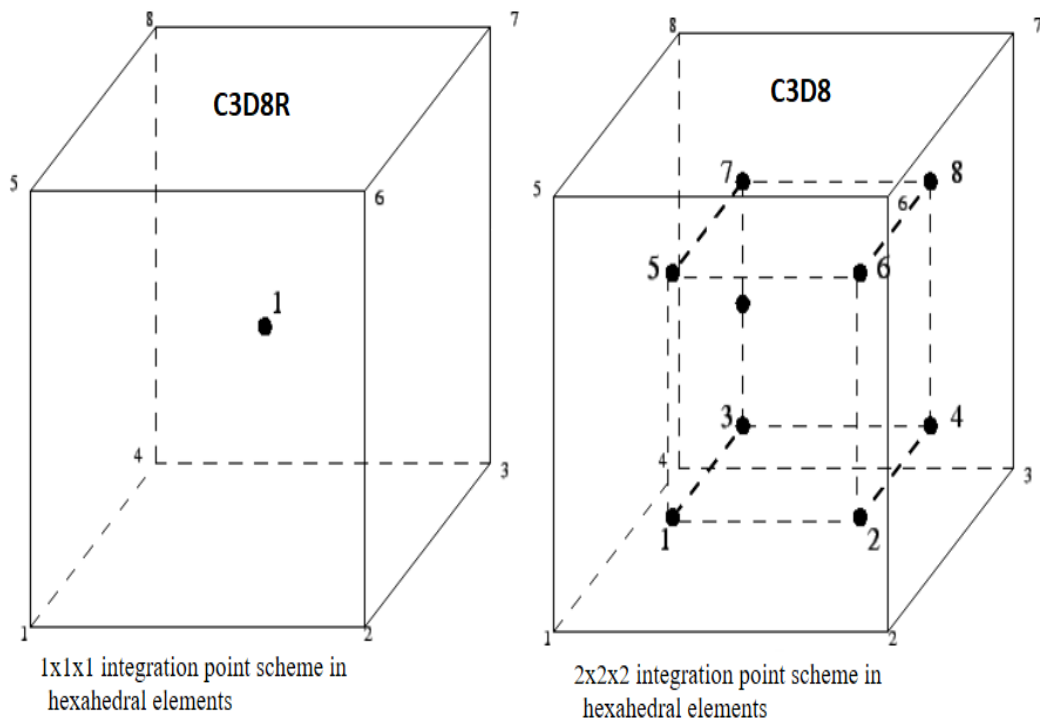


**Figure 4.6:** Integration points scheme in elements C3D8R and C3D8 [109-112].

Mass scaling allows an analysis to be carried out at low and affordable cost without unreasonably raising the loading rate. In the case of simulations having to deal with the rate-dependent material or rate-dependent damping, the solution can be gained economically only with mass scaling. The increase in the loading rate is not an alternative in these cases. This is because material strain rates rise by the same factor as the loading rate. As the properties of the materials change and shift in the strain rate, unrealistic increases of the loading rate unreasonably change the process.

## 4.5 Simulations

The numerical analyses were conducted by utilizing the *ABAQUS* / Explicit finite element program [111] to predict the quasi-static strength of the single lap joint (SLJ) with different joint configurations subjected to tensile loading. To this end, its three-dimensional finite-element (FE) model was developed (Figure 4.7).

In the models, the aluminum adherends and the steel bolt with the nut as a single part, were discretized with eight-node linear brick solid elements (C3D8R), wherein reduced integration with hourglass control was achieved. A mesh convergence study was conducted using a refined mesh in the overlap region as well as for the bolt with element sizes of 0.3 mm, 0.5 mm and 1 mm (an aspect ratio of around 1). Convergence was obtained in terms of the obtained force-displacement curve for the various meshes being less than 5% (see Figure 4.8). A mesh with an element size of 0.5 mm and a coarser mesh with a single bias ratio of 4 (towards the joining region) were used to discretize the adherend resulting in 21,752 solid elements in total for its 4 mm thickness and 12,656 solid elements to represent the steel bolt behaviour. The adhesive layer, created by partitioning from the adherend, was discretized using linear cohesive elements (COH3D8) with a total number of 1,641 (Figure 4.7). The described mesh resolution satisfied the convergence. The thickness of the adherends and the adhesive are 2, 4 and 6 mm and 0.2 mm, respectively. The boundary conditions for the specimen under axial tensile loading are presented and illustrated in Figure 3.1a; with one side fixed (clamped), and the other side with the capability of moving only in the direction of the axial tensile loading.

To represent the preloading in the BJ and HJ experiments, a coefficient of orthotropic thermal expansion was defined for the bolt material between its head part and the nut (Figure 4.7), where a reference temperature value of 40°C was assigned by using the predefined field option. Shrinkage of the bolt in the gripping region along its length inducing the bolt preload was performed with a temperature decrease of 20°C. This temperature difference was defined based on the following: The applied torque ( $T$ ) and the preload value ( $F_i$ ) were related to the each other through  $T = K.F_i.d$ , where  $K$  represents the bolt condition, such as lubricated, zinc-plated, etc., and  $d$  is the bolt diameter. For a typical  $K$  value of 0.2 [116],  $F_i$  was found to be 833.33 N, which ultimately led to a preload stress value of 41.45 MPa. Since  $\sigma_i = -E\alpha\Delta T$ , where  $\alpha$  is the

thermal expansion coefficient, the temperature difference  $\Delta T$ , was found to be  $-20^{\circ}\text{C}$ . This approach was used by Tanlak et al. [117], Egan et al. [118] and Thai et al. [119].

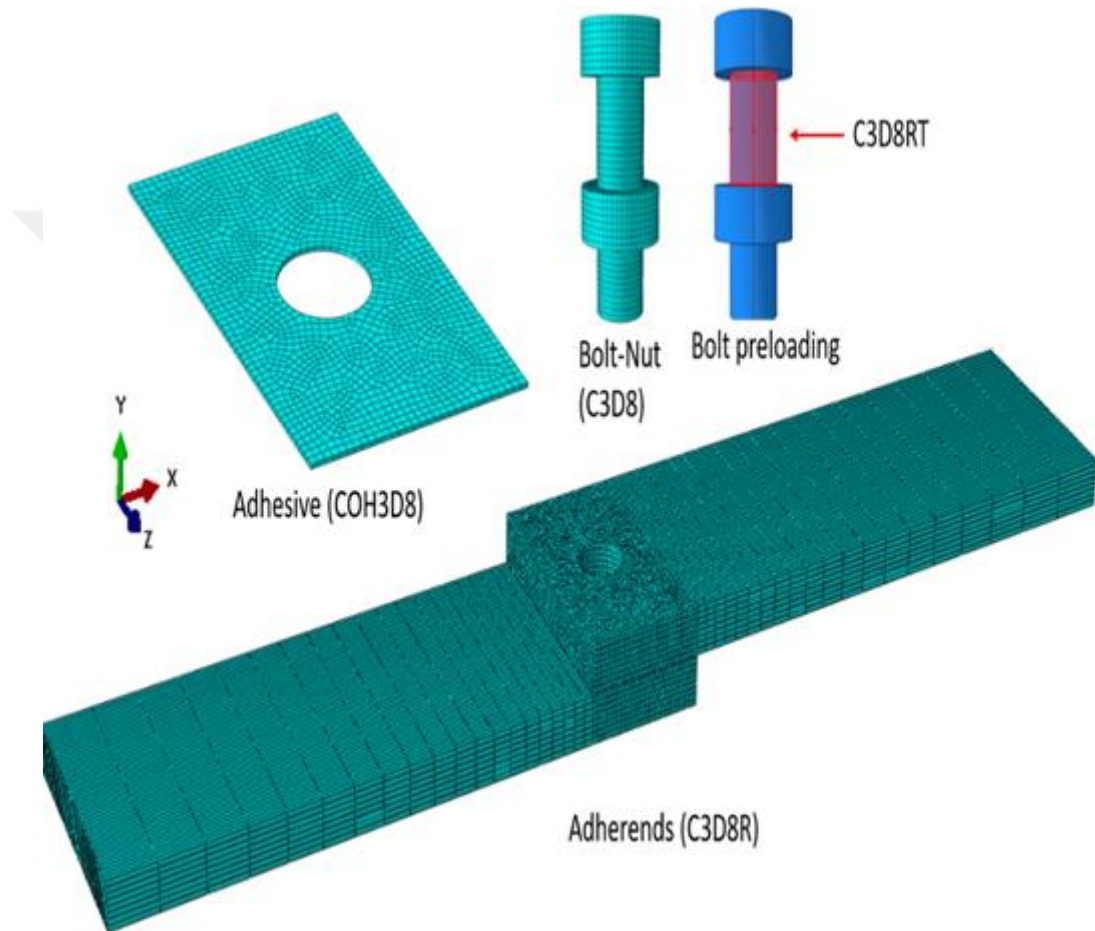


**Figure 4.7:** 3D finite element model of a single lap joint with hybrid configuration (bolted and bonded).

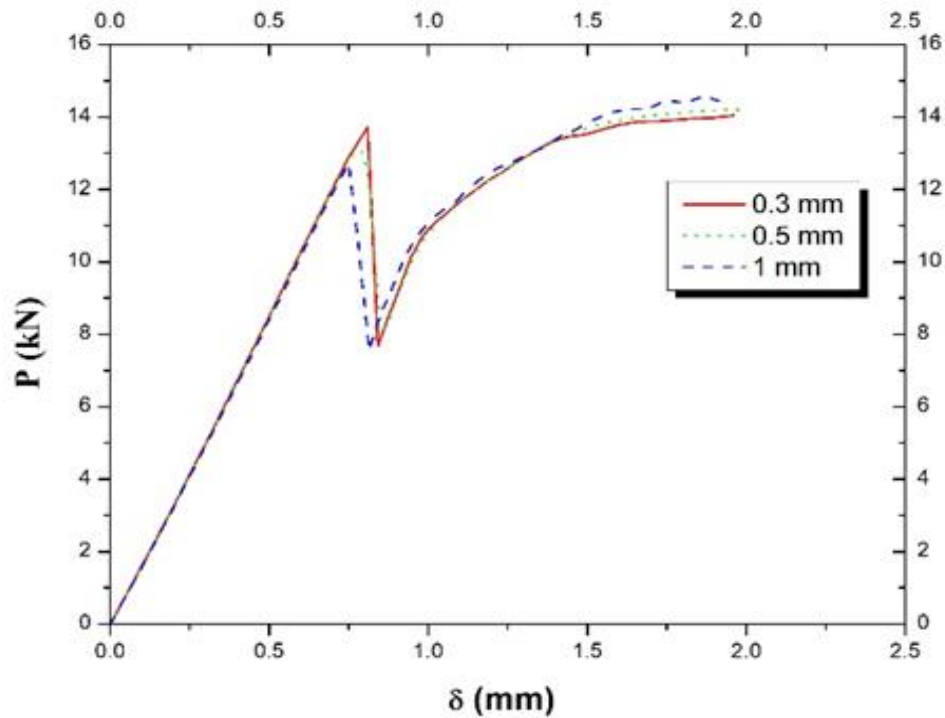


**Figure 4.8:** Study of mesh convergency regarding the force-displacement curve obtained for a HJ with 4 mm AL7075 adherends.

The general contact in *ABAQUS/Explicit* was defined between the adherend and the bolt. The friction coefficient value of 0.2 was taken for the tangential behavior following the reference in [120], and hard contact was assumed to represent the normal behavior of the bolt with regard to the walls of the hole, in other meanings, to prevent the solid elements from interfering with each other. The level of bolt-hole clearance in the models was 50  $\mu\text{m}$  in order to represent a free running fit. This value was calibrated in the HJ for an agreement between numerically and experimentally obtained a sudden drop in the  $P$ - $\delta$  curve after the adhesive layer failed, and the bolt started carrying the load (see Section 5.1.3).

Mass scaling was used in the analysis to increase the speed of the quasi-static analysis. Scaling was set to be variable and non-uniform since it is the most efficient for those models with large spectra of element sizes and damage included. The ratio of kinetic energy to the total energy to be less than 0.5% was ensured to eliminate possible dynamic effects on the results and to keep the simulations operating in a quasi-static manner.

The explicit method was selected here intentionally to avoid numerical convergence difficulties in the standard method caused by large deformations and complex contact problems. However, the initial stable time increment ( $\Delta t$ ), in the order of  $10^{-8}$ , would lead to an unacceptably large number of increments for the quasi-static problem studied here. To avoid this, mass scaling was performed with  $\Delta t$  increasing to around  $5 \times 10^{-7}$ , where a quasi-static solution was deemed to be attained as the kinetic energy was negligibly small compared to the internal energy in the model (see Figure 4.9). Some fluctuations observed in the numerically obtained force-displacement curves were due to the limited dynamic effects.

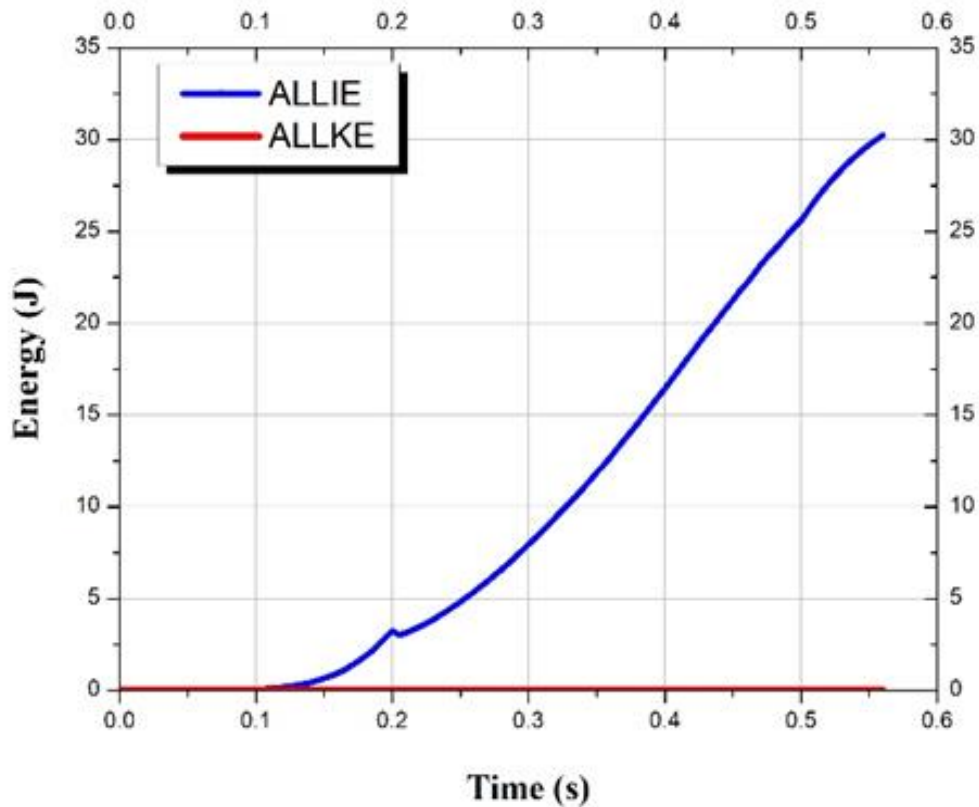


**Figure 4.9:** All internal energy (ALLIE) and all kinetic energy (ALLKE) in the model for the HJ of 2 mm AL6061 adherends.

It is important to notice that the degradation of materials and dynamic loading are the core reasons for the damage in the materials. The degradation of materials occurs because of crack initiation, and fatigue or dynamic load, which is known to be the source of crack propagation. An accurate and a more realistic modelling of metal



inelastic characteristics is the fundamental tool that is applied in the solving of a number of problems in the engineering field. There are notable numerous failure models and theories alike that predict the initiation and accumulation of the damage.

In this research, the CZM was utilized and applied to simulate the adhesive layer. Moreover, the ductile and shear damage model was applied to categorize the stiffness degradation of the adherend material and bolt materials [109-112].

In the simulations, the damage parameters presented in Table 4.1 were used. For Al6061 and AL7075, the  $\bar{\epsilon}_D^{pl}$  value as a function of  $\eta$  presented in Table 4.2 were used [121, 122]. The  $\bar{u}_f^{pl}$  value of 0.1 mm was used for both materials based on best agreement between numerically and experimentally obtained  $P$ - $\delta$  curves of the BJ's of 2 mm adherends with an overlap length of 15 mm in Section 5.1.1, where the failure occurred in the aluminium samples. To the authors' knowledge, there is no reference data for  $\bar{\epsilon}_S^{pl}$  available in the open literature of both types of aluminium; therefore, a shear damage model was not activated in the simulations. On the other hand, both ductile and shear damage models were used for steel bolt, where constant values of 1.78 and 0.7 were taken for  $\bar{\epsilon}_D^{pl}$ ,  $\bar{\epsilon}_S^{pl}$ , respectively and  $G_f=5.0$  kJ/m<sup>2</sup> in the former and  $\bar{u}_{f,S}^{pl}=0.05$  (an exponential softening with a constant of 0.7) in the latter model were considered following the study in [123].  $\bar{u}_{f,S}^{pl}$  was calibrated from the BJ's of 6 mm adherends with an overlap length of 15 mm in Section 5.1.1, where a shear failure occurred in the bolt. Following the study in [102], it is assumed that in the failure zones, the prevailing value of the shear stress ratio was 1.732. Therefore, in the shear damage model, a constant value of equivalent plastic strain at the onset of damage was used. As the experiments were performed quasi-statically, the strain rate was rolled out in the simulations. In the simulations, the element was removed from the mesh when the stiffness at every integration point reached the maximum degradation; i.e., complete damaged occurred. Figure 4.10 illustrates the various instances of onset damage corresponding to the stress triaxiality for all the materials.

In the simulations, once the damage criterion was reached, the stiffness of the material degraded following the softening law. The element was removed from the mesh when the stiffness at every integration point reached the maximum degradation; i.e., complete damaged occurred.

**Table 4.1:** Damage parameters of aluminum adherends and steel bolt materials used in the FE analysis [121-123].

Material	Ductile damage			Shear damage		
	Equivalent plastic strain $\bar{\epsilon}_D^{pl}$	Displ. at failure (Fracture Energy) $\bar{u}_{f,D}^{pl}(G_f)$	Softening law	Equivalent plastic strain $\bar{\epsilon}_S^{pl}$	Displ. at failure $\bar{u}_{f,S}^{pl}$	Softening law
AL6061	See Fig. 4.10	0.1 mm-Calibrated	Linear	-	-	-
AL7075	See Fig. 4.10	0.1 mm-Calibrated	Linear	-	-	-
Bolt grade 8.8	1.78	(5.0 kJ/m <sup>2</sup> )	Linear	0.7	0.05 mm-Calibrated	Exponential ( $\alpha = 0.7$ [102])

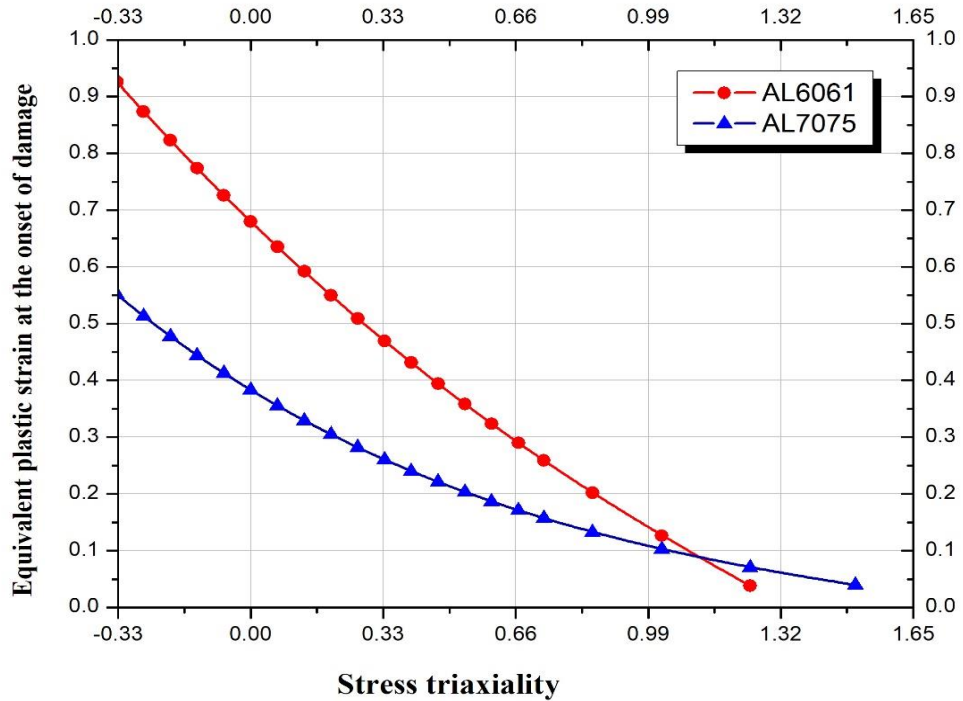


**Figure 4.10:** Equivalent plastic strain values at damage initiation as a function of stress triaxiality in the ductile damage model [102].

**Table 4.2:** Equivalent plastic strain values at damage initiation for different stress triaxiality used in ductile damage model.

	AL6061	AL7075
$\eta$	$\bar{\epsilon}_D^{pl}$	$\bar{\epsilon}_D^{pl}$
-0.33333	0.925926	0.551429
-0.26667	0.873616	0.513341
-0.2	0.822912	0.47759
-0.13333	0.773772	0.444037
-0.06667	0.726153	0.412551
0	0.68	0.383
0.066667	0.635271	0.355266
0.13333	0.591924	0.329239
0.2	0.54991	0.304809
0.26667	0.509192	0.281883
0.33333	0.469736	0.260369
0.4	0.431491	0.240175
0.46667	0.394426	0.221223
0.53333	0.35851	0.203439
0.6	0.323697	0.186746
0.66667	0.289957	0.17108
0.7301	0.258824	0.15707
0.85097	0.202007	0.132606
1.0237	0.126215	0.102188
1.2435	0.038252	0.070055

## CHAPTER 5

### RESULTS AND DISCUSSIONS

In this chapter, the bolted, bonded and hybrid single lap joints in terms of their force-displacement curves, the amount of energy absorbed, and failure modes were evaluated experimentally and numerically in a row, and relevant discussions were presented. This was conducted in the context of two main parameters: firstly, the influence of the adherend thickness and later the influence of the overlap length were considered.

#### 5.1 Influence of the Adherend Thickness

In this section, the mechanical performances of the BJ, ADJ and HJ with 15 mm overlap length were presented for three different adherend thicknesses, namely 2 mm, 4 mm and 6 mm, to study the effect of adherend thickness.

##### 5.1.1 Bolted Joints

Force-displacement ( $P-\delta$ ) curves for different thicknesses of AL6061 and AL7075 adherends, joined through bolts, obtained experimentally and with FE simulations are presented in Figure 5.1. The respective failure photographs with stress distributions on the adherend and the bolt material to failure point are shown in Figures 5.2 and 5.3.

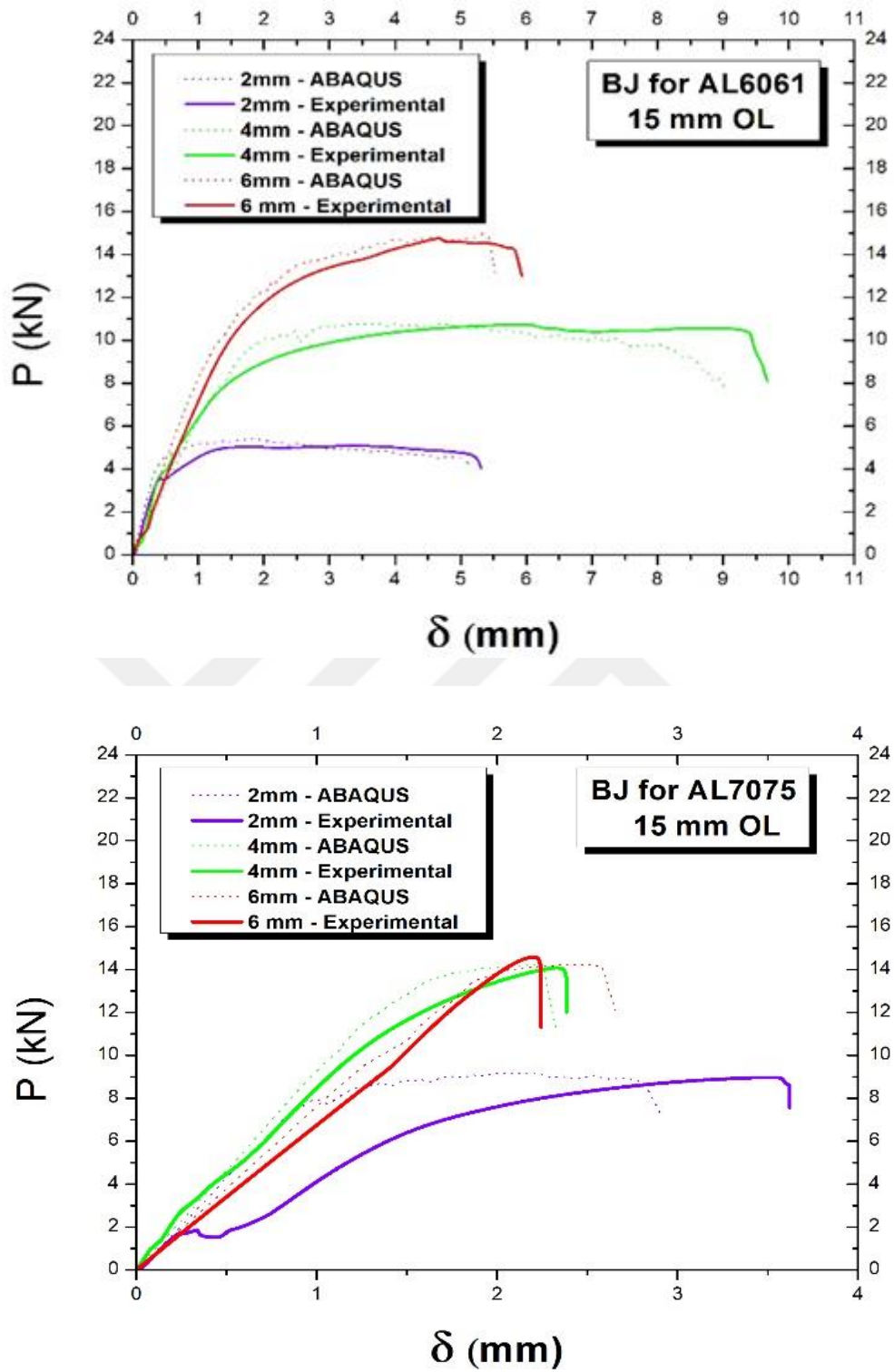


**Figure 5.1:** Experimentally and numerically obtained load-displacement curves of BJ for 15 mm OL.

**Table 5.1:** Experimentally obtained energy absorption values and failure types for different joints and various thickness of AL6061 and AL7075 adherends for 15 mm OL.

<b>Energy absorption (J)</b>				
<b>Joint type</b>	<b>Adherend material</b>	<b>2 mm OL</b>	<b>4 mm OL</b>	<b>6 mm OL</b>
<b>Bolted (BJ)</b>	AL6061	24.40(S)	91.66(S)	75.10(B)
	AL7075	22.03(S)	21.20(B)	17.10(B)
<b>Bonded (ADJ)</b>	AL6061	6.34(C)	7.42(C)	7.72(C)
	AL7075	6.44(C)	7.15(C)	8.11(C)
<b>Hybrid (HJ)</b>	AL6061	32.54(C,S)	87.36(C,S)	55.60(C,B)
	AL7075	35.50(C,S)	27.00(C,B)	23.50(C,B)

B = Bolt failure; C = Cohesive failure; S = Shear-out failure.

An agreement between the numerically and experimentally obtained P- $\delta$  curve was satisfied. From Figure 5.1, it is obvious that the strength of the BJ depends on the type of adherend and its thickness. We compared the amount of energy absorbed (EA) and the area under the force-displacement curve for AL6061 and AL7075. Table 5.1 presents the respective EA values obtained from experiments for different thicknesses of adherends joined via a bolt, adhesive and hybrid as bolt and adhesive joints together. Firstly, when the AL6061 with BJ was used in the test, it absorbed more energy than the AL7075 even though it was weaker (see Figure 3.9).

For the 2 mm adherend thickness, the amount of respective energies, 24.40 J and 22.03 J, were close to each other and failure occurred due to shear tear out for both aluminum materials (Figures 5.2 and 5.3) even though the maximum load and the displacement at failure, 5 kN/5.2 mm and 8.5 kN/3.6 mm for AL6061 and AL7075, respectively, were different.

## Chapter 5

However, for the 4 mm adherend thickness, the EA value was at least four times higher for AL6061 than for AL7075 due to the difference in failure modes, where shear tear-out and bolt failure occurred. We here note that when the adherend thickness increased, the bolt material was exposed to greater stresses, where they were even larger when AL7075 as compared to when AL6061 was used. Therefore, in this case, damage initiated on the steel bolt material earlier than the adherend followed by its ultimate failure.

However, when AL6061 was used in the tests, the bolt material was exposed to relatively less stress, delaying the initiation of its damage, whereas the weaker adherend had already failed. However, since the AL6061 was relatively ductile, its complete damage occurred at a larger displacement, i.e.,  $\delta \approx 10$  mm, hence more energy was absorbed. In the case of the 6 mm adherend thickness, bolt failure occurred first irrespective of the adherend material as the steel bolt could not sustain the applied load.

Here although the maximum load was around 15 kN for both materials, the failure displacement value was different with 7 mm and 2.4 mm for the AL6061 and AL7075, respectively. More energy was therefore absorbed with the AL6061 compared to the others, with values of 75.10 J and 17.10 J, respectively. We here note that when the stronger AL7075 was used in the test, the bolt was exposed to larger stresses and resulted in its shear failure at a smaller deformation displacement. However, in the case of another type of aluminum, the bolt was exposed to smaller stresses and hence could sustain a larger deformation displacement, namely  $\delta \approx 7$  mm. When AL7075 adherends with thickness values of 4 mm and 6 mm were tested, the resulting  $P$ - $\delta$  curves did not change significantly as the bolt in both cases had already been exposed to larger stresses and hence failed abruptly.

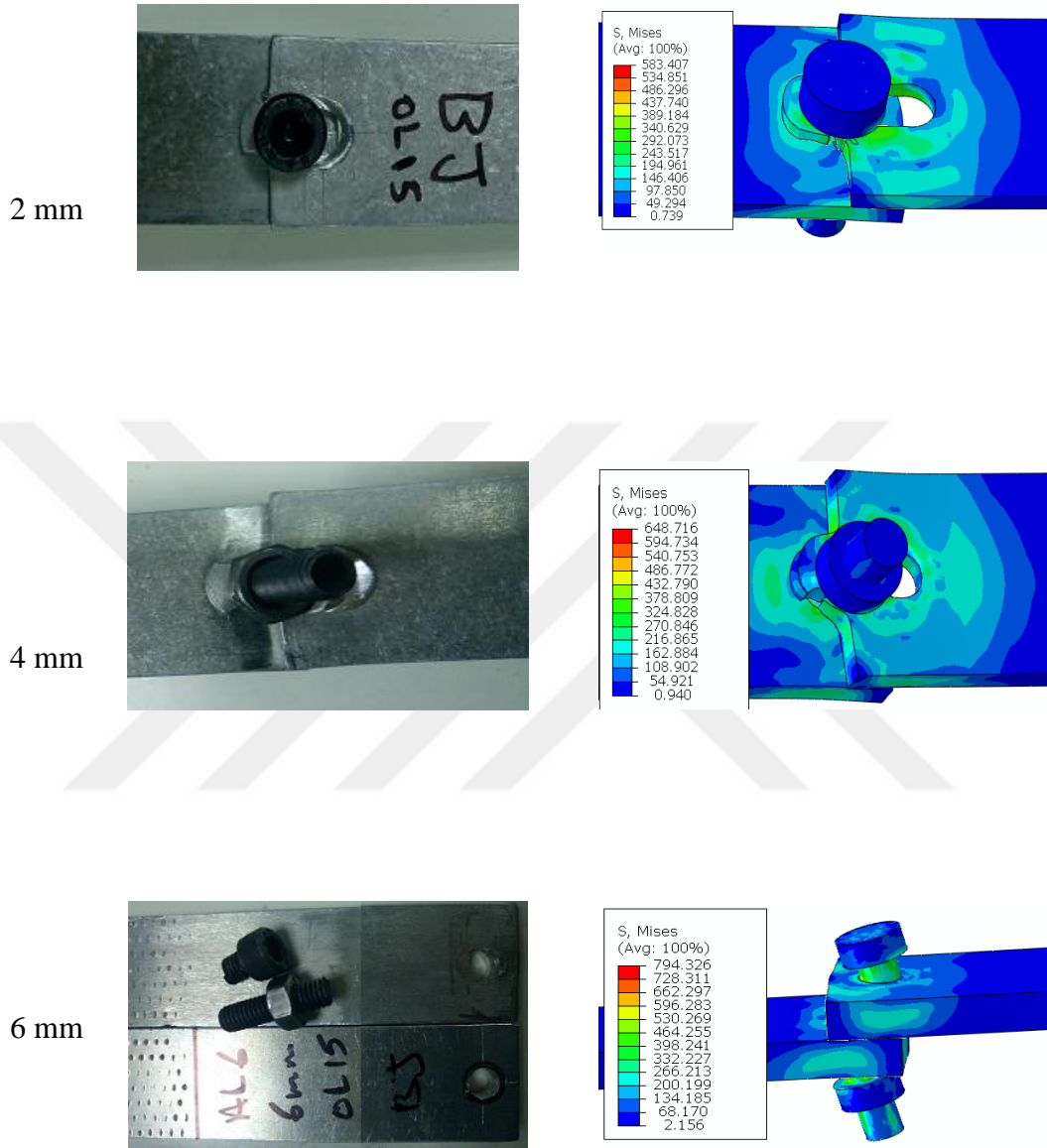


**Figure 5.2:** Experimentally and numerically obtained failure modes of the BJ for AL6061 for 15 mm OL.



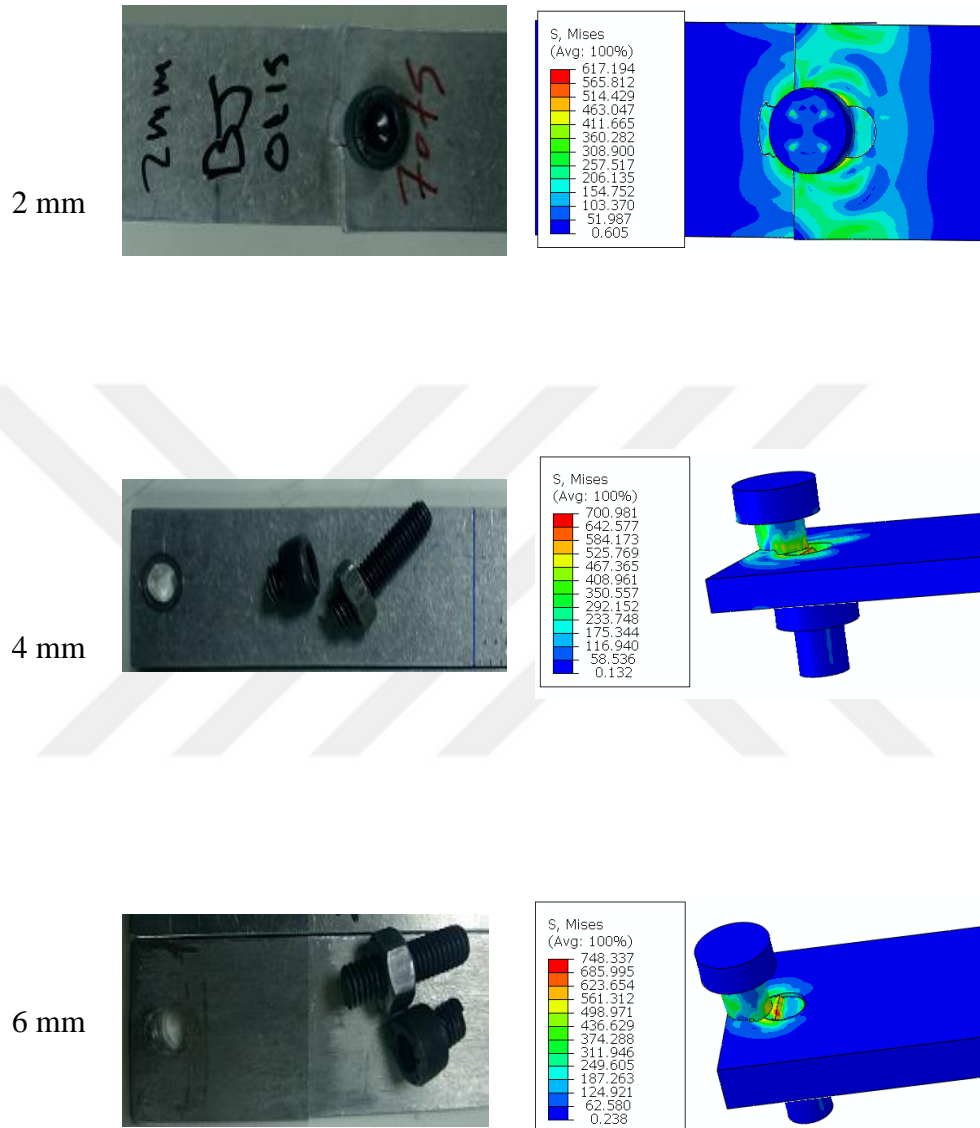


**Figure 5.3:** Experimentally and numerically obtained failure modes of the BJ for AL7075 for 15 mm OL.

### 5.1.2 Bonded Joints

Figure 5.4 presents experimentally and numerically obtained  $P-\delta$  curves for different thicknesses of AL6061 and AL7075 adherends, where they were joined via adhesive bonding. The curves obtained from the tests, and the FE simulations are substantially close to each other, confirming the robustness of the developed model. Figure 5.5 showed experimentally observed adhesive failure when the 2 mm AL6061 adherend was tested. Since adhesive failure occurred for all the cases studied here, only the result of this configuration was demonstrated as being representative. In the same figure, the stress distribution on the adherends after the adhesive layer was completely damaged and damage progress in the adhesive layer during loading via the scalar damage variable SDEG showing the degree of damage level (when  $SDEG = 1$ , complete failure reached) are presented.

We observed that when the thickness of the adherend material increased, the maximum load increased while failure displacement decreased regardless of the adherend material (Figure 5.4). It was also noted that when the comparatively weaker AL6061 was tested, as expected a smaller maximum force was obtained when compared with the other one. At the same time, a slightly higher displacement at failure was obtained since in this case, the adhesive was exposed to smaller stresses, which in turn led to sustaining the load longer. These two points explained why the absorbed energy as the area under the  $P-\delta$  curve was close to each other for all the configurations in this group (the decrease in  $P$  was compensated for by an increase in  $\delta$ , and vice versa), ranging from 6.34 J to 8.11 J (Table 5.1), as compared with those in the bolted joints, ranging from 17.10 J to 91.66 J. From Table 5.1, it can also be deduced that the BJ configuration absorbed more energy than the ADJ configurations as the EA values were far larger for the first group compared to the second group.

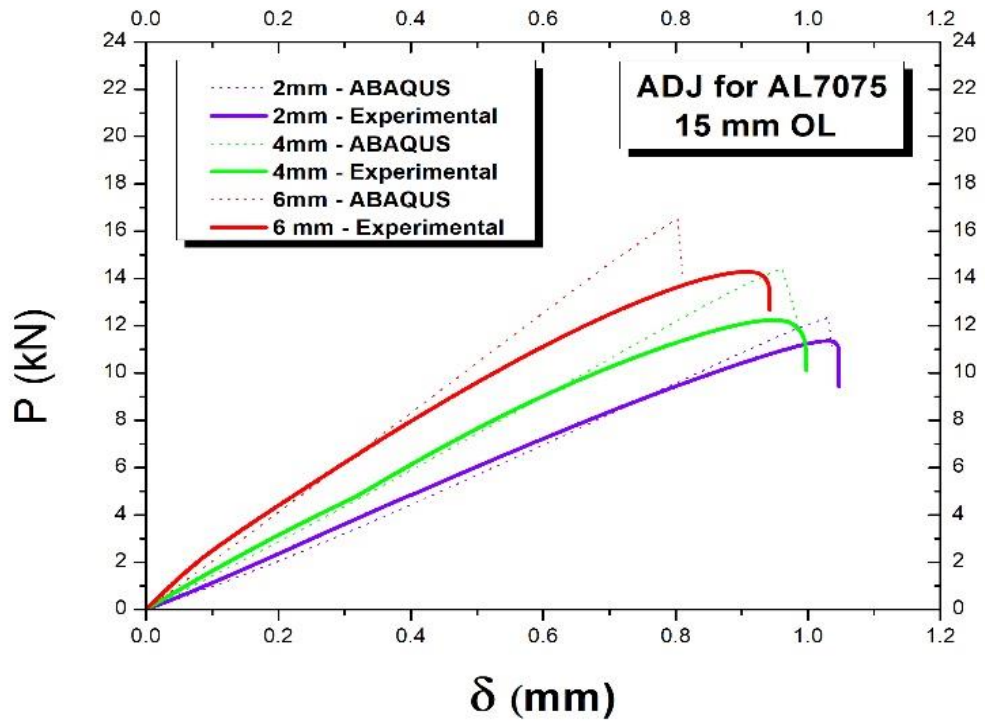
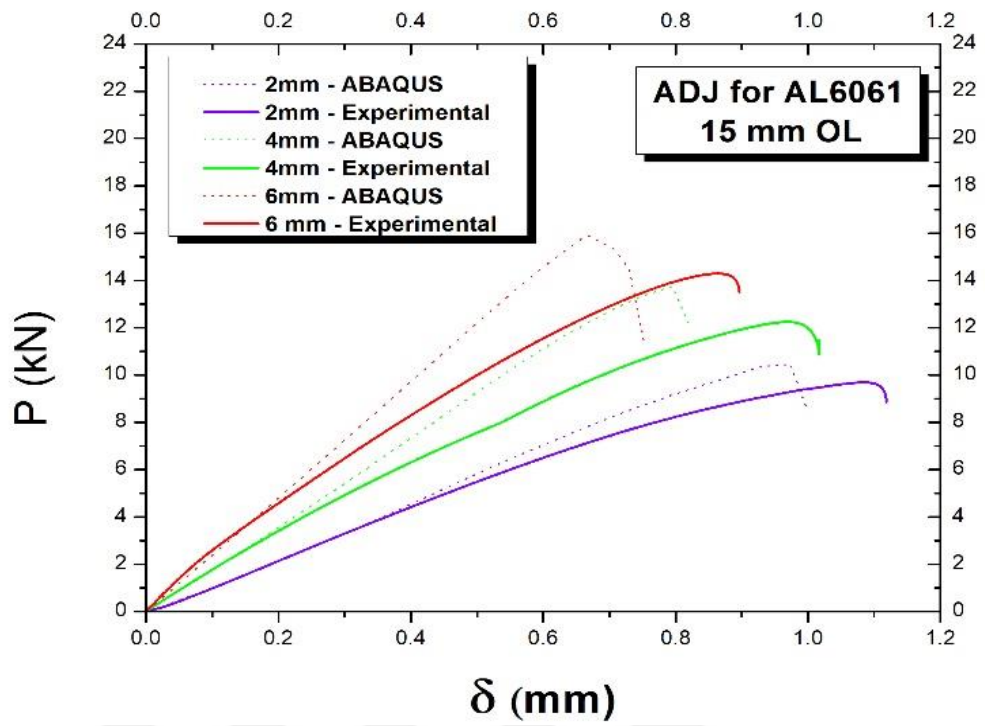


**Figure 5.4:** Experimentally and numerically obtained load–displacement curves of ADJ for 15 mm OL.

It was observed that as the damage completion occurred earlier in the adhesive layer, the strength of the joint was more dependent on the strength of the adhesive material than that of the adherend. Therefore, an increase in the adherend thickness could not be reflected proportionally in the increase of the maximum load. For instance, when the thickness of the AL6061 adherend was enlarged from 2 mm to 4 mm,  $P$  increased from 9.75 kN to just 12.25 kN. On the other hand, a proportional increase was observed in the BJ for the mentioned configurations, i.e.,  $P$  improved from 5.00 kN to 10.00 kN (Figure 5.1), where the assembly could not carry the load due to adherend failure.

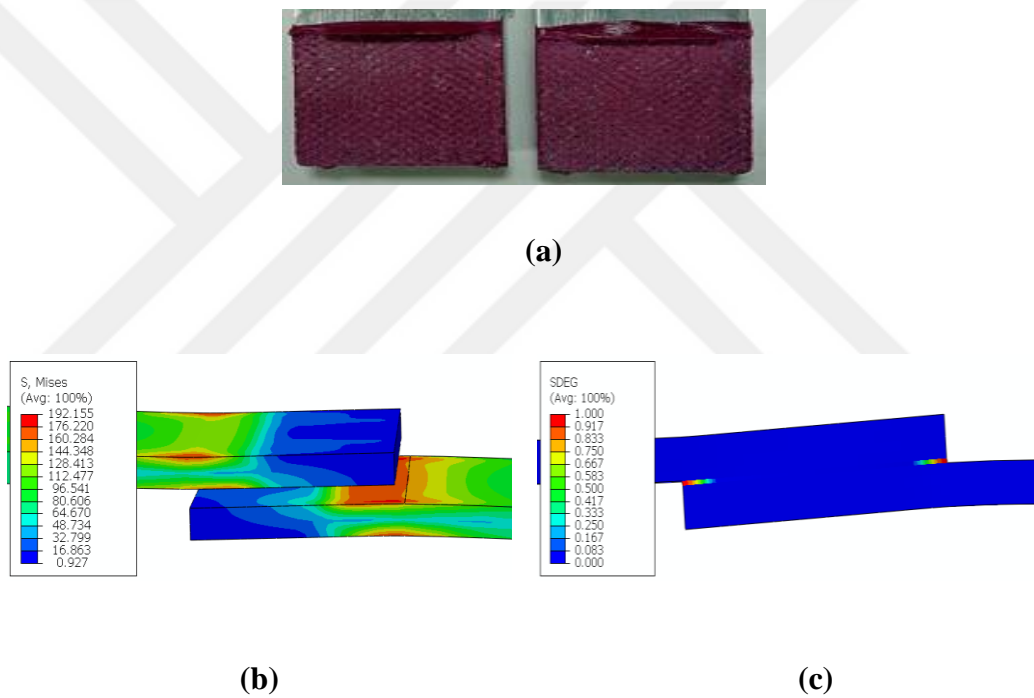


**Figure 5.5:** Experimentally (a) and numerically (b) observed adhesive failure and damage progress in the adhesive layer during deformation (c) for the 2 mm AL6061 adherends joined via adhesive bonding for 15 mm OL.

### 5.1.3 Hybrid Joints

Force displacement curves for different thicknesses of the AL6061 and AL7075 adherends, where hybrid joint configuration was used, obtained experimentally and numerically are presented in Figure 5.6. Figures 5.7 and 5.8 show the respective failure photographs and FE stress distributions on the adherend and the bolt material at the failure point.

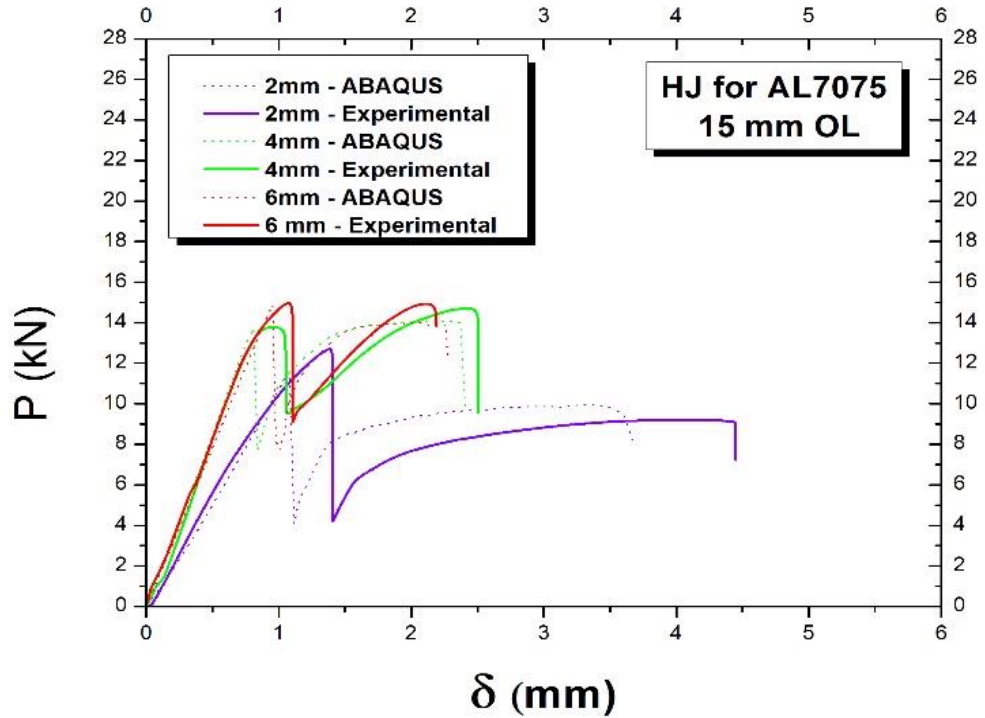
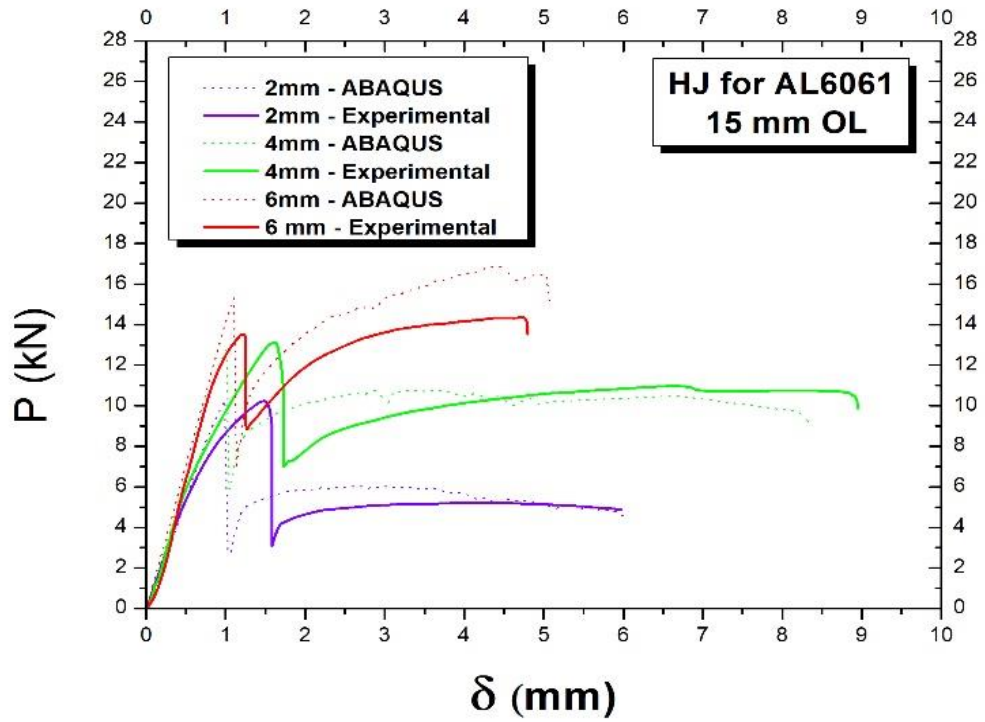


**Figure 5.6:** Experimentally and numerically obtained load–displacement curves of the HJ for 15 mm OL.

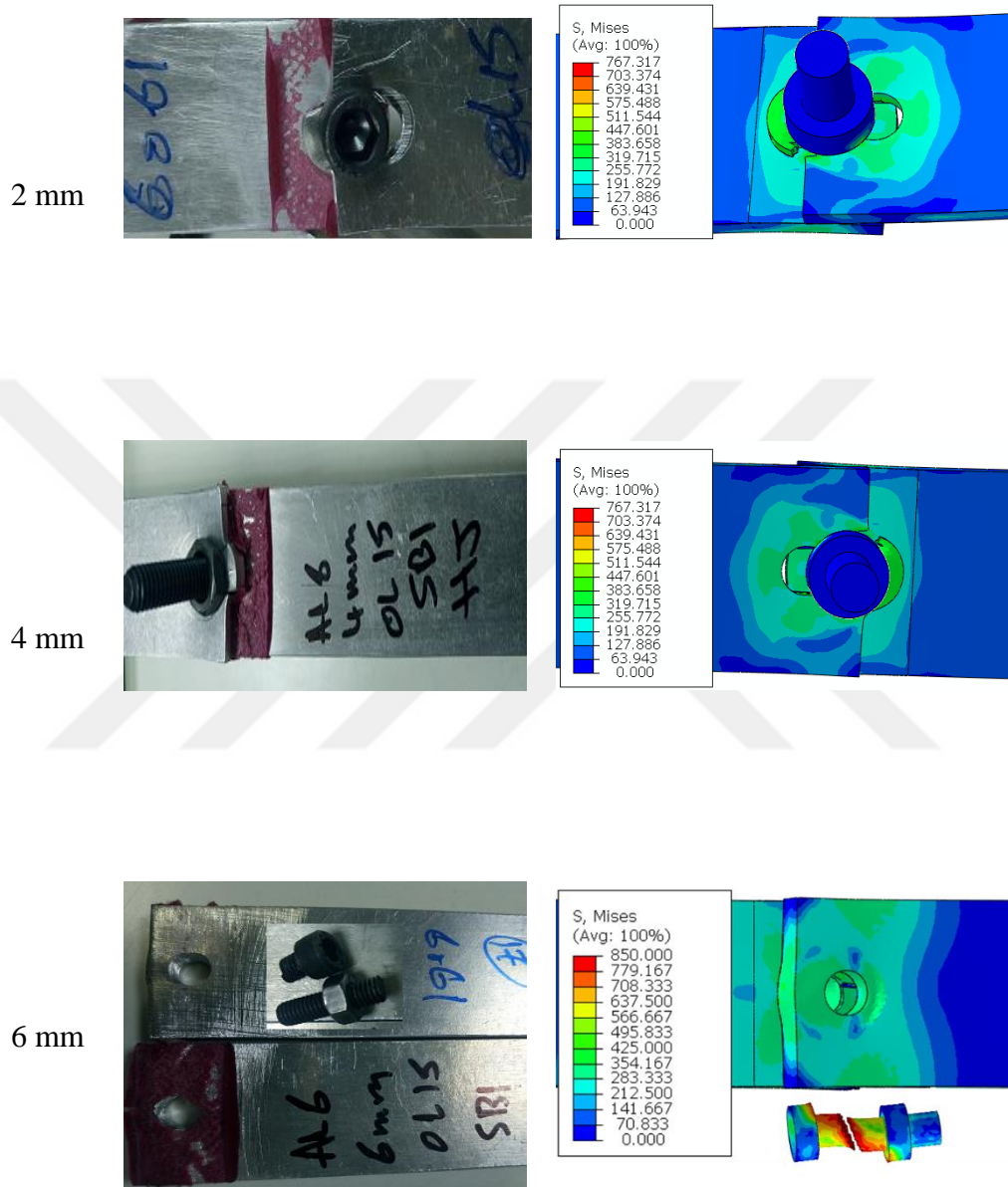


**Figure 5.7:** Experimentally and numerically obtained failure modes of the HJ for AL6061 for 15 mm OL.

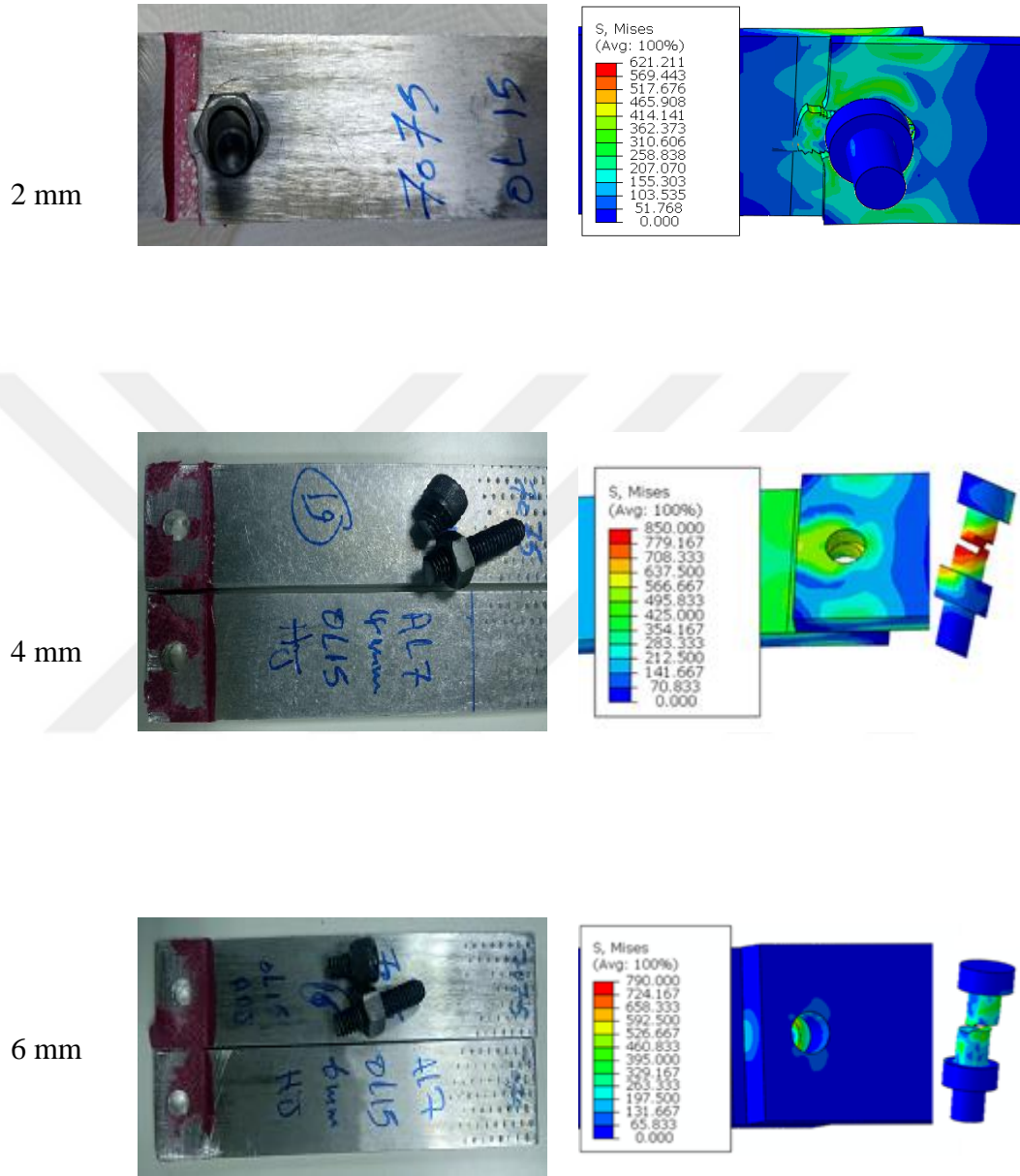


**Figure 5.8: Experimentally and numerically obtained failure modes of the HJ for AL7075 for 15 mm OL.**

Overall, an agreement between the experiments and the FE simulations was achieved. The adhesive failure occurred first for all the cases studied here, which in turn led to an abrupt decrease in the load during deformation (Figure 5.6). Afterwards, shear failure of the adherend, i.e., shear tear-out, was observed for the 2 mm and 4 mm thicknesses of the AL6061 and 2 mm of the AL7075 and the bolt failure with a slight amount of bearing deformation in the adherend occurring for all the other cases tested (Figures 5.7 and 5.8). This observation is identical to the failure modes of the BJ if we skip the initial adhesive failure in the HJ. As a hybrid joint included bolted and bonded joints together, the observations we made in  $P-\delta$  for them in Figures 5.1 and 5.4 were reflected in that of the hybrid joint, as shown in Figure 5.6.

The performance of the adhesive layer in ADJ and HJ was compared to see the influence of the bolt material. We observed that the stiffness of the joint, the initial slope of the  $P-\delta$  curve, did not change significantly for all the cases, consistent with the results in the literature [78-80, 124] [8-11] as the adhesive material studied here was relatively stiff. When a stiffer adhesive was used in the HJ, the transfer of stresses from the ends of the overlap to its middle part was less, hence the load was carried by the end regions of the adhesive layer and with a low fraction by the bolt [125]. Therefore, a slight increase in the maximum load was observed in the HJ (considering up to the failure of the adhesive layer) when compared to the ADJ. For instance, the corresponding values for the 2 mm AL6061 adherends are 10.4 kN and 9.8 kN, respectively (see Figures 5.4 and 5.6). Consequently, more energy was absorbed when HJ was used compared to ADJ; i.e., HJ was tougher than ADJ (Table 5.1). This indicates the fact that in the HJ, the bolt material supports the adhesive layer and delays its complete failure. The high strain capability of a flexible adhesive such as SBT 9244 provides for the transfer of more stresses from the ends of the overlap to the middle part of the overlap and results in an increase in the load carried by the SLJs with SBT 9244. Furthermore, the flexible adhesive layer handles the high strains and plastic deformations on the adherend material by reducing and distributing the peel stress, which greatly affects its performance [126]. Figure 5.9a presents the respective stress distribution in the adhesive layer and the bolt material just before the complete damage of the adhesive layer was attained. It was observed that the adhesive layer was greatly exposed to stresses whereas the gripping region of the bolt material partially experienced smaller amount of stresses without damage initiated. Therefore, most of



## Chapter 5

the load was carried by the former. As seen in Figure 5.9b, where the stresses in the bolt just before and just after the failure in the adhesive layer were compared, the load was transferred to the bolt material in this period as the stresses increased dramatically. We here concluded that the bolt material did not support the adhesive layer until its failure in the HJ.

On the one hand, when the EA values in the BJ and HJ configurations were compared, the latter generally absorbed more energy than the former. However, interestingly, when 6 mm AL6061 adherends were joined via a bolt, more energy was absorbed than when joined via bolt and adhesive together (75.10 J/55.60 J); i.e., it became less strong. The underlying reason was as follows: In the HJ, the amount of EA increased up to the failure of the adhesive layer; afterwards, the bolt was directly exposed to larger stresses and hence could not sustain this load longer, and ultimately it was broken.

On the other hand, when only the bolt was used to join the adherends, the bolt was exposed to loading from zero and increased gradually, where in the meantime, the bolt started to rotate due to bending effects because of the loading misalignment; hence as the bearing area also increased, more loads were carried by the adherend, which in turn delayed the development of damage in the bolt, and more energy could be absorbed. Figure 5.10 shows the deformed shape of the bolt in the BJ and HJ where the x displacement values, just before its complete damage was attained, are presented. As can be observed, the bolt displaced more in x direction, whereas it was rotated more in the BJ configuration and therefore, the bearing area increased compared to those in the HJ. As the adhesive material studied here was relatively brittle, the rotation of the overlap region was more likely to occur, which in turn, led to an occurrence of a crack initiation in this region, when compared with the flexible adhesive handling the high strains and plastic deformations on the adherend material by reducing and distributing the peel stress, which greatly affected the performance [126].

For the 4 mm AL6061 adherends, the EA values were closer to each other for the BJ (91.66 J) and HJ (87.36 J) configurations since the peak in the load at the first stage in the HJ was due to the presence of adhesive which did not significantly contribute to the EA. Moreover, as the bolt had not been exposed to larger stresses, and after the adhesive was broken as in the case of 6 mm, it could carry a load of up

to  $\delta \approx 9$  mm, which was very close to that of the BJ ( $\delta \approx 10$  mm).

In the study of Sadowski et al. [75], it was concluded that the EA of the hybrid joint was equal to the sum of the EA for the adhesive and the rivets individually. A similar observation here might be made when the AL7075 adherend was considered since the EA of the HJ configuration was close to the summations of the BJ and ADJ configurations since the corresponding values were 28.47 J/35.50 J (2 mm), 28.35 J/27.00 J (4 mm), and 25.21 J/23.50 J (6mm), respectively. Such an observation was only correct for the 2 mm AL6061 adherend with the respective values of 30.74 J/32.54 J, while for the 4 mm and 6 mm AL6061 adherends, this statement was not true.

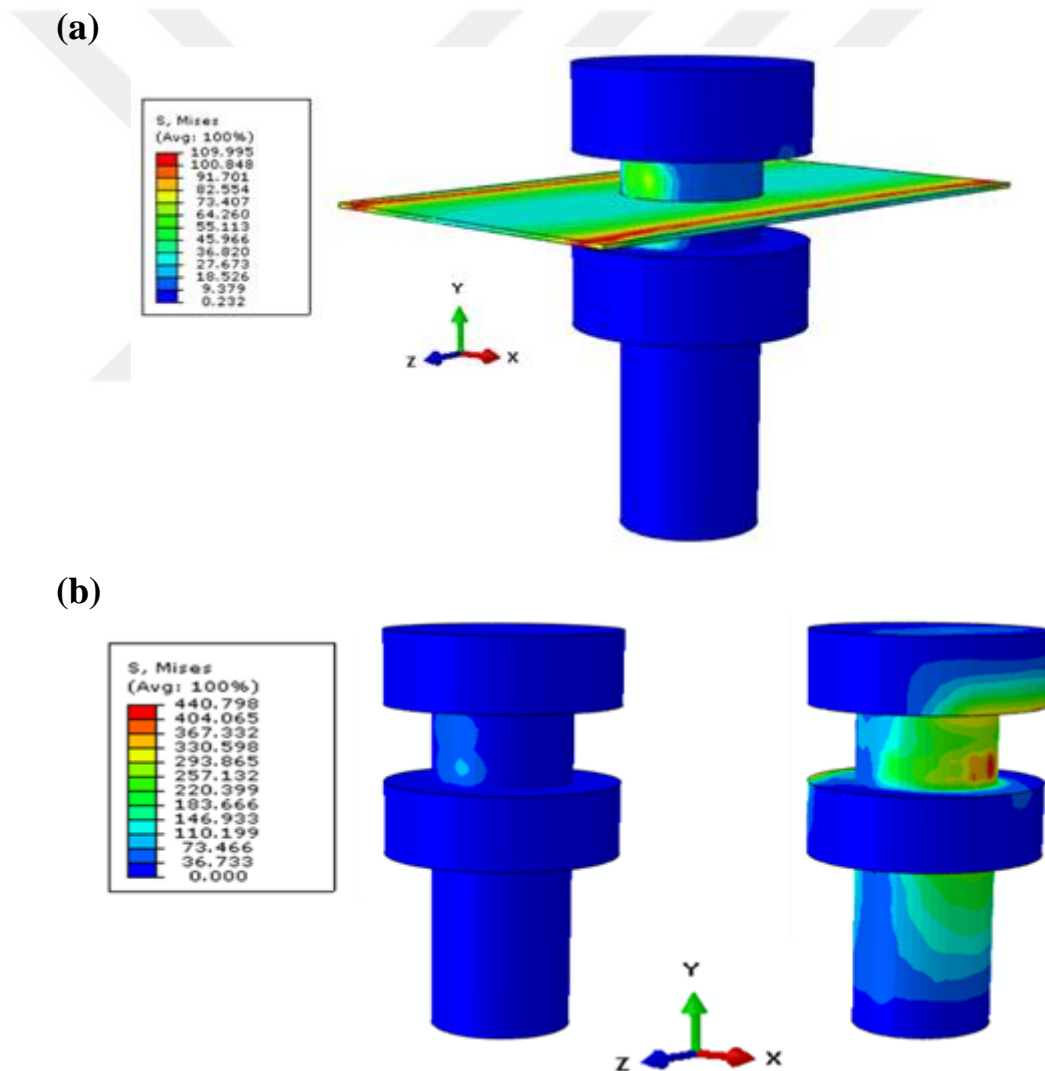


**Figure 5.9:** Stress distribution in the adhesive layer and the bolt material just before the complete damage of the adhesive layer was attained (a) and the comparison of stresses in the bolt just before (left) and just after (right) complete damage in the adhesive layer for hybrid joint of 2 mm AL6061 adherends

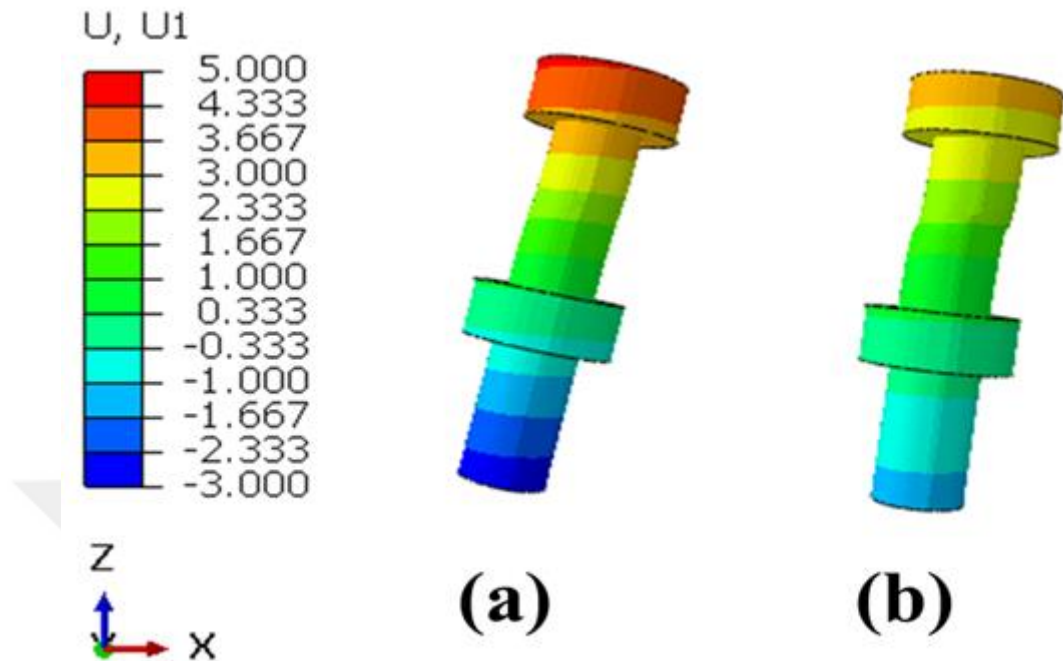


**Figure 5.10:**  $x$ -displacement of the bolt (just before its complete damage was attained) for 6 mm AL6061 adherends via bolted (a) and hybrid (b) joint configurations for 15 mm OL.

## 5.2 Influence of the Overlap Length

In this section, the mechanical performances of the BJ, ADJ and HJ with 25 mm and 45 mm overlap length are presented to study the effect of the overlap length.

### 5.2.1 Bolted Joints

Figure 5.11 presents the force-displacement ( $P$ - $\delta$ ) curves for the bolted SLJs of the three thicknesses of AL6061 and AL7075 adherends with  $OL = 25$  mm and 45 mm obtained experimentally and numerically. A good agreement between them was achieved.

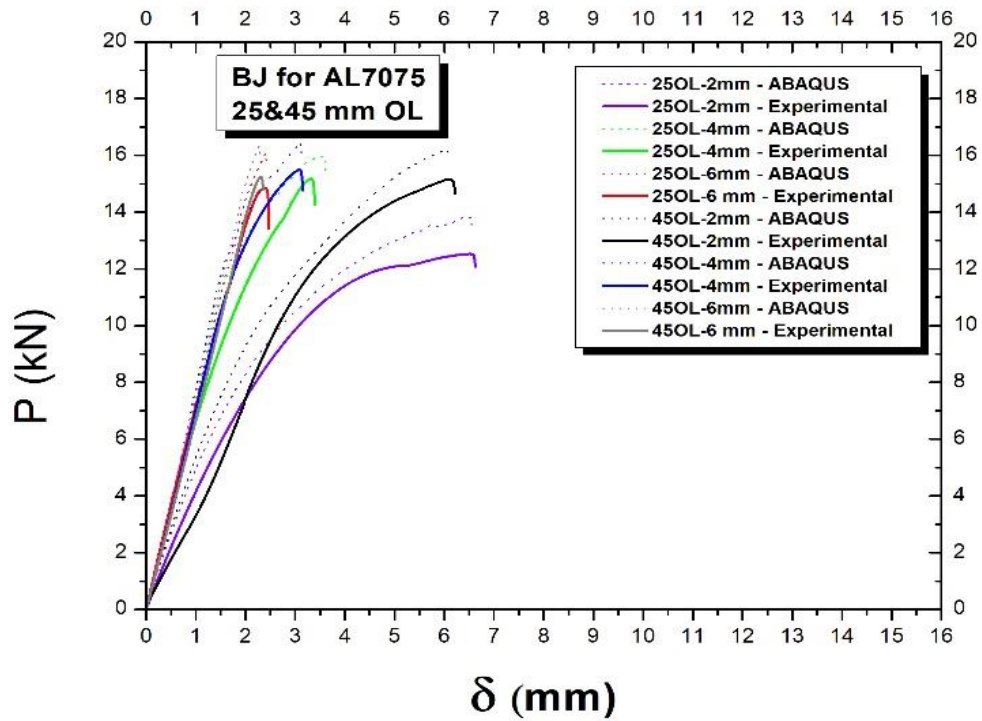
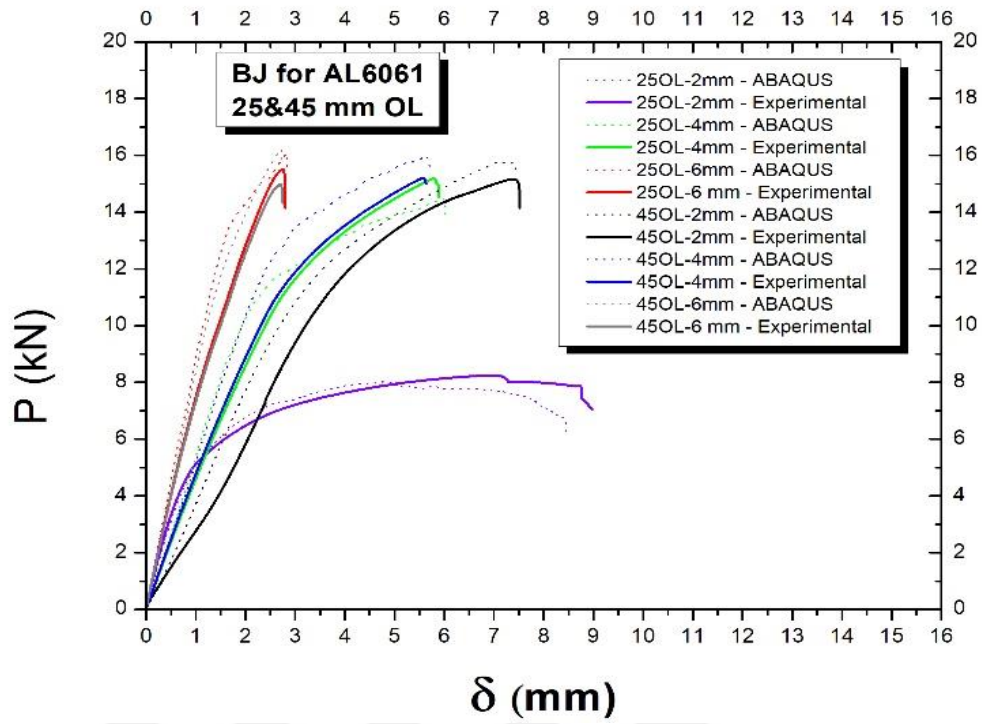


**Figure 5.11:** Experimentally and numerically obtained load displacement curves of bolted joints.

For the 2 mm thickness of AL6061 and AL7075, with an increase in the overlap length from 25 mm to 45 mm, the maximum force value that the single lap joint carried increased from 8 kN to 15 kN for the former and 12 kN to 15 kN for the latter, while the respective failure displacement values decreased from 9 mm to 7.5 mm and from 6.5 mm to 6 mm (Figure 5.11). Table 5.2 presents the amount of energy absorbed (EA), the area under the force-displacement curve, obtained from experiments for different SLJs, adherend thicknesses and overlap lengths, including the failure modes of the SLJs leading to the deficiency in carrying the load. The respective amount of energies absorbed increased from 63.4 J to 73.2 J for AL6061 and from 59.7 J to 60.5 J for AL7075.

It was experimentally and numerically observed that with an increase in the OL, the failure mode was changed from net-tension into bolt failure for both materials. The respective failure photographs and numerically obtained stress distributions on the adherend and the bolt materials at failure point are shown in Figure 5.12.

Our FE simulations demonstrated that with an increase in deformation, in the overlap region especially, that the bolt started to rotate due to bending effects as a result of the loading misalignment. Since the moment of inertia for the adherends with shorter overlap lengths was smaller, the bolt rotated more, as seen from Figure 5.13a, then the deformation was constrained into smaller surface area of the adherends (see the hole in Figure 5.13b with a sharper tip); which in turn; accelerated the damage evolution in the bearing area of the adherends and ultimately led to net-tension failure. For  $OL = 45$  mm, however, failure of the bolt occurred earlier as the larger surface area of the adherends in contact with the bolt delayed the net-tension failure.

It should be noted that this failure mode here was related to the geometrical constraints of the SLJ. The ratio of  $OL/2$  to  $d_{bolt}$  defines either the shear-out failure or net tension failure that occurs for the SLJs with smaller thickness adherends such as 2 mm, where for its smaller value, the first failure mode, and for the larger one, the second failure mode is activated [21]. In line with this, for  $OL = 25$  mm, the respective ratio was 2.08 and net tension failure occurred for 2 mm adherend thickness of both materials. In our previous study (Section 5.1.1), for the OL of 15 mm with a corresponding ratio of 1.25, shear-out failure in the adherends occurred and a similar observation was achieved in [21].

**Table 5.2:** Experimentally obtained energy absorption values and failure types for different joint configurations with 25 mm and 45 mm overlap lengths and various thicknesses of AL6061 and AL7075 adherends.

<b>Energy absorption (J)</b>							
		2 mm Thickness		4 mm Thickness		6 mm Thickness	
Joint type	Adherend materials	25 mm OL	45 mm OL	25 mm OL	45 mm OL	25 mm OL	45 mm OL
Bolted (BJ)	AL6061	63.4(N)	73.2(B)	59.1(B)	56.6(B)	25.7(B)	24.4(B)
	AL7075	59.7(N)	60.5(B)	31.6(B)	30.3(B)	20.8(B)	19.4(B)
Bonded (ADJ)	AL6061	32.6(C)	170.7(C)	22.2(C)	44.9(C)	13.7(C)	29.4(C)
	AL7075	29.7(C)	119.7(C)	21.5(C)	33.0(C)	14.9(C)	29.9(C)
Hybrid (HJ)	AL6061	120.7(C,N)	245.5(A)	66.9(C,B)	85.5(C,B)	33.3(C,B)	52.6(C,B)
	AL7075	83.0(C,N)	167.3(C,B)	44.8(C,B)	50.6(C,B)	32.3(C,B)	43.1(C,B)

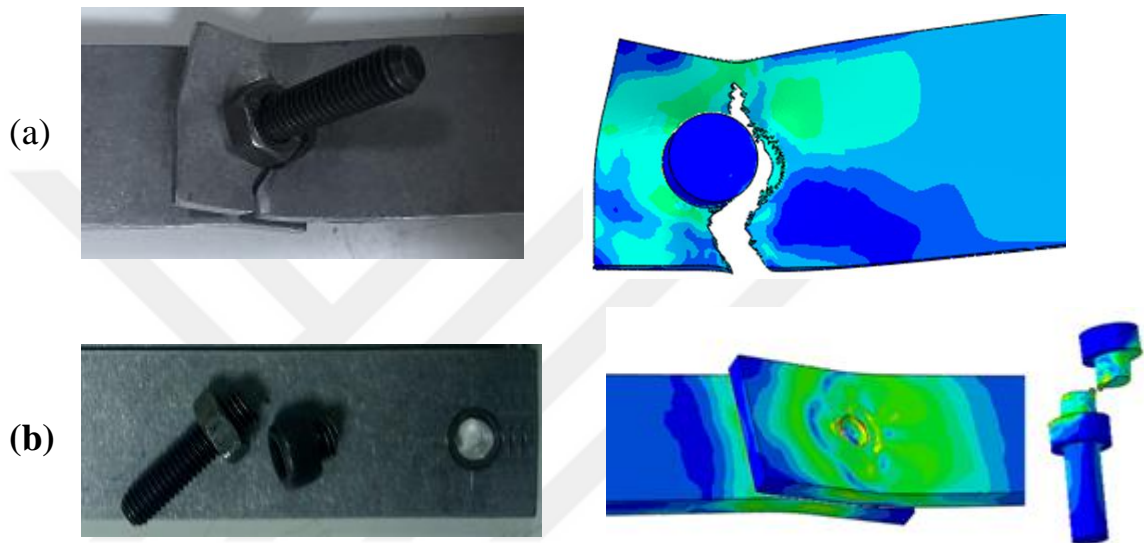
A = Adherend failure; B = Bolt failure; C = Cohesive failure; N = Net-tension failure

With an increase in the adherend thickness from 2 mm to 4 mm or to 6 mm, since the bolt material was exposed to larger stresses and with damage initiated to the respective surface areas, ultimately the bolt failure occurred irrespective of the overlap length. A maximum force value of 15 kN was obtained for all the respective failures as this was the capacity that the bolt material could carry (Figure 5.11). It is worth mentioning that the larger thickness of the adherends constrained the rotation of the bolt. Therefore, the OL did not influence the performance of the SLJs, unlike the case explained above, and very close EA values were obtained for different OL values (Table 5.2).

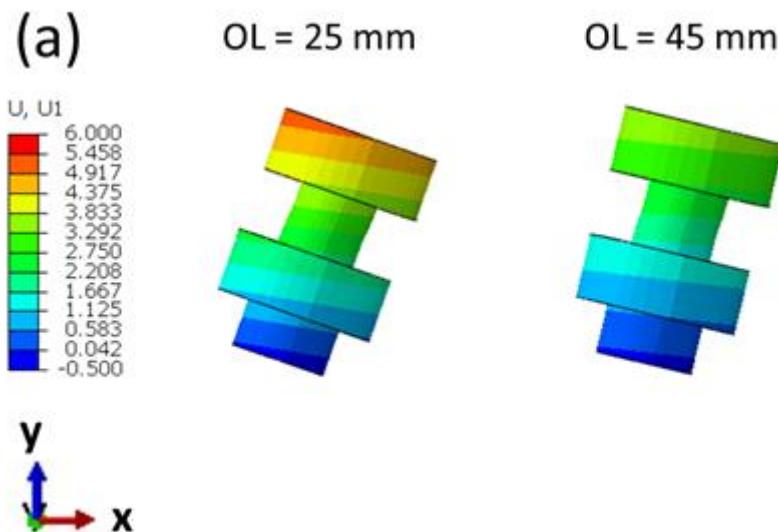
Interestingly, for the cases that the SLJ failed due to bolt failure, the BJ with the AL6061 adherends absorbed more energy than those with the AL7075 adherends (Table 5.2). When the AL6061 was tested, the bolt material was exposed to relatively fewer stresses, thereby delaying the initiation of its damage, whereas the stronger AL7075 enforced the bolt significantly; hence it reached its tensile strength earlier, which ultimately resulted in its earlier failure; i.e., it had a smaller failure

displacement ( $\delta_f$ ).

Since the bolt could carry a maximum force value of 15 kN regardless of the adherend material, the amount of EA as the area under the force-displacement curve was smaller for the BJ of AL7075 adherends. In parallel with this, an increase in the adherend thickness also led to the bolt material being exposed to larger stresses; hence failure of the SLJs due to bolt failure occurred at a smaller  $\delta_f$  value. The EA value was therefore smaller for thicker adherends of both aluminum materials.



**Figure 5.12:** Failure modes observed in bolted joints: (a) Net-tension failure and (b) Bolt failure (Left: Experimental, Right: FE simulation)



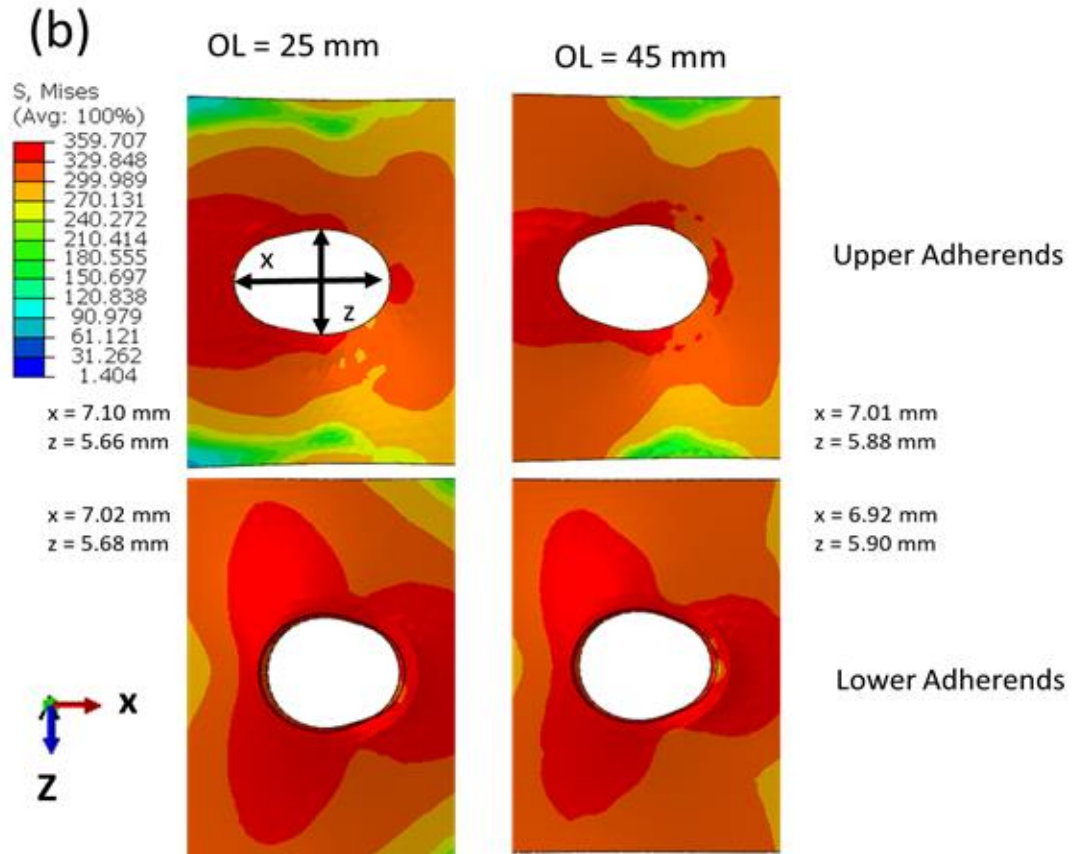


**Figure 5.13:** x-displacement of the bolt (just before the damage initiated on the bolt surface) (a) and the bearing area for the upper and lower adherends (b) in the bolted joints of 2 mm AL6061 adherends for both 25 mm and 45 mm overlap lengths

### 5.2.2 Bonded Joints

Figure 5.14 presents experimentally and numerically gained  $P-\delta$  curves for different thicknesses of AL6061 and AL7075 adherends joined via adhesive bonding with two overlap lengths. The obtained curves are substantially close to each other, thereby confirming the robustness of the developed model. Cohesive failure occurred for all the cases studied here (Table 5.2).

It is worth mentioning that the bonds are separated from each other from their half thickness showing that the adhesive was well placed between the adherends.



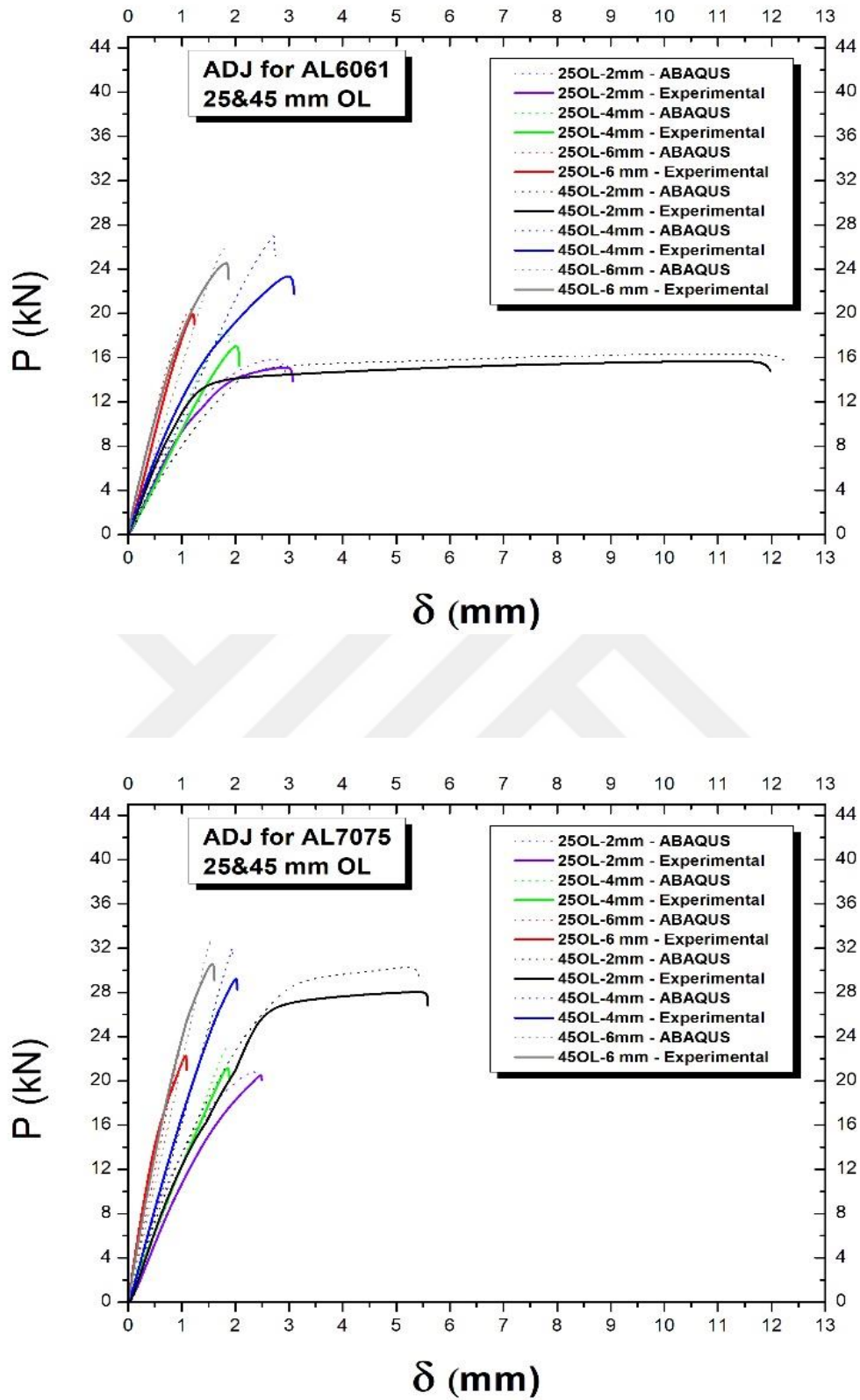


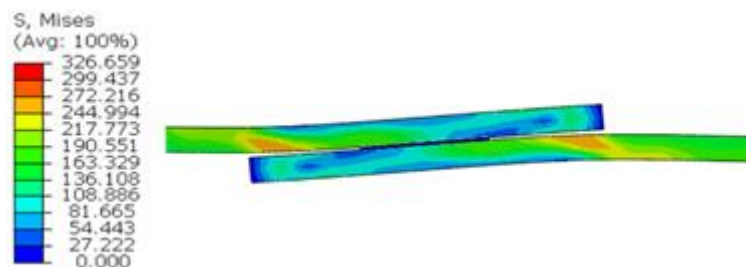
**Figure 5.14:** Experimentally and numerically obtained load displacement curves of bonded joints.

## Chapter 5

For the 2 mm thickness of the AL6061 adherends, with an increase in the overlap length from 25 mm to 45 mm, while the obtained maximum force value did not change to a value of around 15 kN, the failure displacement value increased significantly from 3 mm to 12 mm (Figure 5.14). The absorbed energy, therefore, increased from 32.6 J to 170.7 J. The FE simulations demonstrated that the adherend materials were stretched and deformed plastically, where the plateau in the stress-strain curve was reached (Figure 3.9), whereas the damage occurred in the adhesive layer, and eventually cohesive failure occurred (Figure 5.15). Since with an increase in the OL, the stresses in the adhesive layer were smaller due to an increase in the area, the SLJ could carry the load for larger displacement values. However, when stronger AL7075 adherends were tested for the same thickness value, the damage in the adhesive layer already started before the plateau in the stress-strain curve of AL7075 was reached for  $OL = 25$  mm (Figure 5.16- bottom). Therefore, the adhesive joint failed at  $\delta = 2.5$  mm. On the other hand, for  $OL = 45$  mm, the damage initiation in the adhesive layer was delayed due to its larger area, hence the tensile strength of 540 MPa was already attained in the material points of adherend material, i.e. the plateau in the curve was reached (Figure 5.16 - top) leading to saturation of the force value at 28.0 kN until the adhesive failure at  $\delta = 5.5$  mm.



(a)



(b)

**Figure 5.15:** Cohesive failure observed in bonded joints (a: Experimental, b: FE simulation)

Both aluminum adherends in the larger thicknesses were naturally exposed to fewer stresses, henceforth reaching the respective plateaus in their stress-strain curves becoming less likely. In the meantime, the damage in the adhesive layers already started, which resulted in cohesive failure at a smaller  $\delta$  compared to cases with 2 mm adherend thickness. However, with an increase in the OL, the damage initiation in the adhesive layer was delayed as mentioned above, hence an increase in both the maximum  $P$  and  $\delta$  values was obtained. Therefore, the EA value increased significantly. For instance, for the 4 mm and 6 mm thickness of AL6061, the EA reached 44.9 J from 22.2 J and 29.4 J from 13.7 J when the OL was increased to 45 mm from 25 mm. A similar observation is valid for AL7075 adherends (Table 5.2).

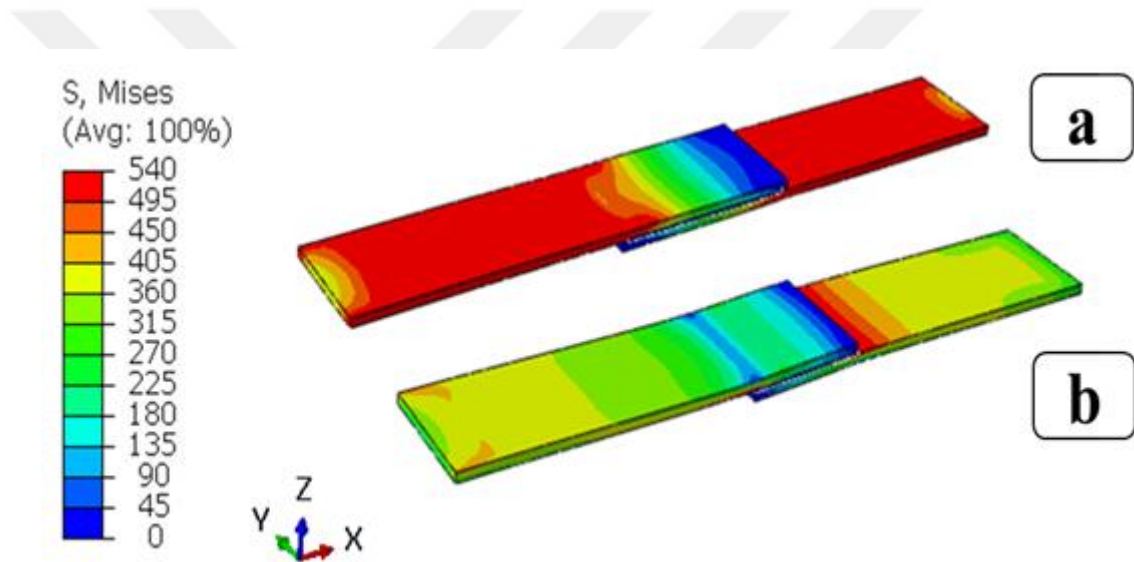


**Figure 5.16 :** Stress distributions (just before the cohesive failure occurred) in the 2 mm thickness of AL7075 adherends with bonded joints for the overlap length of 45 mm (top) and 25 mm (bottom)

### 5.2.3 Hybrid joints

The experimental and numerical force displacement curves of the hybrid joint configuration are presented in Figures 5.17 and 5.18. Overall, an agreement between experiments and FE simulations was achieved.

When the OL of the 2 mm AL6061 adherends joined via a bolt and adhesive together were increased from 25 mm to 45 mm, the maximum load remained constant with a value of 15 kN and the failure displacement value increased from 11.5 mm to

16.5 mm (Figure 5.17). The EA value increased to 245.5 J from 120.7 J (Table 5.2). It was observed that the failure mode changed from cohesive failure followed by the net-tension failure into adherend failure. In fact, the former failure was a combination of the failures of bolted and bonded SLJs alone from the cases discussed above. For the shorter OL, the adhesive layer was exposed to higher stresses and hence failed first, and later since the bolt was stronger than the 2 mm adherends, net-tension failure in the adherend material occurred. Here the force that the HJ could carry abruptly decreased to 3 kN with the complete damage in the adhesive layer was attained followed by an increase up to 8 kN as the adherends started mostly carrying the load up to occurrence of net-tension failure (Figure 5.19b).

However, when the OL was 45 mm, instead of any combinations of bolt and cohesive failures, which were observed in the BJ and ADJ individually, only adherend failure occurred. This can be explained by the fact that the bolt material and the adhesive layer with its larger area supported each other, hence their own failures were delayed, whereas the stresses in the adherend material increased gradually, and the plateau in Figure 3.9 was reached. Finally, due to damage initiation and evolution, the adherend material was broken far from the overlap region (Figure 5.19a). On the other hand, when the 2 mm AL7075 adherends with the HJ were tested, the corresponding failure modes of the ADJ and BJ occurred sequentially, where it was the cohesive and net tension failures for OL = 25 mm, cohesive and bolt failures for OL = 45 mm. The former P value dropped from 21 kN to 8 kN suddenly without saturating after the cohesive failure occurred, which then escalated to 12 kN and saturated there till the net tension failure occurred (Figure 5.18). In the latter, parallel P  $\delta$  behavior was observed, but the force value was already saturated to 28 kN as the stresses in the adherend materials reached the plateau before the adhesive failure occurred, causing a sudden drop in the force value followed by a second increase as the bolt started carrying the load (Figure 5.18). Since the AL7075 was stronger than the AL6061, the adherend failure was not observed here. With an increase in the adherend thickness from 2 mm to 4 mm or 6 mm, cohesive and bolt failures (Figure 5.19c) in a row occurred for the HJ of both adherend materials as the net tension or adherend failures were eliminated for thicker geometries.

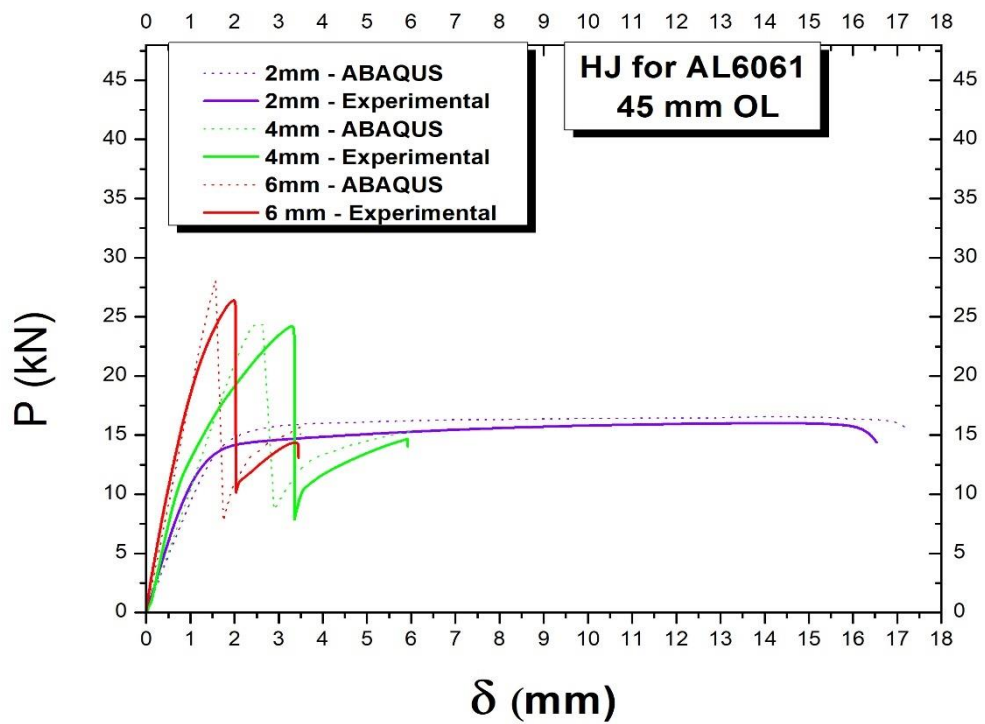
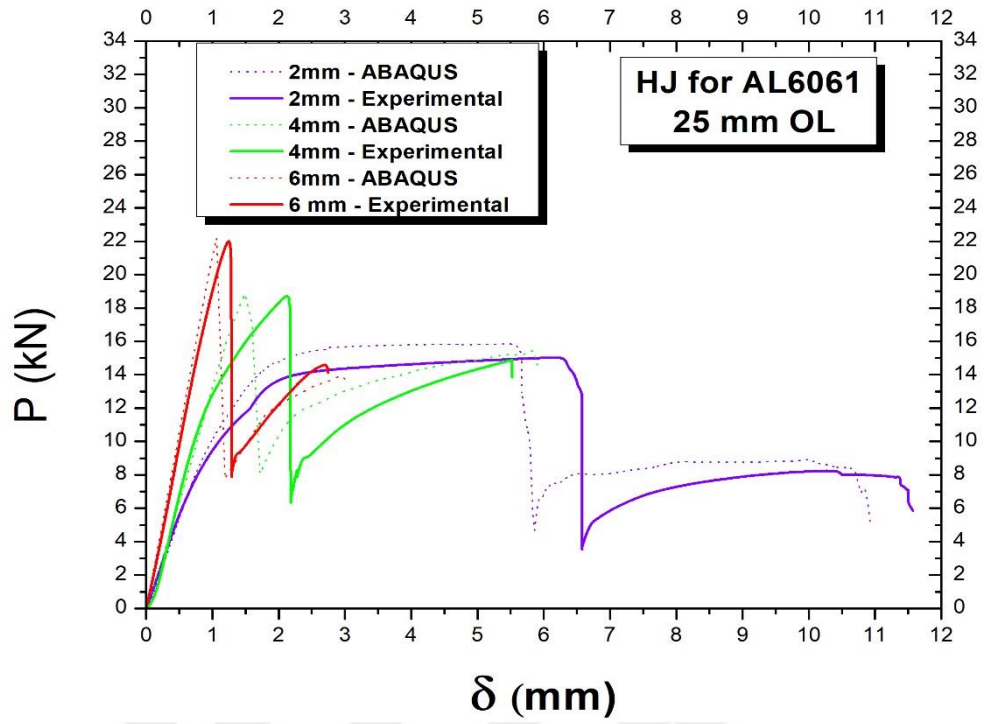


**Figure 5.17:** Experimentally and numerically obtained load displacement curves of HJ of AL6061.

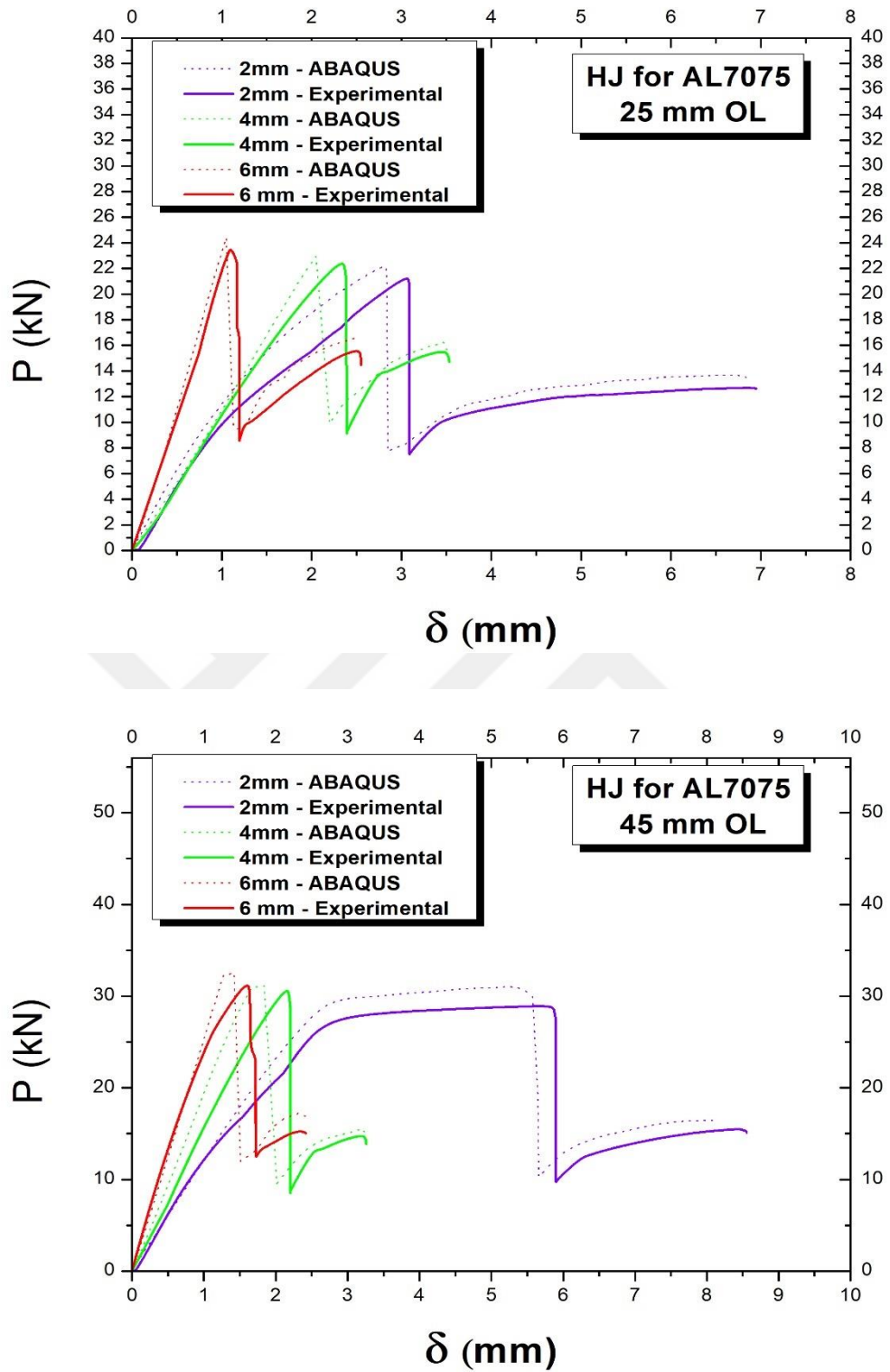


**Figure 5.18:** Experimentally and numerically obtained load displacement curves of HJ of AL7075.

We compared the results here with those of the single lap joints discussed above. Initially, the performance of the HJ was compared with the ADJ. It was observed that the respective stiffness of the joints, represented by the initial slope of the  $P$ - $\delta$  curve, were very close to each other for all the cases due to the stiffer adhesive material studied here [78, 79]. When such an adhesive material was used in the HJ, the load transferred by the bolt is low with the adhesive transferring more than 90% of the applied load due to the fact that the load was carried mostly by the end regions of the adhesive layer and the transfer of stresses from the ends of the overlap to its middle part was limited [125]. For instance, the maximum force values for the 4 mm AL6061 and AL7075 adherends with 45 mm OL were 23.32 kN and 29.20 kN in the ADJ, 24.20 kN and 30.55 kN in the HJ with 96.36% and 95.58% load fractions of the adhesive layer, respectively (see Figurer. 5.14, 5.17 and 5.18). Consequently, the EA values in the ADJ and in the first part of the HJ were very close to each other.

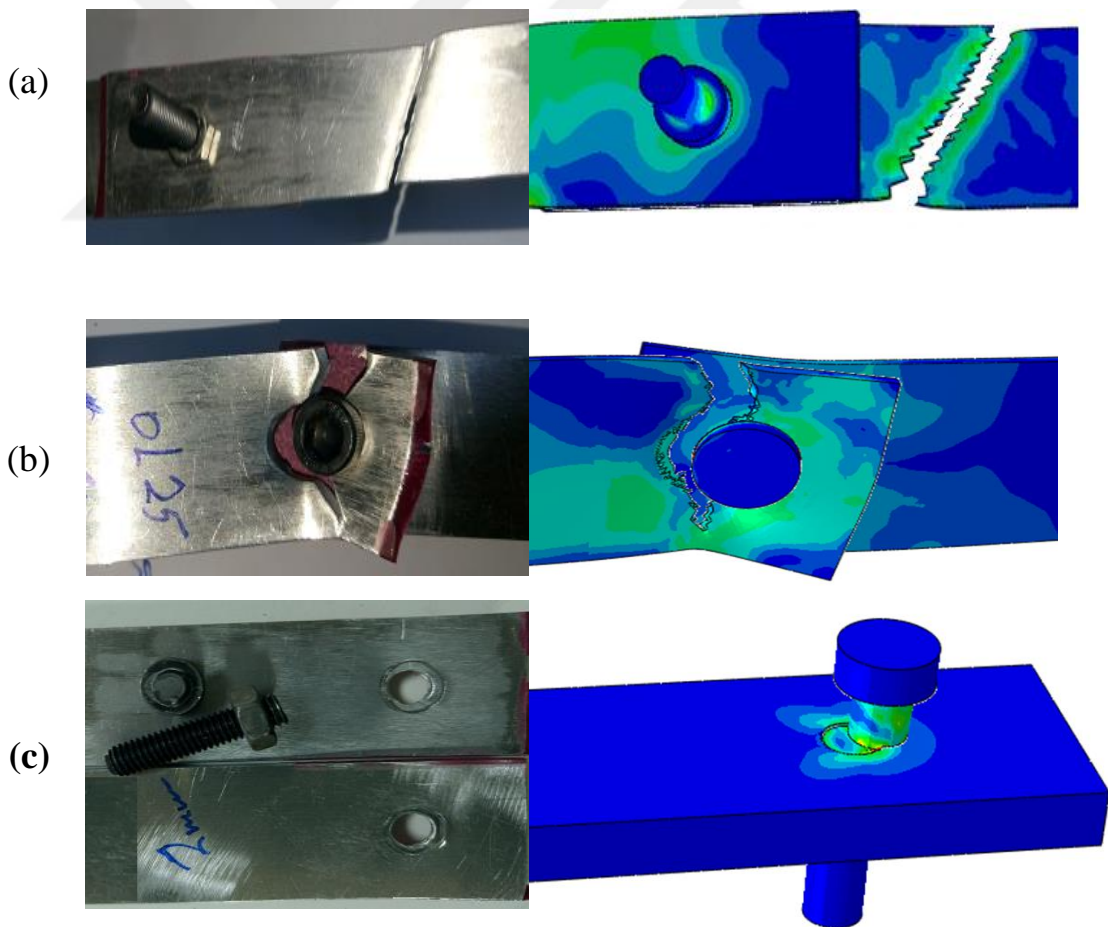


**Figure 5.19:** Failure modes observed in hybrid joints: (a) Adherend failure, (b) Net-tension failure and (c) Bolt failure (Left: Experimental, Right: FE simulation).

When the BJ and HJ configurations were compared, the latter absorbed more energy than the former, especially when the overlap length was increased. For instance, for the 4 mm AL7075 adherends, the respective values were 31.6 J and 44.8 J with a 41.7% increase for  $OL = 25$  mm and 30.3 J and 50.6 J with a 66.9% increase for  $OL = 45$  mm. Since the adhesive layer could sustain the load efficiently with an increase in the  $OL$ , the performance of the HJ with longer  $OL$  was better.

Figure 5.20 presents the shear and ductile damage distribution on the surface of the bolt material in the BJ and HJ configurations for the 6 mm AL6061 adherends with the  $OL = 25$  mm at  $P = 8$  kN. This force was the minimum observed after the cohesive failure took place in the HJ. Obviously, the bolt material started experiencing shear damage in the HJ configuration, whereas the damage in the bolt did not start yet in the BJ. In fact, in the HJ, the bolt did not support the adhesive layer up to its failure as discussed above, but later (after the failure of the adhesive layer) the load was transferred to the bolt material and the stresses on its surface increased dramatically and damage initiated, whereas in the BJ the bolt experienced loading from zero and increased gradually. It is worth mentioning that all the bolt failures occurred due to shear damage rather the ductile one. The bolt in HJ, therefore, could mainly carry the load from  $\delta = 1.33$  mm to only 2.78 mm, whereas in the BJ from initial loading to  $\delta = 2.80$  mm, i.e. the EA absorbed in the HJ due to presence of the bolt was smaller than that in the BJ. Therefore, the EA of the HJ was smaller than the sum of the values in the BJ and the ADJ individually for the cases the cohesive and bolt failures occurred in the hybrid configuration.

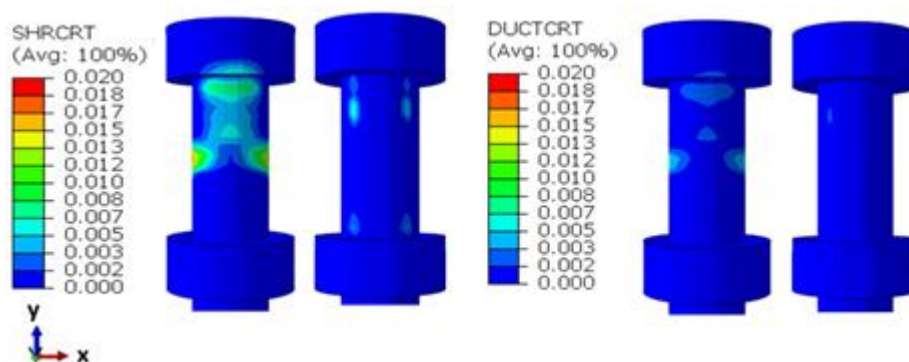


**Figure 5.20:** Shear and ductile damage distributions on the surfaces of bolts for 6 mm AL6061 adherends in the hybrid (left) and bolted (right) joint configurations at  $P = 8$  kN (after the cohesive failure for HJ).



## CHAPTER 6

### CONCLUSIONS AND FUTURE WORK

#### 6.1 Conclusions

This research focused on the experimental and analytical investigations on the effect of the various parameters of the strength of bolted, bonded and hybrid single lap joints. The core purpose of this study was to obtain a significant and relevant amount and source of knowledge on SLJs and the limitations of their stiffness. In terms of an overall outcome, the failure mode of the adhesive layers for ADJ and HJ reveals a cohesive failure which proves the quality of the surface treatment. The processing of adhesives requires a clean working space to prevent their contamination that may lead to adhesive failure as it may become a non-stick source of the zone. The study consisted of two parts.

The first study in Section 5.1 focused on the investigation into the effect of adherend thickness and material characteristics for bolted, bonded and hybrid single lap joints under axial tensile loading. From this study, the following observations and conclusions were made:

- In the single lap bolted joints, when aluminum adherends of 2 mm thickness were loaded, the adherend materials reached complete damage earlier than the bolt material. However, when this thickness was 6 mm, the bolt could not sustain the load and it failed earlier. In the case of 4 mm adherend thickness, the bolt reached complete damage earlier than the relatively stronger AL7075 adherends while weaker AL6061 adherends failed earlier than the bolt material.

- When only the adhesive layer was used to assemble aluminum adherends, the bonding adhesive always failed first. When the thickness of the adherend material increased, the maximum load improved while failure displacement decreased, resulting in an upsurge in the amount of energy absorbed. No significant change was observed in the amount of EA in either the AL6061 or AL7075 adherend materials that were tested.
- When bolt and adhesive layer were used together for assembling purposes, the adhesive material (AF163-2K) always reached complete damage earlier than either the bolt or the adherend materials. Furthermore, when the hybrid joint was compared with the pure adhesive joint, it was observed that the bolt material supported the adhesive layer and delayed its complete failure.
- The amount of energy absorbed (EA) in the hybrid joint (HJ) was equal to the sum of the EA for the adhesive and the bolt individually when the AL7075 adherends were assembled. However, this cannot be expressed for all the thicknesses of the AL6061. For instance, when their 6 mm thickness samples were united via bolted single lap joints, more energy was absorbed than those united via hybrid joints. Therefore, one cannot say whether HJ is always stronger than bolted or bonded joints or whether material characteristics play a significant role in the comparison.

In the second study in Section 5.2, the mechanical performances of bolted, bonded and hybrid single lap joints under tensile loading for different overlap lengths was investigated experimentally and numerically. From this part, the following observations and conclusions were made:

- In the single lap bolted joints, as a result of the loading misalignment the bolt rotated, where this was larger especially for smaller adherend thickness and shorter overlap lengths. This rotation led to an increase in the bearing area in the adherends, which in turn led to the net-tension failure. For their larger values, the rotation of the bolt was relatively constrained, and it carried the load substantially, hence bolt failure occurred.

- With an increase in the overlap length in the bonded joints, the stresses in the adhesive layer became smaller. Thus, the respective SLJ could carry larger load values for larger displacement values.
- In the HJ, the bolt supported the adhesive layer from the beginning up to its failure, where significant plastic deformation followed by the damage initiation occurred in the bolt. Furthermore, it was directly exposed to larger stresses after the failure of the adhesive layer. The bolt, therefore, could not carry the load effectively in the HJ (after the adhesive layer failure) as it was carrying in the BJ. Consequently, the amount of energy absorbed in the HJ was smaller than the sum of that for the BJ and the ADJ individually for the cases of the cohesive, and bolt failures occurring.

## **6.2 Future Work**

In future work, the effects of extra parameters on the strength of bolted, bonded and hybrid joints will be investigated as follows:

- It has now been envisaged that the effects of environmental factors on adhesion, such as humidity, temperature and chemical substances ought to be considered in future research.
- It has been recognized and acknowledged now that instead of using steel bolts, stiffer titanium bolts ought to be used.
- Several types of adhesive ought to be investigated along with the effect of the surface treatment of aluminum adherends.
- There ought to be a comprehensive and intensive study of the joint of dissimilar materials.
- There will be an extensive study on the effect of various strain rates for different loading rates.

It has become a known fact that the value and quality of the simulation process and stages technically lie in the possibilities of looking ahead and beyond any stage of the sampling during the test, which in all cases clearly explains and examines the strange observations by looking into the stages as examined in observatory

experiments. Notwithstanding, the experimental test thus exposes and opens up only the force displacement curves with the final failure modes. The effects to this end clearly show that the experimental test ought to be captured with the technical help of a high-speed camera with the aim of validating the simulation stages.

Technically, a more practical approach to the recognition and comprehension of the influence of several materials and geometric parameters leads to a number of critical points which have led emphasis the various parameters at once in order to comprehend better the nature of the interaction of each parameter among themselves. One might also comprehend the SLJ extensively to be examined with a great level of intensity of long and exceedingly short lap joints, in contrast to the joints of intermediate length examined in this research.

Furthermore, this study could envision the influence of the various parameters that were predicted in this analysis and their influences on the strength of the SLJ under a dynamic load situation. There is, however, a likely possibility that there could be an extension to this study into the bending effect by using the three-point bending test. In the future with various kinds of attachments, new kinds of mechanical fasteners, such as rivets could be combined and the aftermath may be linked with the current one to ascertain strength and failure modes. The approach of repairable applications might be accomplished on various kinds of materials and joints that are suitable to the kind of approaches specific to the needs of the utilized applications.

The vibration of the joint could be reduced by the adhesive layer when a ductile adhesive is utilized. The vibration effect is one of the most critical forms of damage that occur on an airplane. Therefore, comprehensive investigations of the effect of the thickness and type of adhesive on the damping ratio ought to be productively investigated.

The new design of the joint is planned to be considered and highly recommended in future work based on the conclusions of this study. Theoretically, Figure 6.1 presents the geometry and overlap length of the joint. Through the various adhesive layers, their configurations have now been presented and revealed in Figure 6.2. This could be experimentally and numerically investigated with the target to determine their effect on the stress distribution and joint strength.

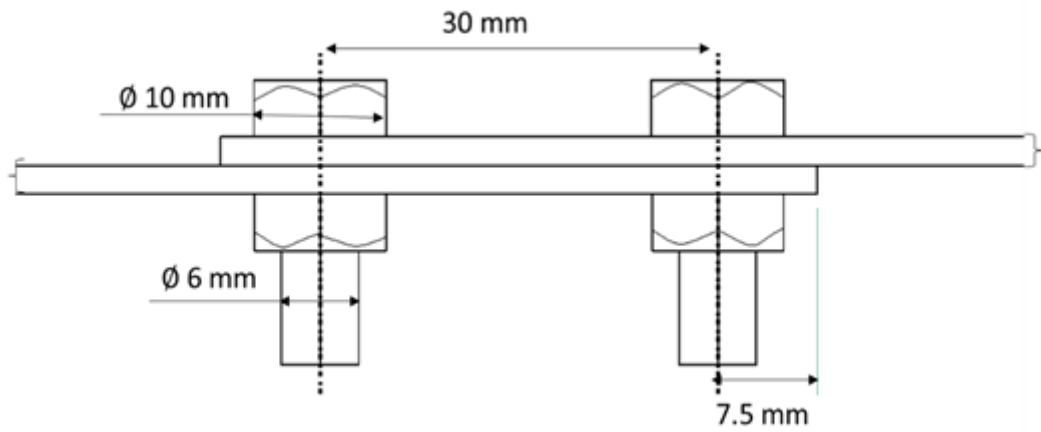


**Figure 6.1:** New joint configurations for BJ and HJ.

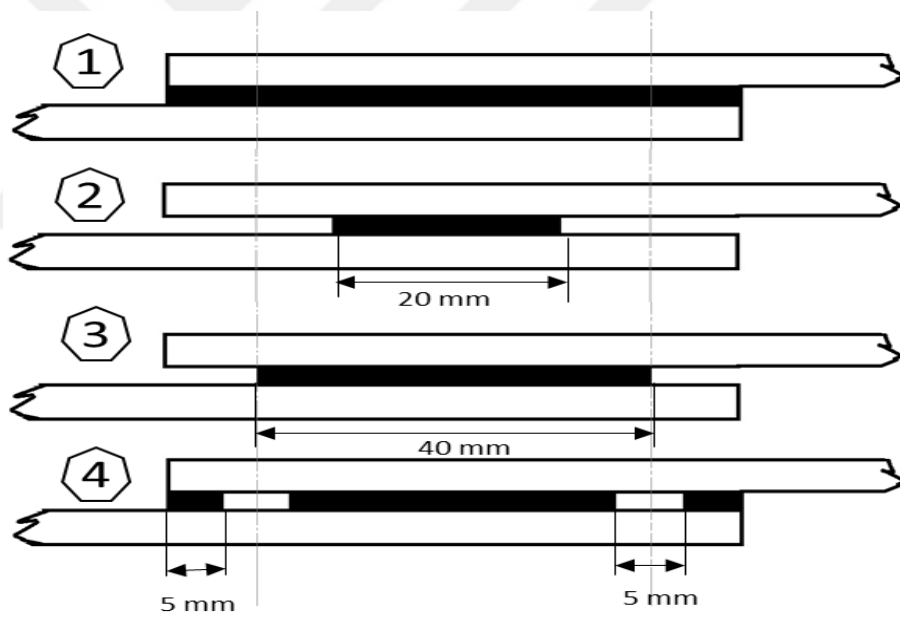


**Figure 6.2:** Adhesive layer configurations.

## REFERENCES

1. Baker, A.A.B., *Composite Materials for Aircraft Structures*. 2004: AIAA.
2. Campbell, F.C., *Joining: Understanding the Basics*. 2011: ASM International.
3. Campbell, F.C., *Structural Composite Materials*. 2010: ASM international.
4. da Silva, L.F., et al., *Analytical Models of Adhesively Bonded Joints—Part I: Literature Survey*. *International Journal of Adhesion and Adhesives*, 2009. 29(3): p. 319-330.
5. Kinloch, A., *Adhesion and Adhesives: Science and Technology*. 1987. City: London, Chapman and Hall, 1987.
6. Da Silva, L.F., A. Öchsner, and R.D. Adams, *Handbook of Adhesion Technology*. 2011: Springer Science & Business Media.
7. Berg, J.C., *Chapter 1 - Semi-Empirical Strategies for Predicting Adhesion A2 - Dillard, D.A*, in *Adhesion Science and Engineering*, A.V. Pocius and M. Chaudhury, Editors. 2002, Elsevier Science B.V.: Amsterdam. p. 1-73.
8. Comyn, J., *Adhesion Science*. 2007: Royal Society of Chemistry.
9. Van den Bosch, M., P. Schreurs, and M. Geers, *An Improved Description of the Exponential Xu and Needleman Cohesive Zone Law for Mixed-Mode Decohesion*. *Engineering Fracture Mechanics*, 2006. 73(9): p. 1220-1234.
10. Lau, C.C., *A Fracture Mechanics Approach to the Adhesion of Packaging Laminates*. 1993, Imperial College London (University of London).
11. Turon Travesa, A., *Simulation of Delamination in Composites under Quasi-Static and Fatigue Loading Using Cohesive Zone Models*. 2006: Universitat de Girona.

12. Packham, D.E., *Theories of Fundamental Adhesion*, In *Handbook of Adhesion Technology*. 2011, Springer. p. 9-38.
13. Zhao, X., R. Adams, and L. Da Silva, *Single Lap Joints with Rounded Adherend Corners: Experimental Results and Strength Prediction*. *Journal of Adhesion Science and Technology*, 2011. 25(8): p. 837-856.
14. Zhao, X., R. Adams, and L. Da Silva, *Single Lap Joints with Rounded Adherend Corners: Stress and Strain Analysis*. *Journal of Adhesion Science and Technology*, 2011. 25(8): p. 819-836.
15. Lang, T. and P. Mallick, *Effect of Spew Geometry on Stresses in Single Lap Adhesive Joints*. *International Journal of Adhesion and adhesives*, 1998. 18(3): p. 167-177.
16. Belingardi, G., L. Goglio, and A. Tarditi, *Investigating the Effect of Spew and Chamfer Size on the Stresses in Metal/Plastics Adhesive Joints*. *International Journal of Adhesion and Adhesives*, 2002. 22(4): p. 273-282.
17. Solmaz, M.Y. and T. Aydın, *An Experimental and Numerical Study on the Effects of Taper Angles and Overlap Length on the Failure and Stress Distribution of Adhesively-Bonded Single-Lap Joints*. *Mathematical and computational applications*, 2011. 16(1): p. 159-170.
18. Campilho, R., et al., *Strength Improvement of Adhesively-Bonded Joints Using a Reverse-Bent Geometry*. *Journal of Adhesion Science and Technology*, 2011. 25(18): p. 2351-2368.
19. Vangrimde, B. and R. Boukhili, *Descriptive Relationships between Bearing Response and Macroscopic Damage in GRP Bolted Joints*. *Composites Part B: Engineering*, 2003. 34(7): p. 593-605.
20. Salih, N.M. and M.J. Patil, 2, *Hybrid (Bonded/Bolted) Composite Single-Lap Joints and Its Load Transfer Analysis*. *International Journal of Advanced Engineering Technology E-ISSN 0976-3945 IJAET*, 2012. 3: p. 213-216.

21. Choi, J.-I., et al., *Failure Load Prediction of Composite Bolted Joint with Clamping Force*. *Composite Structures*, 2018. 189: p. 247-255.
22. Tajeuna, T.A., et al., *Effect of Geometrical Parameters of Aluminum-to-Steel Bolted Connections*. *Engineering Structures*, 2015. 102: p. 344-357.
23. Ireman, T., T. Ranvik, and I. Eriksson, *On Damage Development in Mechanically Fastened Composite Laminates*. *Composite Structures*, 2000. 49(2): p. 151-171.
24. Ekh, J. and J. Schön, *Effect of Secondary Bending on Strength Prediction of Composite, Single Shear Lap Joints*. *Composites Science and Technology*, 2005. 65(6): p. 953-965.
25. Kelly, G., *Quasi-Static Strength and Fatigue Life of Hybrid (Bonded/Bolted) Composite Single-Lap Joints*. *Composite structures*, 2006. 72(1): p. 119-129.
26. Davis, J.R., *Aluminum and Aluminum Alloys*. 2013.
27. Taib, A.A., et al., *Bonded Joints with Composite Adherends. Part II. Finite Element Analysis of Joggle Lap Joints*. *International journal of adhesion and adhesives*, 2006. 26(4): p. 237-248.
28. Taib, A.A., et al., *Bonded joints with Composite Adherends. Part I. Effect of Specimen Configuration, Adhesive Thickness, Spew Fillet and Adherend Stiffness on Fracture*. *International Journal of Adhesion and Adhesives*, 2006. 26(4): p. 226-236.
29. Akpınar, S., et al., *The Effect of the Spew Fillet on an Adhesively Bonded Single-Lap Joint Subjected to Bending Moment*. *Composites Part B: Engineering*, 2013. 55: p. 55-64.
30. Doru, M.O., et al., *Effect of the Spew Fillet on Adhesively Bonded Single-Lap Joint Subjected to Tensile Loading: Experimental and 3-D Non-Linear Stress Analysis*. *The Journal of Adhesion*, 2014. 90(3): p. 195-209.



31. Çalık, A. and S. Yıldırım, *An Investigation on the Effect of Parallel Slot in Bi-Adhesive Single Lap Joints with Spew Fillet*. Journal of Engg. Research Vol, 2015. 3(4): p. 95-110.
32. Grant, L., R. Adams, and L.F. da Silva, *Experimental and Numerical Analysis of Single-Lap Joints for the Automotive Industry*. International journal of adhesion and adhesives, 2009. 29(4): p. 405-413.
33. Ejaz, H., et al., *Topology Optimisation of Adhesive Joints using Non-Parametric Methods*. International Journal of Adhesion and Adhesives, 2018. 81: p. 1-10.
34. Liao, L., C. Huang, and T. Sawa, *Effect of Adhesive Thickness, Adhesive Type and Scarf Angle on the Mechanical Properties of Scarf Adhesive Joints*. International Journal of Solids and Structures, 2013. 50(25-26): p. 4333-4340.
35. Xu, W. and Y. Wei, *Strength and Interface Failure Mechanism of Adhesive Joints*. International journal of adhesion and adhesives, 2012. 34: p. 80-92.
36. Mohan, J., A. Ivanković, and N. Murphy, *Mode I Fracture Toughness of Co-Cured and Secondary Bonded Composite Joints*. International Journal of Adhesion and Adhesives, 2014. 51: p. 13-22.
37. Mohan, J., A. Ivanković, and N. Murphy, *Mixed-Mode Fracture Toughness of Co-Cured and Secondary Bonded Composite Joints*. Engineering Fracture Mechanics, 2015. 134: p. 148-167.
38. Castagnetti, D., A. Spaggiari, and E. Dragoni, *Effect of Bondline Thickness on the Static Strength of Structural Adhesives under Nearly-Homogeneous Shear Stresses*. The Journal of Adhesion, 2011. 87(7-8): p. 780-803.
39. Arenas, J.M., J.J. Narbon, and C. Alía, *Optimum Adhesive Thickness in Structural Adhesives Joints using Statistical Techniques Based on Weibull Distribution*. International Journal of Adhesion and Adhesives, 2010. 30(3): p. 160-165.

40. Ji, G., Z. Ouyang, and G. Li, *Effects of Bondline Thickness on Mode-I Nonlinear Interfacial Fracture of Laminated Composites: An Experimental Study*. Composites Part B: Engineering, 2013. 47: p. 1-7.
41. Naito, K., M. Onta, and Y. Kogo, *The Effect of Adhesive Thickness on Tensile and Shear Strength of Polyimide Adhesive*. International Journal of Adhesion and Adhesives, 2012. 36: p. 77-85.
42. Xu, W. and Y. Wei, *Strength Analysis of Metallic Bonded Joints Containing Defects*. Computational Materials Science, 2012. 53(1): p. 444-450.
43. Lucić, M., A. Stoić, and J. Kopač. *Investigation of Aluminum Single Lap Adhesively Bonded Joints*. In *Contemporary Achievements in Mechanics, Manufacturing and Materials Science*. 2005.
44. Seong, M.-S., et al., *A Parametric Study on the Failure of Bonded Single-Lap Joints of Carbon Composite and Aluminum*. Composite structures, 2008. 86(1): p. 135-145.
45. Samaei, M., et al., *The Influence of Geometric Parameters and Mechanical Properties of Adhesive on Stress Analysis in Adhesively Bonded Aluminum Single Lap Joint*. Transactions of FAMENA, 2014. 37(4): p. 91-98.
46. Samaei, M., M. Zehsaz, and T. Chakherlou, *Experimental and Numerical Study of Fatigue Crack Growth of Aluminum Alloy 2024-T3 Single Lap Simple Bolted and Hybrid (Adhesive/Bolted) Joints*. Engineering Failure Analysis, 2016. 59: p. 253-268.
47. Reis, P., J. Ferreira, and F. Antunes, *Effect of Adherend's Rigidity on the Shear Strength of Single Lap Adhesive Joints*. International Journal of Adhesion and Adhesives, 2011. 31(4): p. 193-201.
48. Campilho, R. and T. Fernandes, *Comparative Evaluation of Single-lap Joints Bonded with Different Adhesives by Cohesive Zone Modelling*. Procedia Engineering, 2015. 114: p. 102-109.

49. Ribeiro, T., et al., *Damage Analysis of Composite–Aluminium Adhesively-Bonded Single-Lap Joints*. *Composite Structures*, 2016. 136: p. 25-33.
50. Wei, K., et al., *Strength and Failure Mechanism of Composite-Steel Adhesive Bond Single Lap Joints*. *Advances in Materials Science and Engineering*, 2018. 2018.
51. Papanicolaou, G., et al., *Experimental and Numerical Investigation of Unbalanced Boron/Epoxy-Aluminum Single Lap Joints Subjected to a Corrosive Environment*. *Journal of Composite Materials*, 2016. 50(2): p. 145-157.
52. Turan, K. and Y. Pekbey, *Progressive Failure Analysis of Reinforced-Adhesively Single-Lap Joint*. *The Journal of Adhesion*, 2015. 91(12): p. 962-977.
53. Karachalios, E.F., R.D. Adams, and L.F.M. da Silva, *Single Lap Joints Loaded in Tension with High Strength Steel Adherends*. *International Journal of Adhesion and Adhesives*, 2013. 43: p. 81-95.
54. Adams, R. and N. Peppiatt, *Stress Analysis of Adhesive-Bonded Lap Joints*. *Journal of strain analysis*, 1974. 9(3): p. 185-196.
55. Crocombe, A. and R. Adams, *An Elasto-Plastic Investigation of the Peel Test*. *The Journal of Adhesion*, 1982. 13(3-4): p. 241-267.
56. Harris, J. and R. Adams, *Strength prediction of bonded single lap joints by non-linear finite element methods*. *International Journal of Adhesion and Adhesives*, 1984. 4(2): p. 65-78.
57. Sugiman, S. and H. Ahmad, *Comparison of Cohesive Zone and Continuum Damage Approach in Predicting the Static Failure of Adhesively Bonded Single Lap Joints*. *Journal of Adhesion Science and Technology*, 2017. 31(5): p. 552-570.

58. Rudawska, A. *Select Aspects of FEM Analysis for Bonded Joints of Polymer Composite Materials*. in *Journal of Physics: Conference Series*. 2015. IOP Publishing.
59. Campilho, R., et al., *Modelling of Single-Lap Joints using Cohesive Zone Models: Effect of the Cohesive Parameters on the Output of the Simulations*. *The Journal of Adhesion*, 2012. 88(4-6): p. 513-533.
60. Campilho, R., et al., *Modelling Adhesive Joints with Cohesive Zone Models: Effect of the Cohesive Law Shape of the Adhesive Layer*. *International Journal of Adhesion and Adhesives*, 2013. 44: p. 48-56.
61. Gustafson, P.A. and A.M. Waas, *The Influence of Adhesive Constitutive Parameters in Cohesive Zone Finite Element Models of Adhesively Bonded Joints*. *International Journal of Solids and Structures*, 2009. 46(10): p. 2201-2215.
62. Khoramishad, H., et al., *Predicting Fatigue Damage in Adhesively Bonded Joints using a Cohesive Zone Model*. *International Journal of fatigue*, 2010. 32(7): p. 1146-1158.
63. Carvalho, U. and R. Campilho, *Validation of Pure Tensile and Shear Cohesive Laws Obtained by the Direct Method with Single-Lap Joints*. *International Journal of Adhesion and Adhesives*, 2017. 77: p. 41-50.
64. Ekh, J. and J. Schön, *Load Transfer in Multirow, Single Shear, Composite-to-Aluminium Lap Joints*. *Composites Science and Technology*, 2006. 66(7-8): p. 875-885.
65. Starikov, R. and J. Schön, *Quasi-Static Behaviour of Composite Joints with Protruding-Head Bolts*. *Composite Structures*, 2001. 51(4): p. 411-425.
66. Skorupa, M., et al., *Observations and Analyses of Secondary Bending for Riveted Lap Joints*. *International Journal of Fatigue*, 2015. 72: p. 1-10.

67. McCarthy, M., et al., *Bolt-Hole Clearance Effects and Strength Criteria in Single-Bolt, Single-Lap, Composite Bolted Joints*. Composites science and technology, 2002. 62(10-11): p. 1415-1431.
68. McCarthy, C. and M. McCarthy, *Three-Dimensional Finite Element Analysis of Single-Bolt, Single-Lap Composite Bolted Joints: Part II—Effects of Bolt-Hole Clearance*. Composite Structures, 2005. 71(2): p. 159-175.
69. McCarthy, C.T., M.A. McCarthy, and V. Lawlor, *Progressive Damage Analysis of Multi-Bolt Composite Joints with Variable Bolt-Hole Clearances*. Composites Part B: Engineering, 2005. 36(4): p. 290-305.
70. Ireman, T., *Three-Dimensional Stress Analysis of Bolted Single-Lap Composite Joints*. Composite structures, 1998. 43(3): p. 195-216.
71. McCarthy, M., et al., *Three-Dimensional Finite Element Analysis of Single-Bolt, Single-Lap Composite Bolted Joints: Part I—Model Development and Validation*. Composite structures, 2005. 71(2): p. 140-158.
72. Egan, B., et al., *Stress Analysis of Single-Bolt, Single-Lap, Countersunk Composite Joints with Variable Bolt-Hole Clearance*. Composite Structures, 2012. 94(3): p. 1038-1051.
73. Chakherlou, T., et al., *An Experimental Investigation of the Bolt Clamping Force and Friction Effect on the Fatigue Behavior of Aluminum Alloy 2024-T3 Double Shear Lap Joint*. Materials & Design, 2011. 32(8-9): p. 4641-4649.
74. HART-SMITH, L.J., *Bonded-Bolted Composite Joints*. Journal of Aircraft, 1985. 22(11): p. 993-1000.
75. Sadowski, T., P. Golewski, and E. Zarzeka-Raczkowska, *Damage and Failure Processes of Hybrid Joints: Adhesive Bonded Aluminium Plates Reinforced by Rivets*. Computational Materials Science, 2011. 50(4): p. 1256-1262.

76. Sadowski, T., M. Kneć, and P. Golewski, *Experimental Investigations and Numerical Modelling of Steel Adhesive Joints Reinforced by Rivets*. International Journal of Adhesion and Adhesives, 2010. 30(5): p. 338-346.
77. Fu, M. and P.K. Mallick, *Fatigue of Hybrid (Adhesive/Bolted) Joints in SRIM Composites*. International Journal of Adhesion and Adhesives, 2001. 21(2): p. 145-159.
78. Imanaka, M., K. Haraga, and T. Nishikawa, *Fatigue Strength of Adhesive/Rivet Combined Lap Joints*. The Journal of Adhesion, 1995. 49(3-4): p. 197-209.
79. Lopez-Cruz, P., J. Laliberté, and L. Lessard, *Investigation of Bolted/Bonded Composite Joint Behaviour using Design of Experiments*. Composite Structures, 2017. 170: p. 192-201.
80. Marannano, G. and B. Zuccarello, *Numerical Experimental Analysis of Hybrid Double Lap Aluminum-CFRP Joints*. Composites Part B: Engineering, 2015. 71: p. 28-39.
81. Kweon, J.-H., et al., *Failure of Carbon Composite-To-Aluminum Joints with Combined Mechanical Fastening and Adhesive Bonding*. Composite structures, 2006. 75(1-4): p. 192-198.
82. Lee, Y.-H., et al., *Failure Load Evaluation and Prediction of Hybrid Composite Double Lap Joints*. Composite Structures, 2010. 92(12): p. 2916-2926.
83. Tan, S.C., *Evaluation of Composite Joints*. 1994, Dayton Univ Oh Research Inst.
84. Moroni, F., A. Pironi, and F. Kleiner, *Experimental Analysis and Comparison of the Strength of Simple and Hybrid Structural Joints*. International Journal of Adhesion and Adhesives, 2010. 30(5): p. 367-379.

85. Stewart, M. and M. Stewart. *An Experimental Investigation of Composite Bonded and/or Bolted Repairs using Single Lap Joint Designs*. In *38th Structures, Structural Dynamics, and Materials Conference*. 1997.
86. Sadowski, T. and E. Zarzeka-Raczkowska, *Hybrid Adhesive Bonded and Riveted Joints—Influence of Rivet Geometrical Layout on Strength of Joints/Połączenia Hybrydowe Klejowo-Nitowe-Wpływ Geometrii Rozmieszczenia Nitów Na Wytrzymałość Połączeń*. *Archives of Metallurgy and Materials*, 2012. 57(4): p. 1127-1135.
87. Fu, M. and P. Mallick, *Fatigue of Hybrid (Adhesive/Bolted) Joints in SRIM Composites*. *International Journal of Adhesion and Adhesives*, 2001. 21(2): p. 145-159.
88. Senguttuvan, N. and J. Lillymercy, *Joint Strength Analysis of Single Lap Joint in Glass Fiber Composite Material*. *International Journal of Applied Engineering Research*, 2015. 10(7): p. 16535-16545.
89. Pirondi, A. and F. Moroni, *Clinch-Bonded and Rivet-Bonded Hybrid Joints: Application of Damage Models for Simulation of Forming and Failure*. *Journal of Adhesion Science and Technology*, 2009. 23(10-11): p. 1547-1574.
90. Karthik, A., G. Velukumar, and S. Srinivasan, *Experimental Analysis Made on Hybrid Composite Joint of Woven Ring Type*. *International Journal of Research and Innovation in Engineering Technology*, 2015. 1(10).
91. Lakshmi Narasimman, Y., *Failure Mode and Analysis of the Bonded/bolted Joints between a Hybrid Fibre Reinforced Polymer and Aluminium Alloy*. *Journal of Advanced Materials and Processing*, 2015. 3(2): p. 49-60.
92. Choi, J.-I., et al., *Experimental Study on Failure Mechanism of Hybrid Composite Joints with Different Adhesives*. *Fibers and Polymers*, 2017. 18(3): p. 569-574.

93. Hai, N.D. and H. Mutsuyoshi, *Structural Behavior of Double-Lap Joints of Steel Splice Plates Bolted/Bonded to Pultruded Hybrid CFRP/GFRP Laminates*. Construction and Building Materials, 2012. 30: p. 347-359.
94. Zhao, K. and L.R. Xu, *Size Effect of the Adhesive Bonding Strengths of Metal/Polymer Similar and Dissimilar Material Joints*. The Journal of Adhesion, 2015. 91(12): p. 978-991.
95. Kishore, A.N. and N.S. Prasad, *An Experimental Study of Flat-Joggle-Flat Bonded Joints in Composite Laminates*. International Journal of Adhesion and Adhesives, 2012. 35: p. 55-58.
96. Neto, A.S., R. de Alkmim Dias, and A.F. Ávila, *New Design to Improve Single-Lap Joint Strength*, In Fifth International Symposium on Solid Mechanics. 2015: Belo Horizonte, MG, Brazil.
97. Wang, Y., et al., *Improvement in Strength of Adhesively Bonded Single-Lap Joints using Reinforcements*. The Journal of Adhesion, 2015. 91(6): p. 434-448.
98. Ouellet, M. and A. Vadean. *Design Improvement of Hybrid Composite Joints by Axiomatic Design*. In *The Seventh International Conference on axiomatic design*, Worcester. 2013.
99. *Scotch-weld<sup>™</sup> Structural Adhesive Film AF-163-2. Technical Data Sheet*,. 3M Aerospace and Aircraft Maintenance Division, St. Paul, MN. 2009
100. Bettini, P., et al., *Composite Chiral Structures for Morphing Airfoils: Numerical Analyses and Development of a Manufacturing Process*. Composites Part B: Engineering, 2010. 41(2): p. 133-147.
101. da Silva, L.F., A. Pironi, and A. Ochsner, *Hybrid Adhesive Joints*. Vol. 6. 2011: Springer Science & Business Media.



102. Pavlović, M., et al., *Bolted Shear Connectors vs. Headed Studs Behaviour in Push-out Tests*. Journal of Constructional Steel Research, 2013. 88: p. 134-149.
103. Rao, S., *The finite Element Method in Engineering* Butterworth. 1999, Heinemann.
104. Barenblatt, G.I., *The Mathematical Theory of Equilibrium Cracks in Brittle Fracture*, In Advances in Applied Mechanics. 1962, Elsevier. p. 55-129.
105. Hillerborg, A., M. Modéer, and P.-E. Petersson, *Analysis of Crack Formation and Crack Growth in Concrete by Means of Fracture Mechanics and Finite Elements*. Cement and concrete research, 1976. 6(6): p. 773-781.
106. Neto, J., R. Campilho, and L. Da Silva, *Parametric Study of Adhesive Joints with Composites*. International Journal of Adhesion and Adhesives, 2012. 37: p. 96-101.
107. Da Silva, L.F. and R.D. Campilho, *Advances in Numerical Modelling of Adhesive Joints*. 2012: Springer.
108. Campilho, R.D.S.G., et al., *Modelling Adhesive Joints with Cohesive Zone Models: Effect Of the Cohesive Law Shape of the Adhesive Layer*. International Journal of Adhesion and Adhesives, 2013. 44(Supplement C): p. 48-56.
109. Hibbitt, Karlsson, and Sorensen, *ABAQUS/Explicit: User's Manual V6.16*. Vol. 1. 2016: Hibbitt, Karlsson and Sorenson Incorporated.
110. Hibbitt, Karlsson, and Sorensen, *ABAQUS: Theory Manual V6.16*. 2016: Hibbitt, Karlsson & Sorensen.
111. Hibbitt, Karlsson, and Sorensen, *ABAQUS/Explicit: Software V6.16*. 2016, Hibbitt, Karlsson and Sorenson Incorporated.
112. Hibbitt, H., B. Karlsson, and P. Sorensen, *Abaqus Analysis User's Manual V6.16*. Dassault Systèmes Simulia Corp.: Providence, RI, USA, 2016.

113. Bettini, P., et al., *Composite Chiral Structures for Morphing Airfoils: Numerical Analyses and Development of a Manufacturing Process*. Composites Part B: Engineering, 2010. 41(2): p. 133-147.
114. Billal, M.K., et al., *Prediction of Component Failure using 'Progressive Damage and Failure Model' and Its Application in Automotive Wheel Design*. 2015, SAE Technical Paper.
115. Hooputra, H., et al., *A Comprehensive Failure Model for Crashworthiness Simulation of Aluminium Extrusions*. International Journal of Crashworthiness, 2004. 9(5): p. 449-464.
116. Shigley, J.E., *Shigley's Mechanical Engineering Design*. 2011: Tata McGraw-Hill Education.
117. Tanlak, N., F. Sonmez, and E. Talay, *Detailed and Simplified Models of Bolted Joints under Impact Loading*. The Journal of Strain Analysis for Engineering Design, 2011. 46(3): p. 213-225.
118. Egan, B., et al., *Modelling a Single-Bolt Countersunk Composite Joint using Implicit and Explicit Finite Element Analysis*. Computational Materials Science, 2012. 64: p. 203-208.
119. Thai, H.-T. and B. Uy, *Finite Element Modelling of Blind Bolted Composite Joints*. Journal of Constructional Steel Research, 2015. 112: p. 339-353.
120. Kapidžić, Z., L. Nilsson, and H. Ansell, *Finite Element Modeling of Mechanically Fastened Composite-Aluminum Joints in Aircraft Structures*. Composite structures, 2014. 109: p. 198-210.
121. Ghahremaninezhad, A. and K. Ravi-Chandar, *Ductile Failure Behavior of Polycrystalline Al 6061-T6*. International journal of fracture, 2012. 174(2): p. 177-202.
122. Brar, N., V. Joshi, and B. Harris. *Constitutive Model Constants for Al7075-t651 and Al7075-t6*. In *AIP conference proceedings*. 2009. AIP.

123. Nguyen, H.T. and S.E. Kim, *Finite Element Modeling of Push-out Tests for Large Stud Shear Connectors*. Journal of Constructional Steel Research, 2009. 65(10-11): p. 1909-1920.
124. Kweon, J.-H., et al., *Failure of Carbon Composite-to-Aluminum Joints with Combined Mechanical Fastening and Adhesive Bonding*. Composite Structures, 2006. 75(1): p. 192-198.
125. Kadioglu, F. and R. Adams, *Non-Linear Analysis of a Ductile Adhesive in the Single Lap Joint under Tensile Loading*. Journal of Reinforced Plastics and Composites, 2009. 28(23): p. 2831-2838.
126. Aydın, M.D., Ş. Temiz, and A. Özel, *Effect of Curing Pressure on the Strength of Adhesively Bonded Joints*. Journal of Adhesion, 2007. 83(6): p. 553-571.

## Resume

Name: Mossa Ramadan El zaroug

Phone: +218922675175

E-mail: [malzarug@yahoo.com](mailto:malzarug@yahoo.com)

Date of Birth: 16-06-1977

Marital Status: Married.

Address: Omar Al Mukhtar University, Albeida / Libya, P. O. Box: 919.

Nationality: Libyan.



### Education

- ♦ BSc in Mechanical Engineering, Sebha University, Sebha - Libya, 1994-1999.
- ♦ MSc in Advanced Materials Engineering, University of Bradford, Bradford- UK, 2007-2008.

### Language

- ♦ Excellent oral and written communication skills in Arabic and English.
- ♦ Moderate oral and written communication skills in German and Turkish.

### Personal Profile

- ♦ Mechanical and Materials Science Degrees (BSc & MSc).
- ♦ Detail-oriented with strong mathematical aptitude.
- ♦ Professional user in *ABAQUS* software.
- ♦ Scientifically inclined with strong manual dexterity.
- ♦ Exceptional troubleshooting and problem-solving abilities.
- ♦ Computer literate with experience in Microsoft Office and Windows applications.
- ♦ Committed to lifelong learning and personal development.
- ♦ Productive independent worker and an effective team player.
- ♦ Responsible, resourceful, and reliable.

## **Experience**

Omar Almkhtar University, 2001-2006

- ♦ Department coordinator; organizing academic events, agenda, and memos.
- ♦ Demonstrator; giving tutorials and co-supervising undergraduate academic projects.

## **Professional Experience**

Omar Almkhtar University, 2009 - present

- ♦ Lecturer, instructing the following courses:
  - Strength of Materials.
  - Materials Science.
  - Descriptive Geometry.
  - Engineering Mechanics (Statics).

## **Research**

- ♦ Experimental Analysis of Wood -Polymers Composite, 2008.
- ♦ The Effect of Coupling Agents on Wood- Polymers Composite, 2009.

## **Activities**

- ♦ Travel.
- ♦ Reading.
- ♦ Sports.